UNIVERSITY OF OKLAHOMA

GRADUATE COLLEGE

UNDERSTANDING AND PREDICTING NOCTURNAL CONVECTION INITIATION USING AN ENSEMBLE-BASED MULTI-SCALE DATA ASSIMILATION SYSTEM

A THESIS

SUBMITTED TO THE GRADUATE FACULTY

in partial fulfillment of the requirements for the

Degree of

MASTER OF SCIENCE IN METEOROLOGY

By

SAMUEL KYLE DEGELIA
Norman, Oklahoma
2016

Downloaded from SHAREOK. Persistent Handle URL: https://hdl.handle.net/11244/45040

UNDERSTANDING AND PREDICTING NOCTURNAL CONVECTION INITIATION USING AN ENSEMBLE-BASED MULTI-SCALE DATA ASSIMILATION SYSTEM

A THESIS APPROVED FOR THE
SCHOOL OF METEOROLOGY

BY

Dr. Xuguang Wang, Chair

Dr. David J. Stensrud, Co-Chair

Dr. David B. Parsons

© Copyright by SAMUEL KYLE DEGELIA 2016
All Rights Reserved.

Acknowledgments

I would first like to thank my thesis advisers Dr. Xuguang Wang of the University of Oklahoma, and Dr. David Stensrud of Pennsylvania State University. They proved extremely helpful throughout the course of my studies, both academically and emotionally. Thankfully, they were also kind enough to answer my barrages of questions and steer me back on track when I needed it. I look forward to many more years of academic and professional pursuits under their helpful guidance.

I would also like to acknowledge Dr. David Parsons as the third member of my thesis committee and I am indebted to him for his assistance throughout both my undergraduate and graduate careers. This work would also not have been completed nearly as quickly or thoroughly without the aid of Dr. Aaron Johnson of the University of Oklahoma. His assistance in my multitude of technical questions is extremely appreciated.

I must also express my extreme gratitude to my parents, Pat and Laura Degelia, for their years of personal support and financial assistance. They have always been there to help with every problem I have faced and I could not have achieved this without them. Lastly, I thank my fiancé Gabrielle for her devotedness in getting me through the many long nights that came with this work.

Table of Contents

Acknowledgments **iv**

List of Tables **viii**

List of Figures **ix**

Abstract **xix**

1 Introduction **1**

1.1 Nocturnal precipitation maximum 1

1.2 Nocturnal convection initiation 8

2 Overview of 25 June 2013 CI event **14**

2.1 Synoptic and mesoscale environment 14

2.2 Operational forecasts 19

2.3 Convective history 19

3 Methodology **24**

3.1 Model configuration 24

3.1.1 Initial and lateral boundary conditions 24

3.1.2 Physical parameterizations 26

3.2 Data assimilation system configuration 28

3.2.1 The ensemble Kalman filter . . . 28
3.2.2 Observational dataset . . . 31
3.2.3 Error treatment . . . 32
3.3 Experimental design . . . 35

4 Observation impact analysis 38
4.1 Data assimilation cycling results . . . 38
4.1.1 Inner domain conventional observation verification . . . 40
4.1.2 Inner domain radar observation verification . . . 44
4.2 Ensemble forecasts . . . 51
4.2.1 Convection initiation forecast differences . . . 51
4.2.2 Thermodynamic and kinematic forecast differences . . . 59
4.3 Summary of observation impacts . . . 63

5 Sensitivity to physical parameterizations 66
5.1 Planetary boundary layer parameterizations . . . 66
5.2 Microphysical parameterizations . . . 76

6 Convection initiation mechanisms 86
6.1 Synoptic and mesoscale environment . . . 86
6.2 Sources of lift . . . 88
6.3 Two-dimensional discrete cosine transformation . . . 96
6.3.1 Mesoscale sources of lift . . . 96
6.3.2 Gravity wave analysis . . . 99
6.4 Summary of CI . . . 104

7 Conclusions 109
7.1 Summary of results . . . 109
7.2 Future work . . . 111

Bibliography **114**

List of Tables

3.1 Physical parameterization schemes used for all non-physics sensitivity experiments. 28

3.2 Summary of observation assimilation experiments on the inner domain. 37

5.1 Microphysics schemes studied in 5.2, as well as their moments and predicted species. 77

List of Figures

1.1 Hovmöller diagram of mean diurnal cycle of average hourly rainrates in the US between 1996 and 2007 for both spring and summer from Surcel et al. (2010). The Great Plains region of the US spans from -97° to -102° W. 3

1.2 Schematic features of a severe weather outbreak in the Great Plains as aided by the developing LLJ from Newton (1967). Solid lines are sea level isobars; dashed lines are streamlines of upper-tropospheric flow. Shading outlines the general area of the LLJ moist tongue and region of potential instability 4

1.3 Schematic plot of PV train mechanisms in the lee of a mountain range from Li and Smith (2010). U represents the background wind, N represents the environmental stability, Z_1 is the shear level, H is the heating level, and $Q(z)$ is the vertical profile of diurnal heating over the mountain. 5

1.4 Hovmöller diagram for radar-derived rain-rate for 27-29 May 1998 in the southern Great Plains from Carbone et al. (2002). Smaller squall lines were initiated with the mesoscale convective vortex (noted as cold pool dynamics) but rapidly propagated eastward from it. . . . 7

1.5 Forecast accumulated precipitation that fell in two model runs with only a 1 g kg^{-1} perturbation in the PBL moisture at the location shown in the box, from Martin and Xue (2006). The arrow in each figure, in (a) northwestern Oklahoma; and (b) north-central Oklahoma, indicates the location of the box. Contour increments are 15 mm. The 10 g kg^{-1} isopleth of water vapor at 10 m above the ground is drawn at the initial model time to indicate the location of a dryline. Only a slight perturbation in a small area was able to completely change the precipitation structure in multiple locations. 10

1.6 One hour forecast probabilities (2100 – 2200 UTC) of composite reflectivity (CREF) > 25 dBZ for (a), a control forecast initialized from the NCAR mesoscale ensemble with no DA; and (b) a forecast initialized after 3 hours of surface data assimilation from Sobash and Stensrud (2015). Maximum observed CREF > 25 dBZ from 2100 to 2200 UTC is shaded in black. 12

2.1 Upper-air analyses and observations at 0000 UTC on 25 June of (a) 300 hPa isotachs (fill), streamlines (black contours), and divergence (yellow contours); and (b) 700 hPa heights (black contours), temperature (red contours), and dewpoints > -4 °C (green contours). 15

2.2 Surface observations across the Great Plains at 2213 UTC on 24 June. The brown line indicates the subjectively analyzed location of the surface dryline at 50 °F, while the red line indicates the approximate location of the warm front. Also contoured are the 5 °F isodrosotherms. 16

2.3 Radar observations of 1 km AGL reflectivity valid at (a) 2200 UTC on 24 June; (b) 0000 UTC; (c) 0300 UTC; and (d) 0500 UTC on 25 June. The red circle in (c) indicates a radar fine line moving northwestward. 17
2.4 As in Fig. 2.2 but at 0313 UTC on 25 June. 18
2.5 Preliminary storm reports from the Storm Prediction Center between 1200 UTC on 24 June and 1200 UTC on 25 June. Black icons indicate high wind or large hail reports. 18
2.6 Radar observations of 1 km AGL reflectivity valid at 0230 UTC. The circled area indicates the initiation episode of interest. 20
2.7 Radar observations of 1 km AGL reflectivity valid at (a) 0300 UTC; (b) 0400 UTC; (c) 0500 UTC; and (d) 0900 UTC on 25 June. . . . 21
2.8 Soundings from KDDC at (a) 0000 UTC; and (b) 1200 UTC on 25 June. 23

3.1 Domain configurations for all simulations. The outer box represents the outer, 12 km domain, while the inner box is the convection-allowing, 4 km domain. Each circle within the inner domain represents a WSR-88D radar that was assimilated. 25
3.2 Stretched vertical grid spacing for 50 terrain-following vertical levels in all simulations. 26

3.3 Illustration of the potential of an EnKF for making meteorologically reasonable analysis increments from Hamill et al. (2011a). (a) Mean background forecast of 850 hPa winds. Assuming an observation 10 m s^{-1} greater than the background is available at the black dot. (b) Wind analysis increment from the assimilation of the single observation when using an EnKF, and (c) Wind analysis increment when using an average of the ensemble covariance over all locations around the hurricane, a surrogate for the increment that may be expected from a 3DVar system. 30

3.4 Illustration of covariance localization from Hamill (2006). (a) Correlations of sea-level pressure directly estimated from a 25 member ensemble with pressure at a point in the western Pacific (fill). Solid lines denote ensemble mean background sea-level pressure contoured every 8 hPa. (b) As in (a) but using a 200-member ensemble. (c) Covariance localization correlation function. (d) Correlation estimate from 25-member ensemble after application of covariance localization. Note how even with 175 less ensemble members, (d) is very similar to (b) due to the use of the covariance localization function. 34

3.5 Flowchart for the allDA experiment. The green arrows indicate analysis times during which conventional observations are assimilated, while the orange lines indicate analysis times during which radar observations are assimilated. The top line is for the outer, 12 km domain while the bottom line is for the inner, 4 km domain. . 36

4.1 Verification statistics from the outer domain variables of temperature (K; a-c), water vapor mixing ratio (g kg^{-1}; d-f), and wind speed (m s^{-1}; g-i) including: (a,d,g) alternating time series of background and analysis RMSI (sawtooth; solid line) and TES (dotted line); (b,e,h) profiles of background RMSI (solid line) and TES (dotted line); and (c,f,i) background (dashed line) and analysis (solid line) bias. 41

4.2 As in Fig. 4.1(a,g,d) but for the inner domain variables of temperature (K), water vapor mixing ratio (g kg^{-1}), and wind speed (m s^{-1}) for convDA (green); radarDA (blue); and allDA (red). 42

4.3 Final EnKF mean (a,b) temperature biases (K); and (c,d) water vapor mixing ratio biases (g kg^{-1}) at each observation location below 800 hPa for (a,c) radarDA; and (b,d) allDA. 43

4.4 Final EnKF mean analysis (0130 UTC) soundings from (a) southern Kansas and (b) northwestern Kansas for: convDA (green); radarDA (blue); and allDA (red). 45

4.5 Final EnKF mean analysis (0130) of the most unstable convective available potential energy (MUCAPE; J kg^{-1}; filled) and the lifted parcel level (LPL; m; red contours) for (a) radarDA; and (b) allDA. The LPL indicates the height AGL that the most unstable parcel originates. 46

4.6 Final EnKF mean analysis (0130) of the 850 hPa wind speeds and barbs for (a) convDA; (b) radarDA; and (c) allDA. 47

4.7 As in Fig. 4.2 but for the inner domain variables of radar reflectivity factor (dBZ; a-c) and radial wind (m s^{-1}; d-f). The blue line represents the radarDA experiment and the red line represents the allDA experiment. All statistics are only calculated at observation locations where both the guess and observation have reflectivity > 10 dBZ. 49

4.8 Alternating time series of background and analysis (a) percentage of precipitation observations where precipitation was also located in the guess; and (b) percentage of clear-air observations where clear-air was also located in the guess. The green lines indicate convDA; the blue lines indicate radarDA; and the red lines indicate allDA. . 50

4.9 Spaghetti contours for each ensemble member of composite radar reflectivity factor greater than 30 dBZ for the (a) convDA; (b) radarDA; and (c) allDA EnKF analyses (at 0130 UTC). Each member plotted is a different color. Observed 1 km AGL reflectivity at the same time is given in (d). 52

4.10 Observed 1-km AGL radar reflectivity factor from a) 0200; b) 0300; c) 0400; and d) 0500 UTC. 54

4.11 Spaghetti contours for each ensemble member of composite radar reflectivity factor greater than 40 dBZ for the convDA experiment, valid at a) 0200; b) 0300; c) 0400; and d) 0500 UTC. 55

4.12 As in Fig. 4.11 but for the radarDA experiment. 57

4.13 As in Fig. 4.11 but for the allDA experiment. 58

4.14 Two hour surface temperature (°F) ensemble mean forecasts valid at 0330 UTC from the: a) convDA; b) radarDA; and c) allDA experiments. 60

4.15 Two hour forecasts for member 3 valid at 0330 UTC of a,c) 800 hPa vertical velocity; and b,d) 600 hPa vertical velocity. (a,b) are from radarDA, while (c,d) are from allDA. Also overlaid on all plots are the contours of 30 dBZ composite reflectivity. 61
4.16 Two hour forecast ensemble mean soundings valid at 0330 UTC from near the area CI for: convDA (green); radarDA (blue); and allDA (red). 62
4.17 As in Fig. 4.6 but for the 2 hour ensemble mean forecasts of 850 hPa wind speeds (valid at 0330 UTC). 64

5.1 Ensemble mean surface temperature forecasts (°F) from 0330 UTC on 25 June for the (a) MYNN; (b) QNSE; (c) MYJ; (d) ACM2; and (e) YSU PBL sensitivity experiments. 70
5.2 Ensemble mean soundings from (a) within the cold pool; and (b) ahead of the cold pool for each PBL scheme. 71
5.3 As in Fig. 5.1 but for 850 hPa wind speeds (kts). 73
5.4 As in Fig. 5.1 but for 600 hPa vertical velocity (m s^{-1}) and only for member 3. Also plotted is the 30 dBZ composite reflectivity contour. 74
5.5 As in Fig. 5.1 but at 0400 UTC and for the spaghetti contours for each ensemble member of composite reflectivity greater than 30 dBZ. 75
5.6 Ensemble mean forecasts of composite reflectivity (dBZ) valid at 0330 UTC for (a) Lin; (b) Thompson; (c) Morrison; (d) WSM6; and (e) WDM6 microphysics sensitivity experiments. Also plotted are surface wind barbs (kts). 80
5.7 As in Fig. 5.6 but for surface temperature (°F). 82
5.8 Ensemble mean soundings from (a) within the cold pool; and (b) ahead of the cold pool for each microphysics scheme. 83

5.9 As in Fig. 5.6 but at 0400 UTC and for the spaghetti contours for each ensemble member of composite reflectivity greater than 30 dBZ. 84

5.10 As in Fig. 5.9 but at 0500 UTC and for the spaghetti contours for each ensemble member of composite reflectivity greater than 40 dBZ. 85

6.1 Composite reflectivity forecasts from allDA member 3 (a,c,e) and the corresponding 1 km AGL reflectivity observations (b,d,f) at (a,b) 0400 UTC; (c,d) 0500 UTC; and (e,f) 0600 UTC. 87

6.2 Forecasts valid at 0300 UTC from allDA member 3 of (a) surface dewpoint temperature (°F) and winds (kts); and (b) Potential vorticity (PVU) and winds (kts) at 10 km; and. The star in each plot indicates the simulated location of CI at $\sim$ 0415 UTC. 89

6.3 Forecasts from allDA member 3 of 800 hPa moisture convergence ($*10^4$ g kg^{-1} s^{-1}) valid at (a) 0200; and (b) 0300; (c) 0400; and (d) 0500 UTC. The circle in (c,d) indicates the location of the LLJ convergence. 90

6.4 As in Fig. 6.3 but for surface temperature (°F) and winds (kts). The star in each plot indicates the simulated location of CI at $\sim$ 0415 UTC. 91

6.5 Forward trajectory of a parcel originating just east of the dryline at 0130 UTC and ending under the location of CI at 0430 UTC (in blue) for allDA member 3. The opacity and size of the red dots are proportional to the height AGL of the parcel. 93

6.6 Forecast from allDA member 3 of east to west vertical cross-sections through the y-location of the parcel trajectory's location at (a,b) 0300; (c,d) 0400; and (e,f) 0500 UTC. Plotted in (a,c,e) are potential vorticity (fill, PVU), total hydrometeor mixing ratio (green contours, g kg^{-1}), and virtual potential temperature (black contours, K). Plotted in (b,d,f) are vertical velocity (fill, m s^{-1}) and virtual potential temperature (black contours, K). The parcel trajectory is the same as the 2D trajectory in Fig. 6.5. See text for description of circles. 94

6.7 Forecasts from allDA member 3 of 600 hPa vertical velocity (m s^{-1}) valid at (a) 0230; and (b) 0300; (c) 0330; and (d) 0400 UTC. The circle in (c) indicates the location of the two positive vertical velocity bands. Also overlaid on each plot is the 30 dBZ composite reflectivity contour. 95

6.8 Two-dimensional discrete cosine transformation of the 600 hPa vertical velocity (m s^{-1}) field from Fig. 6.7c valid at 0330 UTC. The original plot is given in (a), while different scales of wavelengths (b) greater than 100 km; (c) between 50 and 100 km; and (d) less than 50 km are shown. See text for description of circles. 97

6.9 As in Fig. 6.8d but at (a) 0230; (b) 0300; (c) 0330; and (d) 0400 UTC. 98

6.10 Forecasts from allDA member 3 of moisture convergence ($*10^4$ g kg^{-1} s^{-1}) at (a) 800 hPa; and (b) 850 hPa valid at 0330 UTC. The green circle indicates convergence at the cold pool, and the red circle indicates convergence at the terminus of the LLJ. 100

6.11 Sounding from just ahead of the potential gravity waves in Fig. 6.9b at 0300 UTC which is used to calculate the potential phase speed following Eom (1975). 103

6.12 Individual terms of the Scorer parameter calculated from the sounding in Fig. 6.11 including (a) N^2; (b) u_{zz}; and (c) $(u-c)$. The final Scorer parameter profile is given in (d). 105
6.13 Schematic of the features likely interacting in order to generate CI for the 25 June 2013 nocturnal CI event. The parcel trajectory is also shown in black. 107

Abstract

A nocturnal maximum in precipitation exists over the Great Plains during the summer. The initiation of nocturnal storms is notoriously difficult to forecast in numerical models due to the storms often involving interactions across many scales. Additionally, most storms that develop at night are categorized as "elevated" in which the conditionally unstable source air is located above the boundary layer. While convection initiation (CI) in well-mixed, daytime boundary layers is often triggered along boundaries of surface convergence and is moderately well-understood, nocturnal CI is relatively unexplored. In this thesis, a multi-scale, GSI-based EnKF forecast system is applied to a case from 25 June 2013 to address the impact of (1) radar and conventional data assimilation; and (2) physical parameterization schemes on nocturnal CI forecasts. These results will be utilized to (3) improve the understanding of mechanisms that lead to nocturnal CI.

The simulated convection appears to have been generated by the interaction of synoptic scale lift, a surface outflow boundary, a veering nocturnal low-level jet (LLJ), and trapped gravity waves. The assimilation of conventional observations (surface, rawinsonde, aircraft, etc.) enhanced convergence at the terminus of the LLJ and strengthened ongoing convection that produced an important cold pool and resulting gravity waves. Radar assimilation showed little improvements in the CI forecast, though it better resolved earlier convection and reduced the amount of spurious precipitation. Additionally, little sensitivity was found for both planetary boundary layer and microphysical parameterization schemes.

Chapter 1

Introduction

1.1 Nocturnal precipitation maximum

There is a well-documented, but not well-understood, nocturnal maximum in precipitation in the Great Plains of the United States (US) during the summer that is critical to the hydrology and agriculture of the region (Wallace 1975; Heideman and Fritsch 1988; Moore et al. 2003; Surcel et al. 2010). Additionally, warm season precipitation forecasting remains a difficult challenge, as the accuracy in quantitative precipitation forecasts (QPFs) is consistently higher in the cool season than the summer (Heideman and Fritsch 1988; Fritsch et al. 1998; Fritsch and Carbone 2004). The agricultural industry commonly utilizes weather forecasts to determine how much of their water resources should be used for irrigation purposes and how much can be saved. Lazo et al. (2011) explored the importance of precipitation forecasts to the US economy and determined that in 2008 alone, the variation in the economic activity associated with weather variability could be 3.4%, or up to $485 billion. Flash flooding events are also most common during the summer months (Maddox et al. 1979) and result in more deaths in the United States per year than any other severe weather related hazard (NOAA 2004).

Various studies have suggested that the nocturnal maximum in precipitation over the Great Plains can be related to the eastward movement of convective systems from the higher terrain to the west (Fig. 1.1; Carbone et al. 2002; Ahijevych et al. 2004; Carbone and Tuttle 2008; Keenan and Carbone 2008). Similar maxima have been found east of the Appalachian Mountains (Parker and Ahijevych 2007) and in Australia (Keenan and Carbone 2008). During the afternoon, numerical weather prediction (NWP) models represent the timing and location of the initiation of mesoscale convective systems (MCSs) fairly well, though they are known to poorly depict the propagation characteristics (Surcel et al. 2010; Davis et al. 2004). Other factors are also likely important to the nocturnal precipitation maximum in the Great Plains, including the Great Plains nocturnal low-level jet (LLJ), potential vorticity (PV) anomalies lee of the Rocky Mountains, and convective feedbacks.

The Great Plains LLJ is a well-documented region of 15 – 35 m s^{-1} wind speeds located 300-800 m AGL that often develops over the Great Plains after sunset (Parish and Oolman 2010). It is responsible for advecting warm, moist air into the Great Plains region that enhances the environment for elevated convection (Fig. 1.2; Helfand and Schubert 1995; Higgins et al. 1997; Tollerud et al. 2008). It can also destabilize a region when advecting high θ_e air underneath cooler air aloft, or erode convective inhibition (CIN) via cooling above the LLJ caused by mesoscale ascent north of a surface front (Trier and Parsons 1993). In addition to enhancing the environment for new convective development, the LLJ also often provides potential forcing for convection, such as when interacting with a frontal boundary (Pitchford and London 1962; Augustine and Caracena 1994; Anderson and Arritt 1998) or a pre-existing mesoscale convective vortex (Schumacher and Johnson 2009). In the absence of interaction with another feature, speed convergence at the terminus of the jet can also provide a focal point for new convection

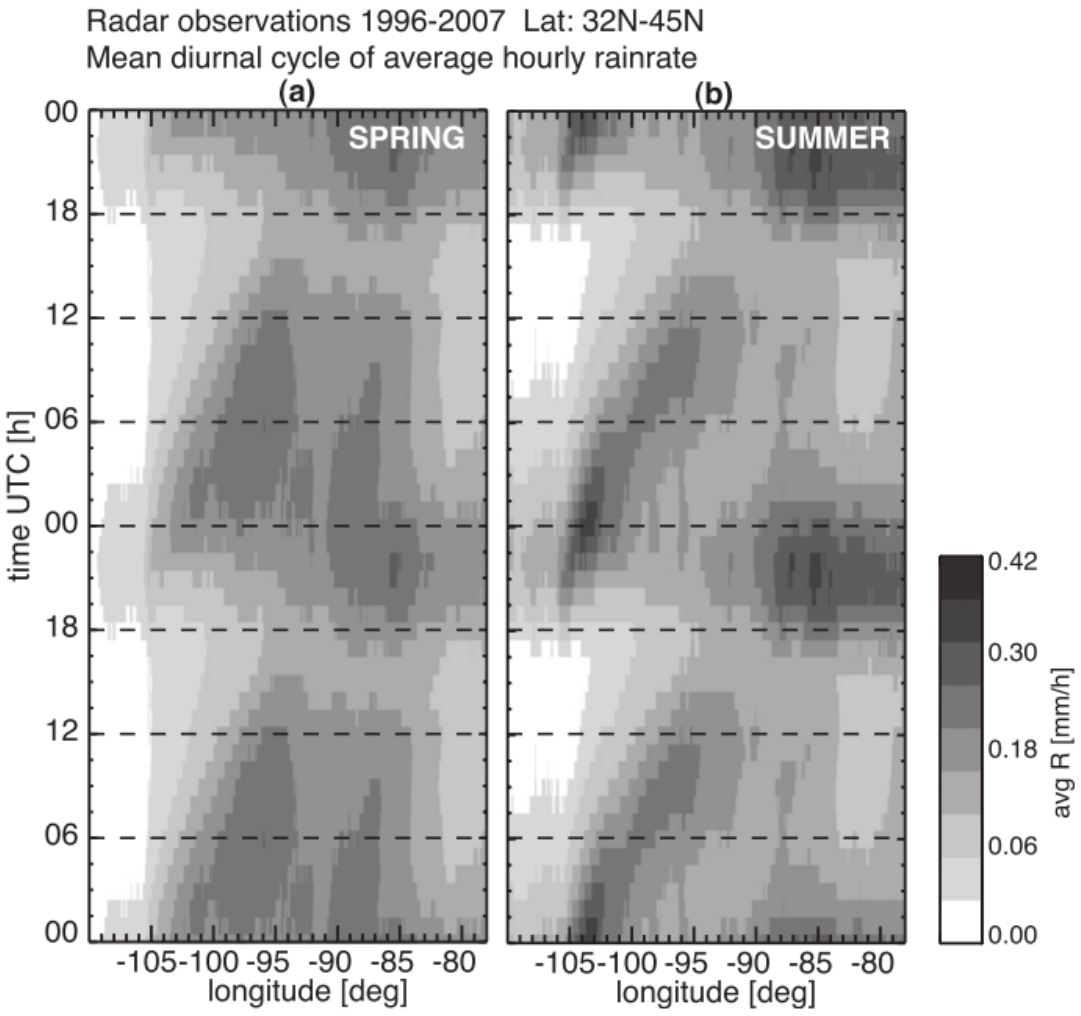


Figure 1.1: Hovmöller diagram of mean diurnal cycle of average hourly rainrates in the US between 1996 and 2007 for both spring and summer from Surcel et al. (2010). The Great Plains region of the US spans from -97° to -102° W.

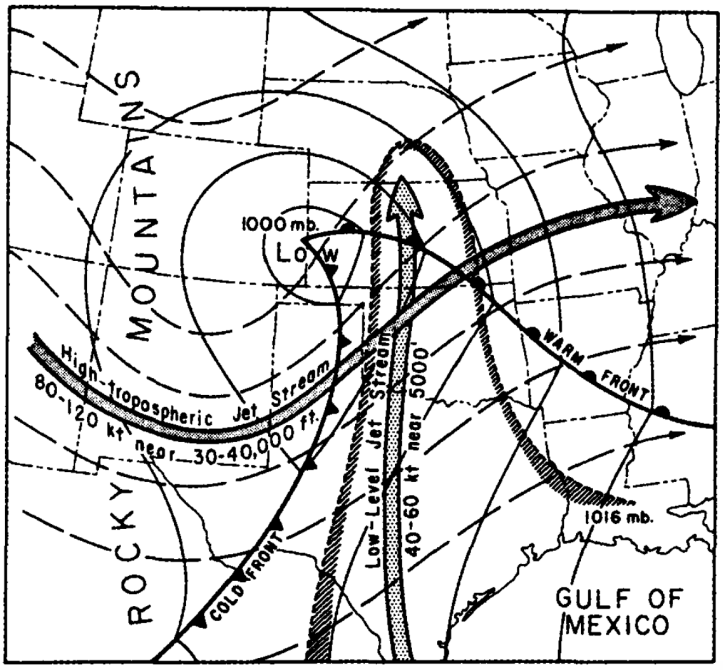


Figure 1.2: Schematic features of a severe weather outbreak in the Great Plains as aided by the developing LLJ from Newton (1967). Solid lines are sea level isobars; dashed lines are streamlines of upper-tropospheric flow. Shading outlines the general area of the LLJ moist tongue and region of potential instability

(Trier and Parsons 1993). A study by (Gale et al. 2002) noted that a majority of MCSs began to dissipate with the removal of LLJ forcing.

Trains of oscillating PV anomalies are produced in the lee of the Rockies due to localized elevated heating over the higher terrain. They are then advected by upper tropospheric winds into the Great Plains (Fig. 1.3; Tripoli and Cotton 1989a,b; Carbone et al. 2002; Li and Smith 2010) and are thought to be capable of producing deep vertical motions near the surface due to the presence of background shear. Li and Smith (2010) performed an analysis of surface observations to find a mix of stationary and east-west moving precipitation events lee of the Rockies that correlate with eastward-moving diurnal pulses of PV. They also found that these PV signals occur in both the summer and winter months; however, the winter

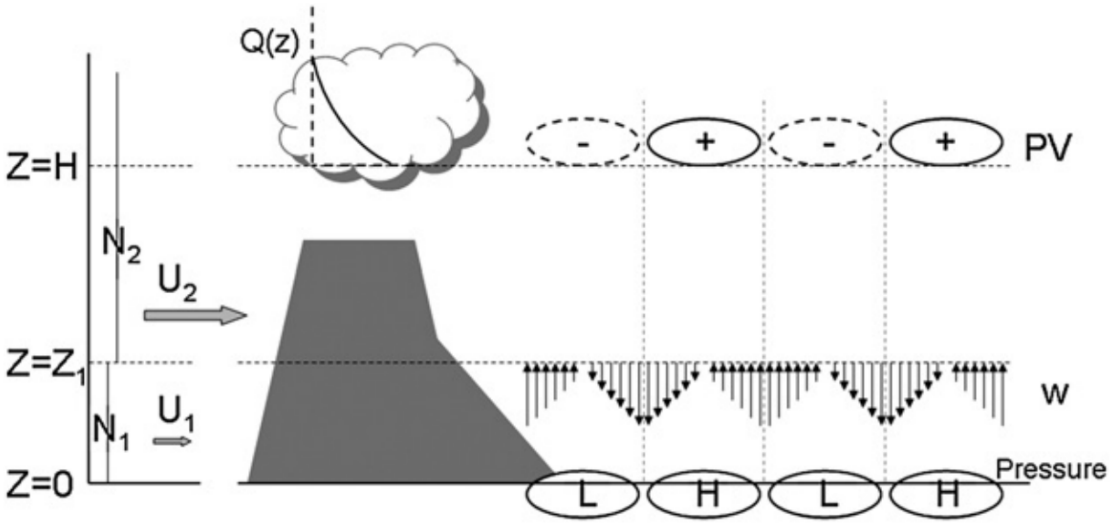


Figure 1.3: Schematic plot of PV train mechanisms in the lee of a mountain range from Li and Smith (2010). U represents the background wind, N represents the environmental stability, Z_1 is the shear level, H is the heating level, and $Q(z)$ is the vertical profile of diurnal heating over the mountain.

disturbances were weaker, moved faster, and did not tend to influence precipitation, thus indicating that the PV signal is a cause, not an effect, of the summer precipitation propagation.

Lastly, convective feedbacks (Carbone et al. 2002) represent the idea that storms forming near the high terrain of the Rocky Mountains produce cold pools or gravity waves that are able to enhance or even generate new convection downstream (Fig. 1.4). Gravity waves that come in contact with a low-level stable layer might produce what is known as an atmospheric bore that moves out ahead of the density current and is able to cause a sustained elevation of the stable layer and intense net upward displacements of air parcels (Crook 1988; Rottman and Simpson 1989) . Koch et al. (2008) observed vertical velocities of nearly 5 m s^{-1} at 2 km AGL in an atmospheric soliton (a type of wave that evolves from a bore) during the International H_2O project (IHOP) in southwest Kansas; disturbances of

this magnitude are capable of lifting conditionally unstable parcels to their level of free convection (LFC). According to climatology, elevated convection is most common east of the Rocky Mountains, northeast of surface cyclone cores, and north of surface warm fronts (Colman 1990), which is consistent with common areas of gravity wave occurrence (Jewett et al. 2003). However, internal gravity waves are inherently dispersive and need other conditions to be present in order to maintain long-lived waves and influence the generation of convection away from the source (Crook 1988).

The various mechanisms listed above provide forecast challenges for both operational meteorologists and NWP models. Apart from those, another large reason for nocturnal convective storms in the US being poorly forecast compared to convection during the daytime (Davis et al. 2004) is due to the increased occurrence of elevated convection at night. Glickman and Zenk (2000) defines elevated convection as convection where the conditionally unstable source air is located above the boundary layer. More simply, elevated convection can be characterized as any convection that develops above a near-surface stable layer, such as a sloping frontal surface or nocturnal inversion. Elevated storms can also evolve from surface-based storms over time (Corfidi et al. 2008; Parker 2008). Not all convection that initiates at night is elevated, however, as some cold pools associated with strong MCSs are able to lift surface-based air to their LFC even in an environment with a strongly stable planetary boundary layer (PBL; Billings and Parker 2012). During the IHOP project in 2002, 50% of all initiation episodes, and 80% of the episodes between 10 p.m. and 7 a.m. LST, were classified as being elevated (Wilson and Roberts 2006).

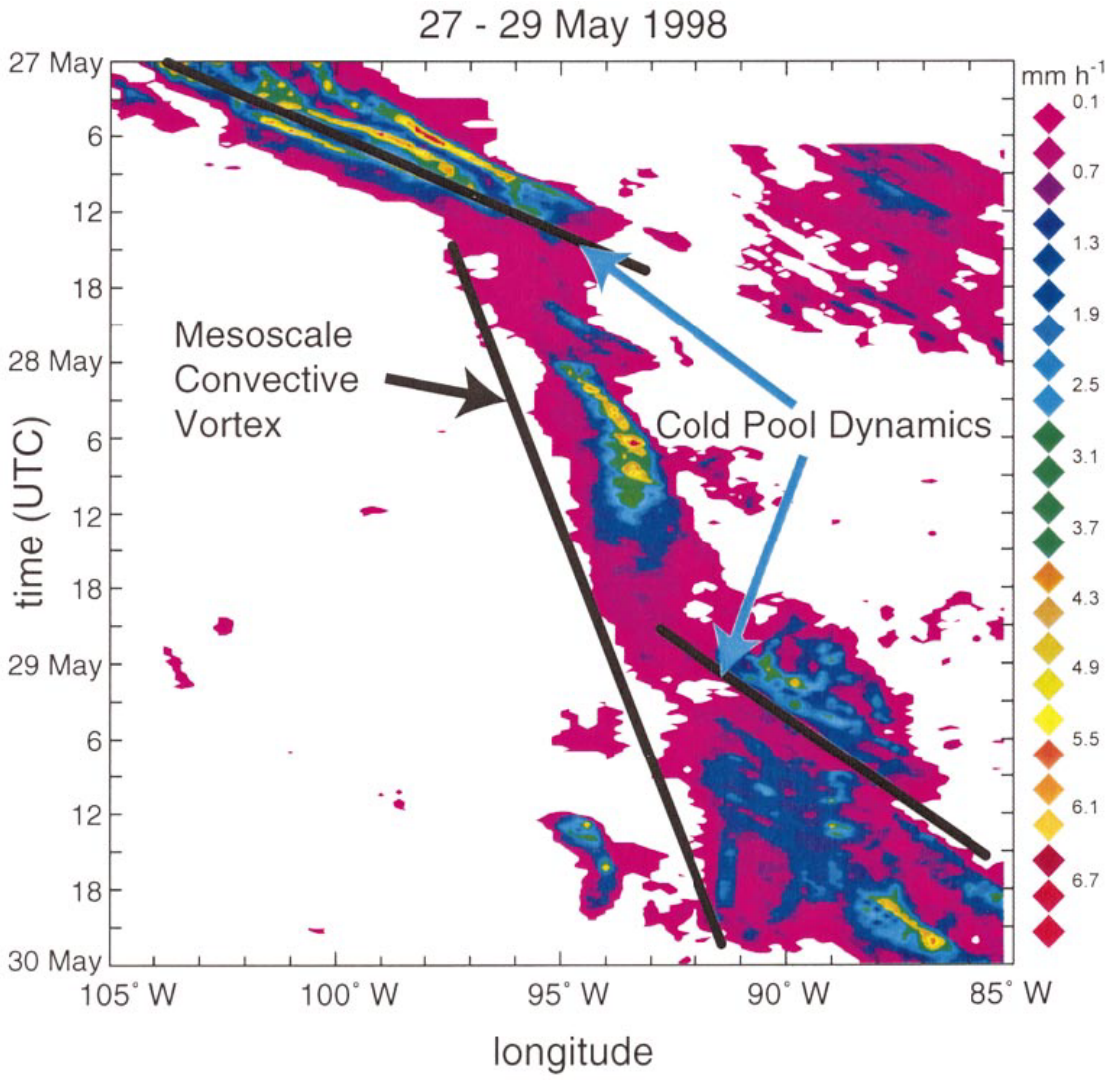


Figure 1.4: Hovmöller diagram for radar-derived rain-rate for 27-29 May 1998 in the southern Great Plains from Carbone et al. (2002). Smaller squall lines were initiated with the mesoscale convective vortex (noted as cold pool dynamics) but rapidly propagated eastward from it.

1.2 Nocturnal convection initiation

It is possible that all the above features are interrelated and contribute to the nocturnal maximum in precipitation over the Great Plains. Though much of the maximum is associated with long-lived, nocturnal MCSs, new storms can develop over the Great Plains that contribute to large rainfall totals. Determining the exact mechanisms that initiate elevated storms is a difficult challenge, especially without routine observations above the surface. Wilson and Roberts (2006) noted that most cases observed during IHOP were associated with convergent or confluent boundaries at the mid-levels. A well-documented nocturnal convection initiation (CI) episode from IHOP occurred when a trapped wave intersected a stationary convergence line at the terminus of the LLJ, producing CI above a stable nocturnal boundary layer affected by a previous MCS (Marsham et al. 2011). The authors calculated the Scorer parameter (1949) from a nearby sounding and showed that the environment, defined by a surface-based stable layer capped by near-neutral layers aloft, and combined with the southerly LLJ, favored wave trapping and thus long-lived internal gravity waves. However, there are various other wave features that potentially play a role in CI at night, including density currents, bores, and solitary waves (White and Helfrich 2012). Multiple instances of bore-produced convection were observed during both the IHOP (Wilson and Roberts 2006) and Plains Elevated Convection at Night (PECAN; Parsons et al. 2013) field projects. This study will apply an advanced data assimilation (DA) system to better understand why convection developed during a summer 2013 case from western Kansas.

Various studies have explored the immense difficulty associated with accurately predicting CI, even during the afternoon, in NWP models (e.g. Xue and Martin 2006a,b; Weisman et al. 2008; Bodine et al. 2010; Kain et al. 2013; Trier et al. 2015). Slight variations in the storm-scale or even the mesoscale environment can

produce significantly different results in regards to timing, location, and structure of new convective development (Fig. 1.5; Martin and Xue 2006). Forecasts of convection have also been shown to be sensitive to physical parameterization schemes, including different PBL and microphysics schemes (e.g. Johnson et al. 2011; Duda et al. 2014; Johnson and Wang 2016; Johnson et al. 2016). PBL schemes determine the structure of the low-level thermodynamic and moisture profiles and can often perform differently in stable conditions. Microphysics schemes are known to handle the strength and structure of cold pools differently (e.g. Dawson et al. 2010; Wheatley et al. 2014; Li et al. 2015), which are potentially important in the process of initiating new convection. Despite the fact that many convective processes also occur at a sub-grid scale, Kain et al. (2013) found that convection-allowing models provide some skill in predicting both the timing and location of diurnal CI. Johnson and Wang (2016) also found similar results for nocturnal CI events during the PECAN experiment; though they did not verify CI forecast locations, their operational forecast ensemble was nearly unbiased in nocturnal CI forecast times.

The assimilation of synoptic and mesoscale observations, as well as storm-scale radar observations, are known to improve analyses of surface boundaries or other features that might be the focal area for new storm development, as well as the mesoscale and kinematic environments in which storms form. Childs et al. (2006) improved precipitation forecasts when assimilating surface layer temperature and water vapor mixing ratio to indirectly update soil variables. Additionally, the assimilation of radar observations (radar reflectivity factor and radial velocity) have shown large impacts on improving forecasts of convection (Zhang et al. 2009; Yussouf et al. 2013; Thompson 2014; Johnson et al. 2015; Jones et al. 2015; Johnson and Wang 2016). Most of these studies have used radar observations to improve the spin-up of convective echoes, but not to specifically study the impact of DA on

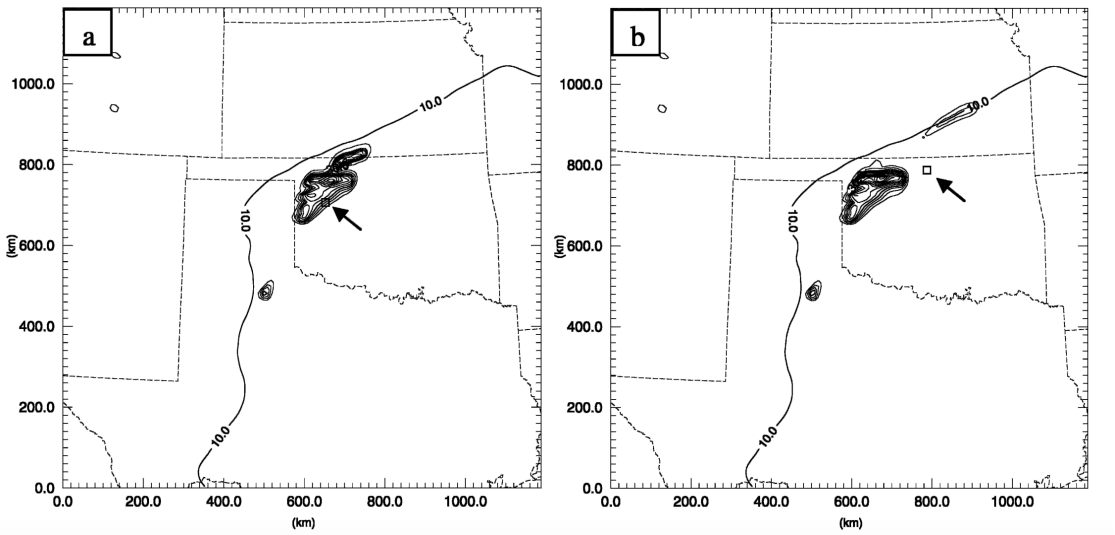


Figure 1.5: Forecast accumulated precipitation that fell in two model runs with only a 1 g kg^{-1} perturbation in the PBL moisture at the location shown in the box, from Martin and Xue (2006). The arrow in each figure, in (a) northwestern Oklahoma; and (b) north-central Oklahoma, indicates the location of the box. Contour increments are 15 mm. The 10 g kg^{-1} isopleth of water vapor at 10 m above the ground is drawn at the initial model time to indicate the location of a dryline. Only a slight perturbation in a small area was able to completely change the precipitation structure in multiple locations.

the forecasting of new storms. Gasperoni et al. (2013) assimilated radar-derived refractivity measurements, which provide information on near-surface moisture content, and found that the assimilation was able to correct low-level moisture errors and improve CI forecasts. More recently, Sobash and Stensrud (2015) improved forecasts of CI in the southern Great Plains by using an ensemble Kalman filter (EnKF) to assimilate mesonet and conventional surface observations (Fig. 1.6). They determined that the improvements largely resulted from a more accurate representation of PBL moisture profiles. The EnKF method of DA, which will be applied for this study, has the advantage of flow-dependent background error covariances compared to the static covariances assumed by variational DA schemes. This produces more accurate spatial and cross-variable correlations between the state variables and observations (given that a number of assumptions are not broken) and thus also a more accurate final analysis compared to 3DVar (Johnson et al. 2015).

Our study will apply an advanced, multi-scale DA system to a nocturnal CI case from central Kansas during 25 June 2013. On 24 June, a late-afternoon MCS initiated off of a dryline in southwestern Kansas before dissipating in the early evening hours of 25 June. Operational forecasts for the area predicted that due to the loss of daytime heating, storm chances would diminish rapidly by late evening. However, convection initiated slightly before 0300 UTC with no apparent boundaries near it. The term "multi-scale" will refer to a DA and forecast system that resolves a range of scales, from the larger synoptic scale on an outer domain, down to the storm-scale on an inner, convection-allowing domain. Observations that are designed to sample these different scales will be assimilated during the DA process on the different grids in order to provide unique analyses that best estimate the state.

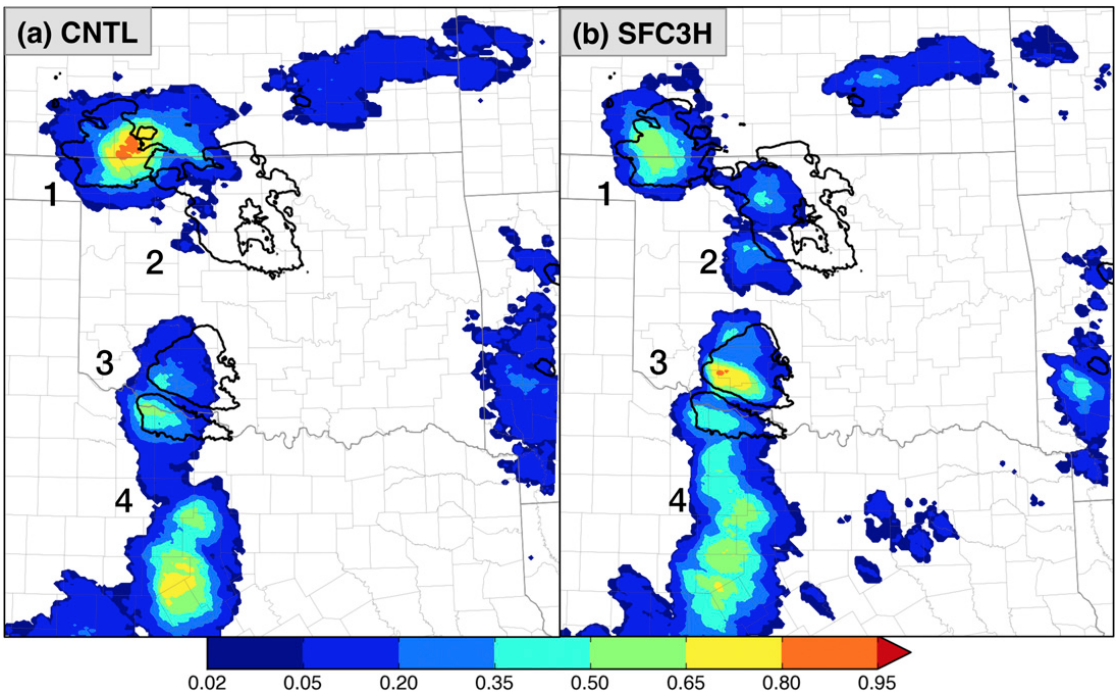


Figure 1.6: One hour forecast probabilities (2100 – 2200 UTC) of composite reflectivity (CREF) > 25 dBZ for (a), a control forecast initialized from the NCAR mesoscale ensemble with no DA; and (b) a forecast initialized after 3 hours of surface data assimilation from Sobash and Stensrud (2015). Maximum observed CREF > 25 dBZ from 2100 to 2200 UTC is shaded in black.

Results from this advanced DA system will be used to address three main goals: (1) what is the impact of radar and in-situ DA for nocturnal CI forecasts? Both observation types are now commonly assimilated into operational forecast models. However, separating them into different assimilation experiments will provide information on which features and scales are most important for the model to resolve in order to specifically forecast nocturnal CI. Since few previous studies have specifically attempted to simulate nocturnal CI, this work can also be approached as a feasibility study of whether convection-allowing forecast systems are able to reproduce some of the unique interactions that lead to CI at night. Also addressed in this thesis is: (2) what roles do physical parameterization schemes (PBL and microphysics) play in simulating nocturnal CI? Though they can produce very different results for diurnal CI simulations, the largest differences between these schemes often occur near the surface and below the likely layers of initiation for most nocturnal convection. Lastly, these results will be used to (3) improve the understanding of mechanisms that lead to nocturnal CI. As previously mentioned, the features responsible for triggering convection at night are often unclear due to the lack of high-frequency observations above the surface. Though it is difficult to verify whether the simulated CI mechanisms are true, NWP models provide a proxy for pinpointing specific features that are likely to be important.

The thesis is organized as follows. A description of the case from 25 June, 2013 is presented in chapter 2. Chapter 3 will outline the model and DA configurations used in this study. Chapter 4 provides an overview of the DA results as well as the forecast results related specifically to CI. Chapter 5 presents the sensitivity results for different parameterization schemes. The dynamical results related to the specific mechanisms responsible for generating CI will be discussed in chapter 6. Lastly, an overall discussion of results, conclusions, and future work are included in chapter 7.

Chapter 2

Overview of 25 June 2013 CI event

2.1 Synoptic and mesoscale environment

The focus of this study will be a cluster of isolated convection that initiated in northwestern Kansas in a stable environment with no obvious convergent boundaries nearby. Upper level flow was mostly weak and southwesterly, although a shortwave trough was present east of the Rocky Mountains at 300 hPa down to 500 hPa (Fig. 2.1a) that can be traced back to the northern Pacific coast. Prior to the passage of the perturbation, upper-level flow was not supportive of convection becoming particularly organized. As the upper-level wave moved over the Rockies, deep southwesterly flow increased and a lee trough developed closer to the surface (Fig. 2.1b). An associated surface low became apparent in southeastern Wyoming during the early afternoon of 24 June.

A bulging dryline extended southward from this surface low into the Texas Panhandle (Fig. 2.2) with surface dew point temperatures of 61 °F in Dodge City, Kansas and 32 °F in far southeastern Colorado at 2200 UTC. The warm front associated with the surface low was draped across southern Nebraska and pushed north into the evening hours. Surface flow throughout most of northern and eastern Kansas was weak (10 kts or less), though wind speeds were higher in parts of western Kansas and the Oklahoma/Texas Panhandle. The late afternoon environment

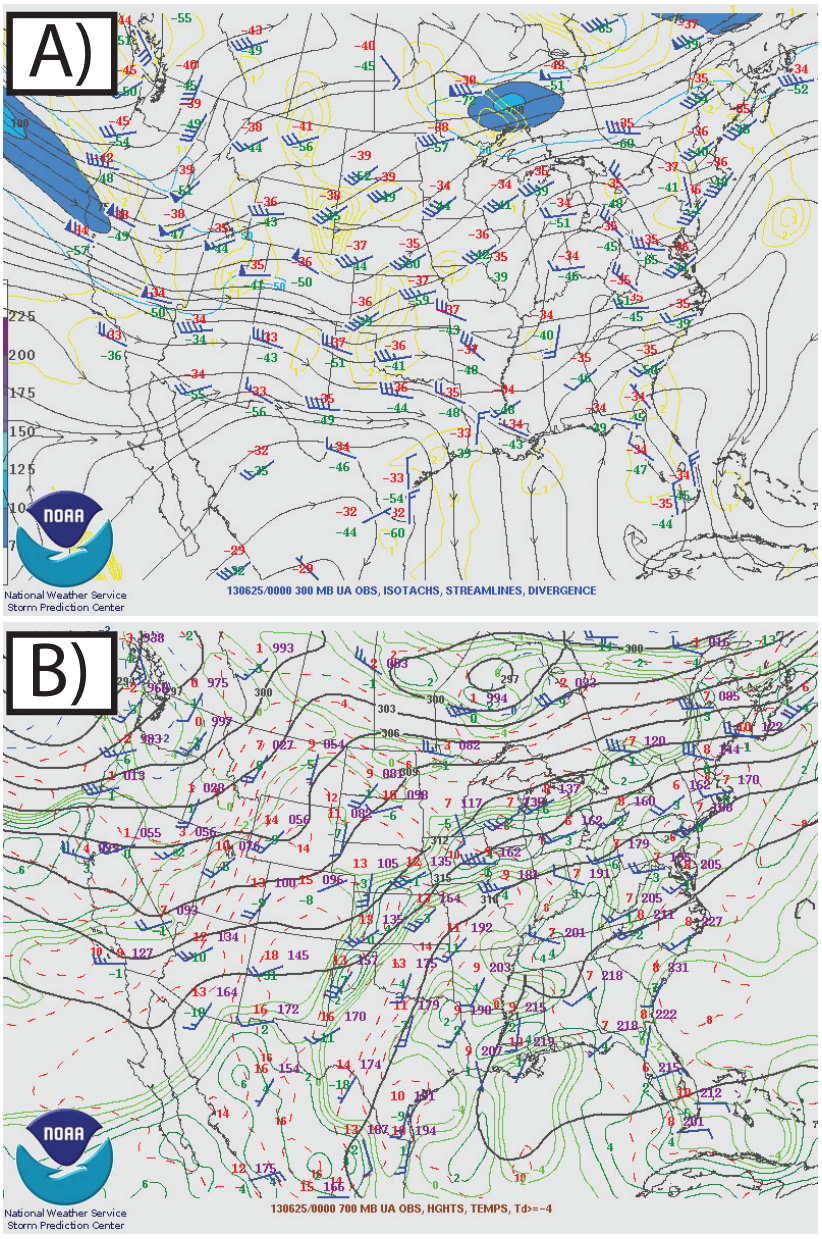


Figure 2.1: Upper-air analyses and observations at 0000 UTC on 25 June of (a) 300 hPa isotachs (fill), streamlines (black contours), and divergence (yellow contours); and (b) 700 hPa heights (black contours), temperature (red contours), and dewpoints > -4 °C (green contours).

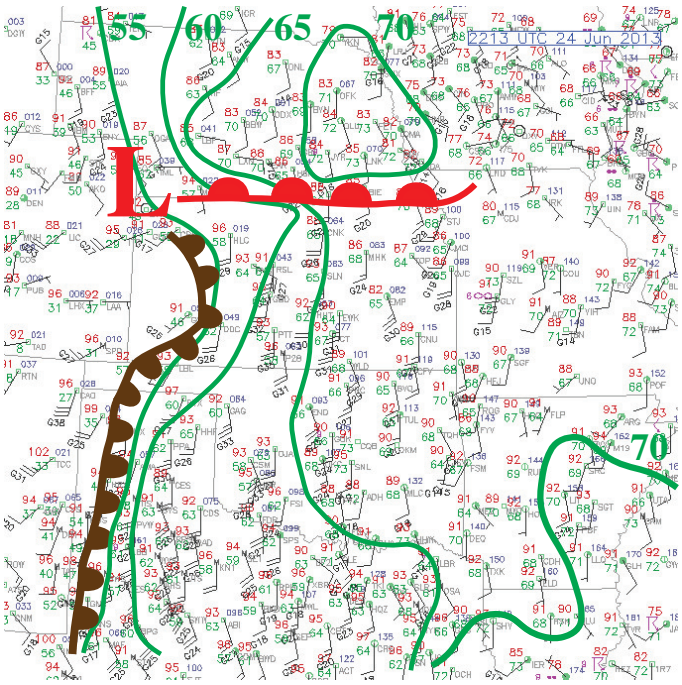


Figure 2.2: Surface observations across the Great Plains at 2213 UTC on 24 June. The brown line indicates the subjectively analyzed location of the surface dryline at 50 °F, while the red line indicates the approximate location of the warm front. Also contoured are the 5 °F isodrosotherms.

on 24 June in the warm sector was classified as strongly capped but moderately unstable (300 J kg^{-1} of surface-based convective inhibition [CIN] and 2200 J kg^{-1} of surface-based convective available potential energy [CAPE] in Topeka at 0000 UTC). The 0000 UTC sounding on 25 June from Dodge City, Kansas was within the cold pool from later convection, though the 1200 UTC sounding on 24 June showed steep mid-level lapse rates but little low-level moisture. Dew points were able to increase in those 12 hours from 13 °C to 21 °C.

Storms formed prior to the convection of interest earlier that afternoon in southwest Kansas along the dryline at 2100 UTC and moved eastward (Fig. 2.3). They merged into a small MCS, possessing their best squall line-like structure at 2330 UTC before slowly dying out by 0500 UTC (Fig. 2.3c-d). Around the time

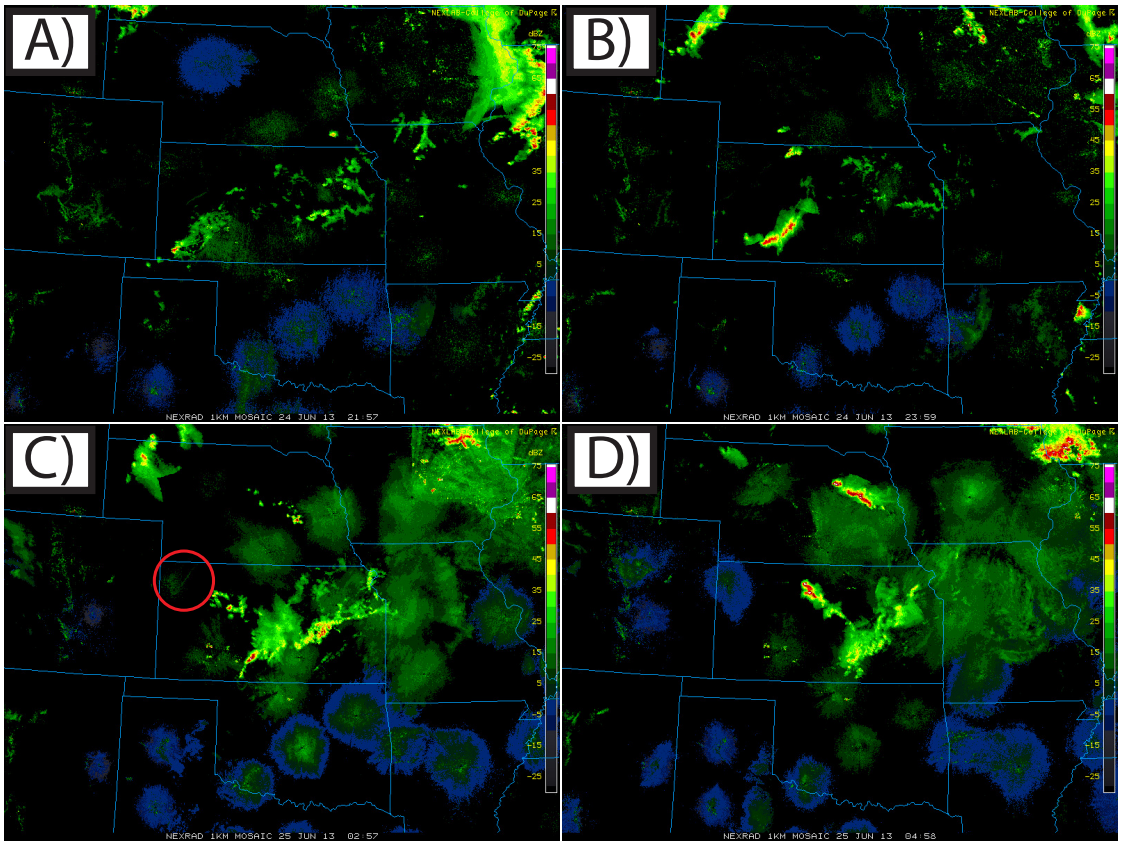


Figure 2.3: Radar observations of 1 km AGL reflectivity valid at (a) 2200 UTC on 24 June; (b) 0000 UTC; (c) 0300 UTC; and (d) 0500 UTC on 25 June. The red circle in (c) indicates a radar fine line moving northwestward.

that the dryline began to retreat back westward (Fig. 2.4), signs of an outflow boundary moving northward through northwest Kansas could also be seen on the observed 1 km AGL reflectivity image (Fig. 2.3c). Reports of large hail and high wind gusts were associated with this southern system (Fig. 2.5, see cluster of reports in southern Kansas).

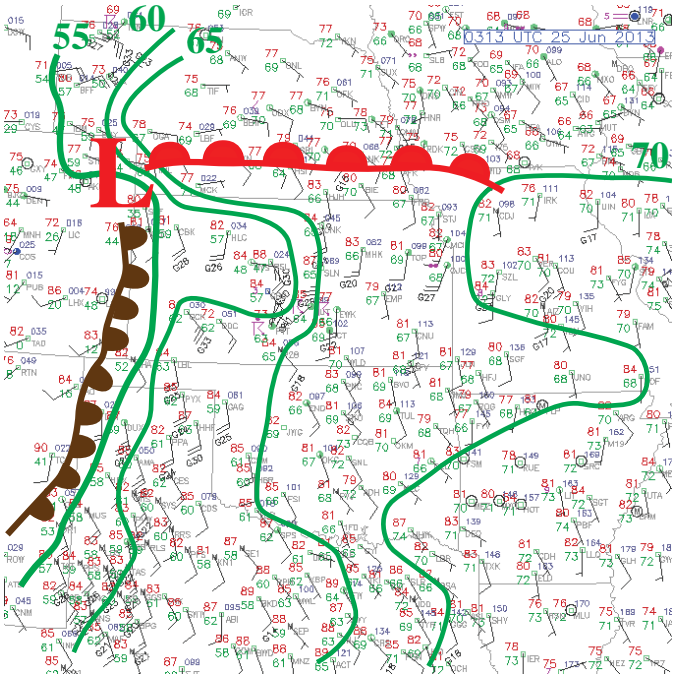


Figure 2.4: As in Fig. 2.2 but at 0313 UTC on 25 June.

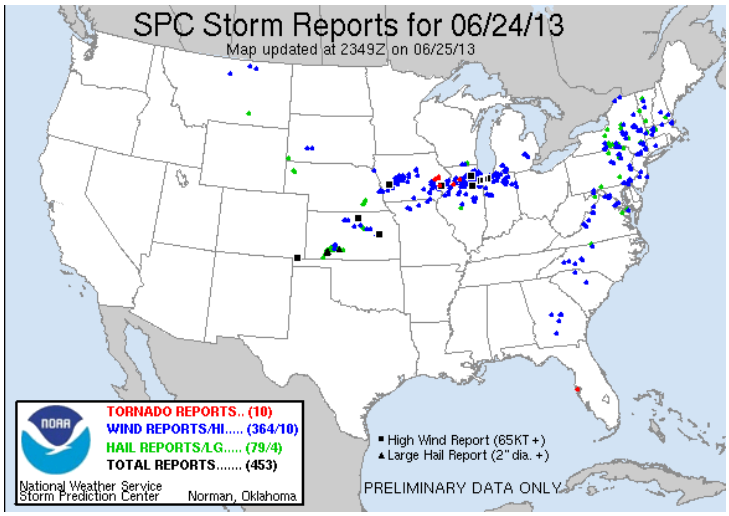


Figure 2.5: Preliminary storm reports from the Storm Prediction Center between 1200 UTC on 24 June and 1200 UTC on 25 June. Black icons indicate high wind or large hail reports.

2.2 Operational forecasts

Most operational forecasts from the National Weather Service (NWS) and Storm Prediction Center (SPC) assumed that storms would be unlikely to develop overnight due to a stabilizing boundary layer, as well as the cold pool from previous convection spreading northward (NOAA 2013). An Area Forecast Discussion (AFD) from the Dodge City, Kansas NWS office at 2100 UTC on 24 June stated: "after the shortwave trough passes tonight, and by the loss of daytime heating, storm chances will diminish rapidly by late evening". The SPC echoed that sentiment at 0200 UTC on 25 June: "the boundary layer is cooling and CIN is increasing rapidly across the area, which should aid in weakening the ongoing storm and likely preclude additional development from western Kansas into south central Nebraska". The NWS office in Hastings, Nebraska however did catch on to the possibility of convection continuing into the overnight hours: "mid-level perturbation currently advancing east from the Rockies... promoting some increasing omega... guidance continues to suggest the axis of a 45-55 850 mb jet streak will develop across portions of the southern and central Plains tonight... 20-30% POPS [probability of precipitation] are presented to the entire central watch area".

2.3 Convective history

Convection initiated in the evening with storms forming in northwestern Kansas by 0230 UTC (Fig. 2.6; circled area). This initiation episode will be the focus of this study. The cells were originally isolated but began to merge into a mesoscale feature at 0500 UTC (Fig. 2.7c). As they moved eastward, severe hail and wind reports (including one greater than 65 kts) were noted in northern Kansas (Fig. 2.5); see cluster of reports in northern Kansas). More storms began to initiate along

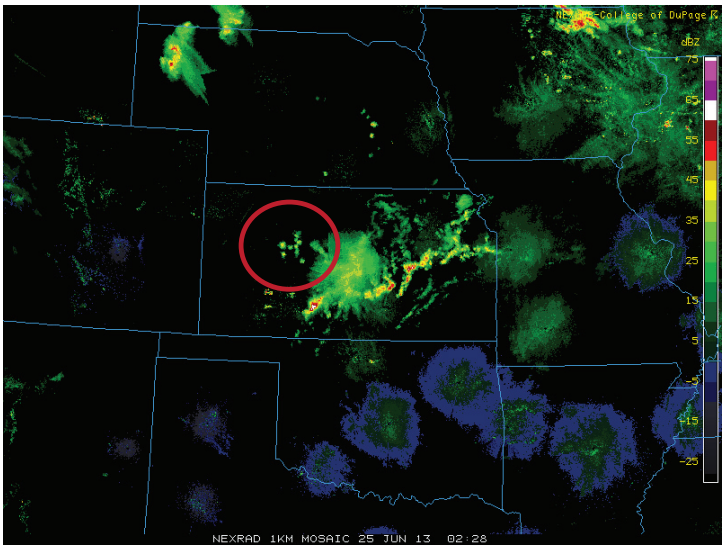


Figure 2.6: Radar observations of 1 km AGL reflectivity valid at 0230 UTC. The circled area indicates the initiation episode of interest.

both the northern and southern ends of a northwest to southeast oriented convective line (only the original initiation point will be studied). At 0800 UTC, a convective core in the middle of the line began to strengthen and move with more of a southerly component than the rest of the line. At 0900 UTC, this storm produced a supercell-like hook structure (Fig. 2.7d). Additional convection initiated further ahead of this line in eastern Nebraska at 1100 UTC though multiple segments of the line began to weaken after that. Most of the original structure fell apart by early morning.

There were no boundaries present near the initiation location on the surface charts (Fig. 2.4). The nearest radiosonde observation to this point at Dodge City, Kansas was within the cold pool of the previous convection at 0000 UTC, though it stands as a decent first-guess analysis of the environment that these storms developed in. Since radar fine-lines were seen moving northward in northwestern Kansas prior to this episode initiating, it is likely that the new convection formed above or within the cold pool of the southern convection. The late afternoon

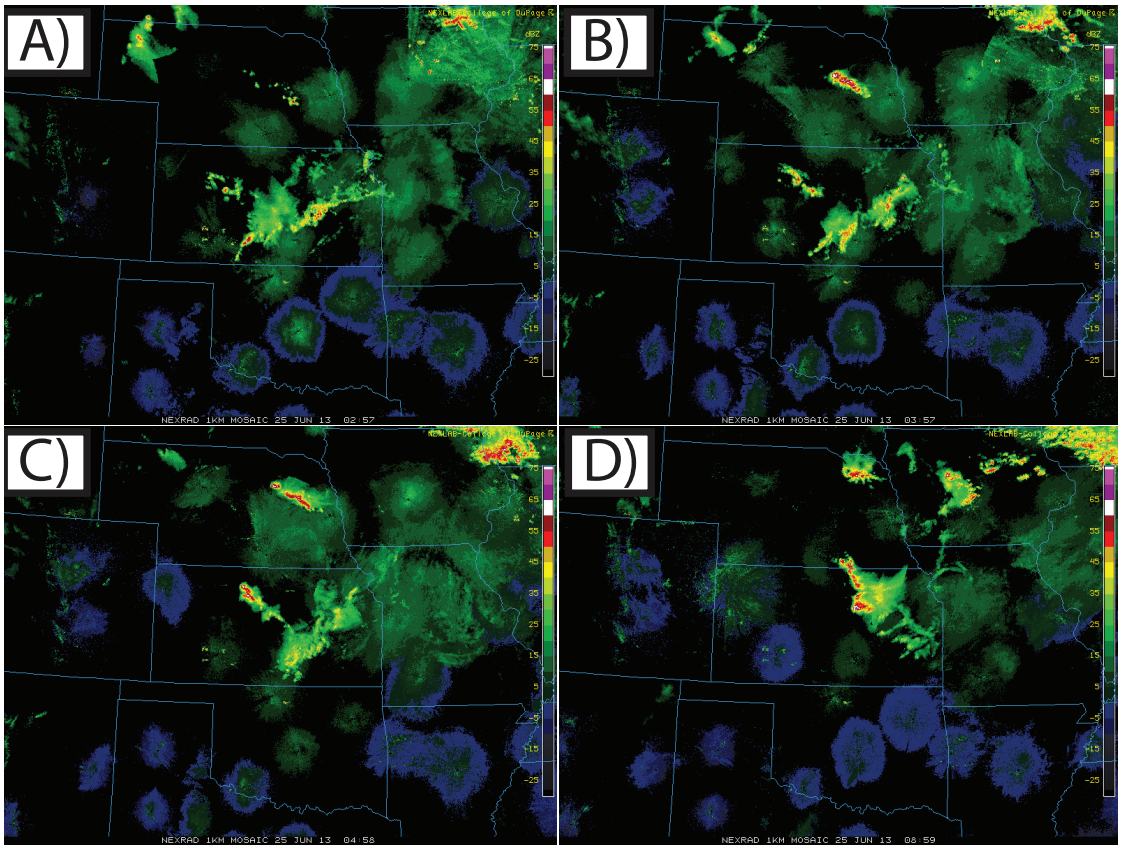


Figure 2.7: Radar observations of 1 km AGL reflectivity valid at (a) 0300 UTC; (b) 0400 UTC; (c) 0500 UTC; and (d) 0900 UTC on 25 June.

sounding (Fig. 2.8a) had a strong surface-based inversion with surface-based CIN values of near 400 J kg^{-1}. However the mid-level lapse rates in the area were very steep (analyzed as over 8.5 K km^{-1} via the SPC mesoanalysis), producing over 1500 J kg^{-1} of most-unstable CAPE (MUCAPE) at KDDC and indicating the possibility for elevated convection to form. Additionally, a strong LLJ was present at the 1200 UTC sounding from KDDC. (Fig. 2.8b). The jet max at 1200 UTC was observed as 56 kt at 843 hPa (1524 m AGL).

Almost no observations, other than conventional surface stations and upper air soundings, are available to analyze the particular cause of this new CI in northwestern Kansas. This study will use modeling results to infer the mechanisms that may be responsible, though it will be impossible to verify whether these actually occurred. However, using these results, one can infer possible mechanisms that may be responsible for generating nocturnal CI and apply them to other cases. Additionally, we will be able to understand through this study whether a 4 km NWP simulation is able to correctly resolve some of these important features.

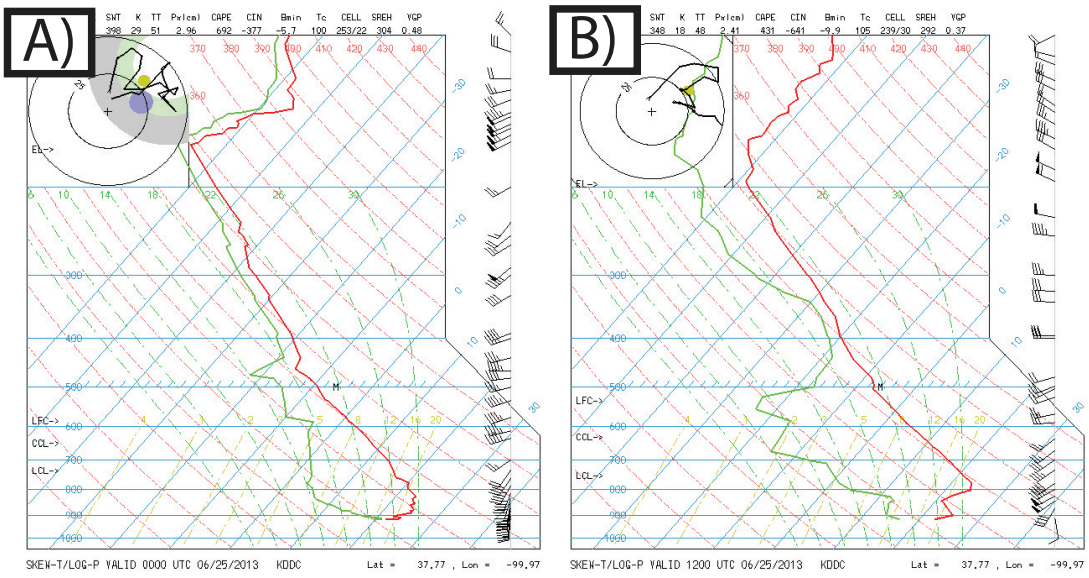


Figure 2.8: Soundings from KDDC at (a) 0000 UTC; and (b) 1200 UTC on 25 June.

Chapter 3

Methodology

3.1 Model configuration

3.1.1 Initial and lateral boundary conditions

All simulations presented in this study utilize the Weather Research and Forecasting (Skamarock et al. 2008) NWP model with the advanced research core (WRF-ARW) version 3.6.1. WRF is widely used and well-documented throughout the field of meteorology for both research and operations. An outer domain is configured with 12 km grid spacing and 50 terrain-following vertical levels over a 326 x 259 grid point domain (Fig. 3.1). These vertical grid levels are stretched, with the tightest spacing near the surface up to 2.5 km AGL and then gradually spreading above until the model top at 50 hPa (Fig. 3.2). The outer domain is created at the beginning of the simulation by downscaling the operational National Centers for Environmental Prediction Global Forecast System (NCEP GFS) analysis to the WRF domain using the WRF Preprocessing System (WPS) at 0000 UTC on 24 June. To generate 40 ensemble members, random perturbations are added through the random-cv facility in the WRF Data Assimilation (WRFDA; Barker et al. 2004) package. Perturbation standard deviations of 1.9 m s^{-1} for

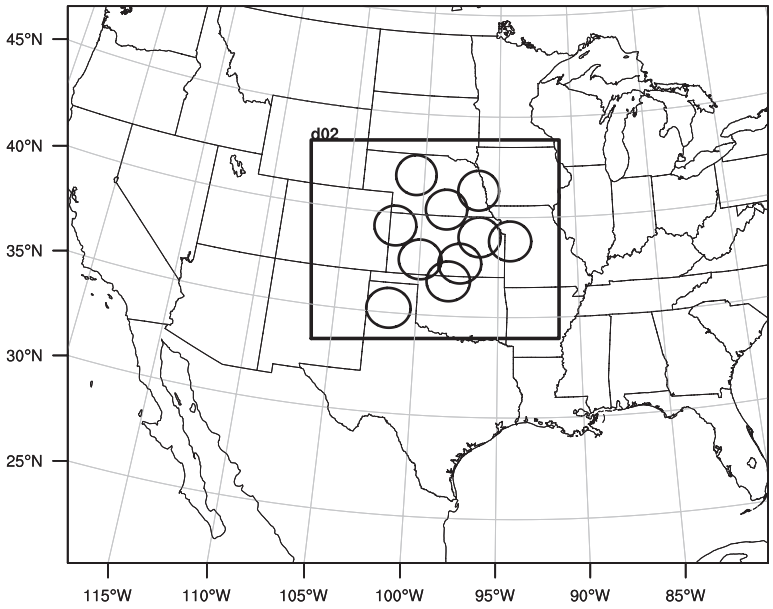


Figure 3.1: Domain configurations for all simulations. The outer box represents the outer, 12 km domain, while the inner box is the convection-allowing, 4 km domain. Each circle within the inner domain represents a WSR-88D radar that was assimilated.

the horizontal wind, 0.6 K for temperature, 0.3 hPa for model pressure perturbation, and 0.9 g kg^{-1} for water vapor mixing ratio are added (Wang et al. 2008; Johnson et al. 2015). GFS forecasts are also used to produce the lateral boundary conditions (LBCs) for the outer domain; the pert_wrf_bc program from the Data Assimilation Research Testbed (DART) and the National Center for Atmospheric Research (NCAR) is used to randomly perturb the LBC for each member similar to the initial conditions.

After DA on the outer domain (detailed in the next section) is finished, an inner, convection-allowing domain with 4 km spacing of 346 x 277 horizontal levels is initialized within the outer domain (inner box in Fig. 3.1) which provides the initial and lateral boundary conditions. Chasteen et al. (2016, personal communication)

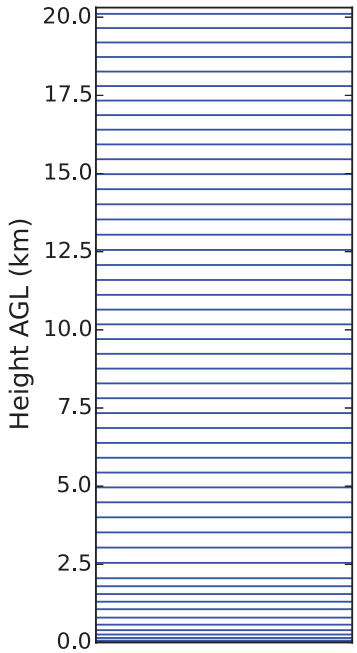


Figure 3.2: Stretched vertical grid spacing for 50 terrain-following vertical levels in all simulations.

found large sensitivity to the nesting configuration for a long-track, nocturnal MCS. They discovered that switching from one-way to two-way nesting allowed a much more developed system, similar to the observed MCS, to form in their simulation. Thus we also utilize two-way nesting in which forecasts from the inner domain are allowed to update the outer domain as well. The inner domain also has the same 50 terrain-following, stretched vertical levels. After assimilation has completed on the inner domain, free forecasts from the final EnKF analyses are launched out to 6 h lead times.

3.1.2 Physical parameterizations

Fixed physical parameterizations are used for each of the 40 members and are listed as follows. Results in chapters 3 and 4 will utilize the Mellor-Yamada-Nakanishi-Niino (MYNN; Nakanishi and Niino 2004, 2009) PBL scheme, as well

as the WRF single-moment 6-class (WSM6; Hong and Lim 2006) and Lin (Lin et al. 1983) microphysics schemes. Additionally, the Noah land surface model (Ek et al. 2003), RRTMG longwave (Iacono et al. 2008) radiation, Goddard shortwave radiation (Tao et al. 2003), and the Grell-Freitas (Grell and Freitas 2013) cumulus parameterization schemes are used for all simulations. Chapter 5 will also examine forecast sensitivities to different PBL and microphysics schemes. 4 km horizontal grid spacing on the inner domain, though not capable of fully resolving all convective details, "allows" convection to form with similar structures to that observed. Thus the cumulus parameterization is turned off for the inner domain simulations. A summary of all parameterization schemes is given in Table 3.1. Coniglio et al. (2013) notes that the local closure, 1.5-order MYNN scheme performs significantly better than other schemes in that it is nearly unbiased in PBL depth, moisture, and potential temperature, thus giving confidence in its use in convection-allowing configurations of WRF. Various studies have demonstrated the large role that microphysics processes and schemes play in the evolution of convection, through changes in the phase speed of convective systems, as well as rainfall magnitudes (Fritsch and Carbone 2004; Dawson et al. 2010). During data assimilation, the WSM6 scheme is utilized due to computational efficiency; the reflectivity observation operator for DA associated with WSM6 follows Johnson et al. (2015; 2016a). While performing diagnostics for the microphysics sensitivity studies described in chapter 5, the Lin microphysics scheme was subjectively chosen for the forecast period due to its ability to produce CI with a similar orientation and shape to that which was observed. The Lin scheme is a single-moment, bulk microphysics scheme that predicts the mixing ratios of cloud and rain water, ice, snow, graupel, and hail. French and Parker (2008) successfully used the scheme to simulate the initiation of both supercells and an MCS in WRF, and it has also been shown to perform well for other convective modes (e.g. Nasrollahi et al. 2012).

Parameterization	**Scheme**
PBL	1.5-order MYNN
Microphysics (DA)	WSM6
Microphysics (Forecast)	Lin
Land Surface Model	Noah
Longwave Radiation	RRTMG
Shortwave Radiation	Goddard
Cumulus	Grell-Freitas (outer domain only)

Table 3.1: Physical parameterization schemes used for all non-physics sensitivity experiments.

3.2 Data assimilation system configuration

3.2.1 The ensemble Kalman filter

The ensemble Kalman filter (EnKF) method for DA has the advantage of flow-dependent covariances compared to the static covariances assumed by variational DA schemes such as 3DVar. This produces more accurate spatial and cross-variable correlations between the state variables and observations (Fig. 3.3). The EnKF used in this study is based on the ensemble square root filter (EnSRF) detailed in Whitaker and Hamill (2002); it updates a prior estimate of the atmospheric state $\boldsymbol{x}^b$, valid at some time with the information given in the observations $\boldsymbol{y}^o$, to arrive at an analysis of the atmosphere $\boldsymbol{x}^a$ as in (3.1). Bold symbols indicate vectors, while overbars denote the ensemble mean, and the deviation from the mean is denoted by a prime symbol. In order to update the ensemble mean, a Kalman gain matrix $\boldsymbol{K}$ is calculated (3.3) to give an appropriate weight to the observations, which have error covariance $\boldsymbol{R}$, and the background, which has error

covariance $\boldsymbol{P}^b$. In order to map the background into observation space, a forward operator $\boldsymbol{H}$ is required. When using an EnSRF, each observation is assimilated serially and a modified Kalman gain $\widetilde{\boldsymbol{K}}$ is used to update ensemble deviations from the ensemble mean (3.2 and 3.4).

$$\overline{\boldsymbol{x}}^a = \overline{\boldsymbol{x}}^b + \boldsymbol{K}(\boldsymbol{y}^o - \boldsymbol{H}\overline{\boldsymbol{x}}^b) \tag{3.1}$$

$$\boldsymbol{x}'^a = \boldsymbol{x}'^b - \widetilde{\boldsymbol{K}}\boldsymbol{H}\boldsymbol{x}'^b \tag{3.2}$$

$$\boldsymbol{K} = \boldsymbol{P^b H^T}(\boldsymbol{H P^b H^T} + \boldsymbol{R})^{-1} \tag{3.3}$$

$$\widetilde{\boldsymbol{K}} = \alpha \boldsymbol{K} \tag{3.4}$$

where

$$\alpha = (1 + \sqrt{\boldsymbol{R}/\boldsymbol{H P^b H^T} + \boldsymbol{R}})^{-1} \tag{3.5}$$

The quantities $\boldsymbol{P}^b\boldsymbol{H}^T$ and $\boldsymbol{H}\boldsymbol{P}^b\boldsymbol{H}^T$ can be estimated using the ensembles following Whitaker and Hamill (2002).

The general theory and equations behind the EnKF can be further explored in Whitaker et al. (2008) and a general review of the filter for atmospheric DA purposes is given in Houtekamer and Zhang (2016). The Gridpoint Statistical Interpolation (GSI) program is used for the calculations of the forward operators ($\boldsymbol{H}$ in 3.1-3.5) for the update step of the DA equations (Kleist et al. 2009). A GSI-based hybrid EnKF-Var system is currently in use in the NCEP operational centers (Hamill et al. 2011b; Wang et al. 2013; Wang and Lei 2014). The GSI-based EnKF used in this study was extended to be able to directly assimilate radar observations (reflectivity and radial velocity; Johnson et al. 2015). Johnson et al. (2015) also compared 3DVar to a GSI-based EnKF data assimilation system over 10 diverse cases of mid-latitude convective-scale precipitation forecasts and found that the GSI-based EnKF forecasts are more skillful than 3DVar both with and without storm-scale radar assimilation. This is attributed to a more accurate analysis of both the mesoscale and storm-scale environments. For the outer domain mesoscale

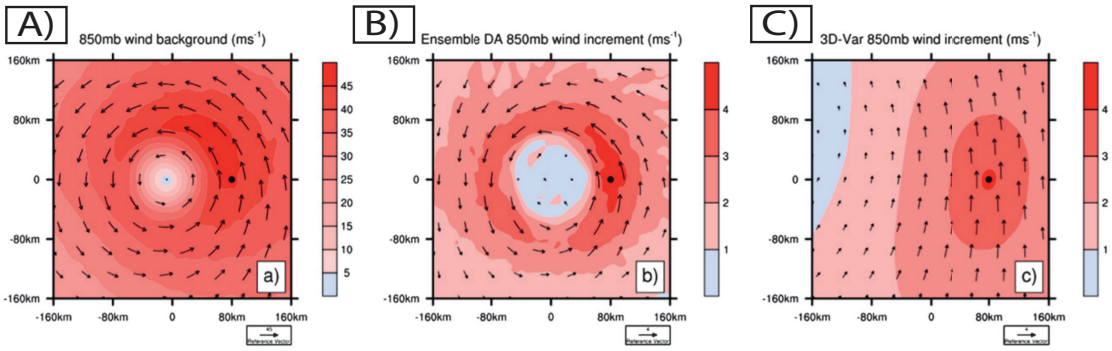


Figure 3.3: Illustration of the potential of an EnKF for making meteorologically reasonable analysis increments from Hamill et al. (2011a). (a) Mean background forecast of 850 hPa winds. Assuming an observation 10 m s^{-1} greater than the background is available at the black dot. (b) Wind analysis increment from the assimilation of the single observation when using an EnKF, and (c) Wind analysis increment when using an average of the ensemble covariance over all locations around the hurricane, a surrogate for the increment that may be expected from a 3DVar system.

assimilation, the state variables updated by the EnKF are as follows: meridional and zonal wind, potential temperature, water vapor mixing ratio, geopotential height, and column perturbation dry air mass (a proxy for pressure). For the inner domain storm-scale assimilation, the above state variables are updated in addition to the mixing ratios of rain, snow, and graupel.

3.2.2 Observational dataset

The data utilized in this study include conventional and radar observations. Conventional observational data will hereby refer to synoptic and mesoscale data obtained from the Climate Forecast System Reanalysis project at the NOAA Operational Model Archive and Distribution System (NOMADS); they include rawinsondes, surface METAR and mesonets, Aircraft Communication Addressing and Reporting System (ACARS), NOAA wind profilers, and ship and buoy observations. Earlier studies have shown large improvements when also assimilating radar observations using an EnKF (e.g. Zhang et al. 2009; Yussouf et al. 2013; Thompson 2014; Marquis et al. 2014; Johnson et al. 2015; Snook et al. 2015). A major difference between this and other studies is that previous work mainly focused on the impact of radar DA in spinning up pre-existing convection, not specifically in evaluating the use of radar observations for forecasting the initiation of new convection. The radar observations (radar reflectivity factor and radial velocity) are NEXRAD level 2 data obtained from the National Centers for Environmental Information (NCEI). The exact WSR-88D radar locations that are assimilated in this study can be seen as the circled areas in Fig. 3.1.

Before being assimilated, all radar data is quality-controlled and preprocessed through the Warning Decision Support System – Integrated Information (WDSS-II; Lakshmanan et al. 2007) software package. The w2qcnn utility is used to remove non-meteorological echoes such as anomalous propagation and biological

echoes. We found that also setting any reflectivity observations less than 5 dBZ to -35 dBZ within GSI (to be consistent with the minimum reflectivity allowed in WRF) also helped with reducing spurious convection during the assimilation cycles. Velocity data are dealiased using a two-dimensional dealiasing algorithm described in Jing and Wiener (1993) and then thresholded based on the reflectivity data; any velocity data where the corresponding reflectivity observation is less than 5 dBZ is omitted. Additionally, velocity observations are rejected if the difference from the background value is greater than 30 m s^{-1}, though this likely only occurs in cases of extreme aliasing missed during preprocessing. Reflectivity observations are not rejected based on an observation-background difference, as large differences could result from areas of spurious convection in the background or early cycles in which storms are observed that are not yet in the background. In these cases, a large observation-background difference is needed to improve the analysis. The observation error of radar reflectivity and radial velocity observations are set to 5 dBZ and 2 m s^{-1}, respectively, following Johnson et al. (2015).

3.2.3 Error treatment

Additional techniques are employed in this study to bypass common DA problems. To circumvent the problem of assimilating observations at a different time than the analysis, first guess at appropriate time (FGAT) is applied to the cycles on the outer domain by outputting background fields at 30 minute intervals for 1.5 h before and after the analysis time. Background fields are linearly interpolated in time for comparison to observations at their time. Additionally, asynchronous assimilation (Sakov et al. 2010) is employed on the outer domain, in which the ensemble covariance matrix is calculated between observation priors valid at individual observation times, and background priors in model space valid at the analysis time.

Covariance localization following a Gaspari and Cohn (1999) function is utilized to treat the problem of sampling errors in the ensemble covariance (Fig. 3.4); observations are only allowed to update the model state variable if they fall within a certain cutoff radius in both the horizontal and vertical. Sampling errors tend to be largest when the actual correlation is small, such as at large distances (Sobash and Stensrud 2013). A unique cutoff radius, which is vertically stretched, is set for each observation type (conventional or radar) in both the horizontal and vertical following Johnson et al. (2015). For the conventional observations assimilated on the outer domain, the horizontal localization cutoff radius is set to 700 km and increases by a factor of 1.5 at the model top. The vertical localization is set to 0.275 scale height units (natural log of pressure), increasing to 0.55 at the model top for temperature and moisture, and 0.55 increasing to 1.1 for wind. On the inner-domain, constant correlation length scales of 20 km in the horizontal and 1.1 scale height units are used for all radar observations (radial velocity and reflectivity) in the vertical. For conventional observations assimilated on the inner domain, only the constant correlation length scale in the horizontal is increased to 200 km.

To treat errors associated with the misrepresentation of model errors, such as those associated with physical parameterizations, both a constant (multiplicative; Whitaker and Hamill 2012), as well as a relaxation to prior spread (RTPS; Whitaker and Hamill 2012) inflation technique are applied to the ensemble spread. A constant inflation of 15% is applied every 3 hour cycle to the background spread on the outer domain; an equivalent $\sim$0.4% is applied every 5 min cycle on the inner domain. The inflation parameter smoothly tapers to $\sim$3% at the 50 hPa model top to avoid excessive spread near the model top, similar to Zhu et al. (2013). The RTPS (also called adaptive inflation) technique inflates the posterior ensemble spread to a certain percentage (95% in our case) of the prior ensemble spread to account for excessive spread reduction during the assimilation process. Lastly,

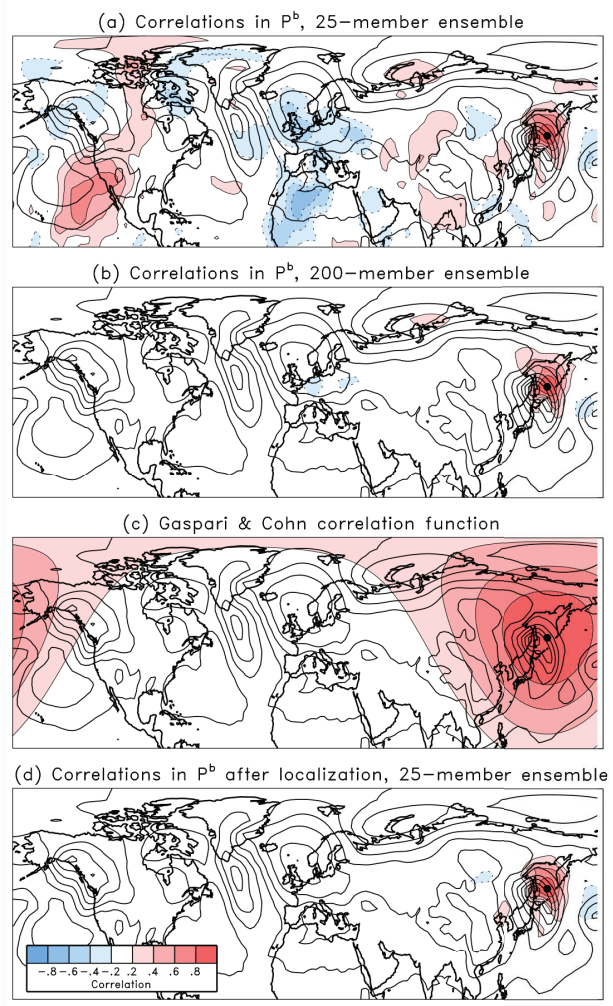


Figure 3.4: Illustration of covariance localization from Hamill (2006). (a) Correlations of sea-level pressure directly estimated from a 25 member ensemble with pressure at a point in the western Pacific (fill). Solid lines denote ensemble mean background sea-level pressure contoured every 8 hPa. (b) As in (a) but using a 200-member ensemble. (c) Covariance localization correlation function. (d) Correlation estimate from 25-member ensemble after application of covariance localization. Note how even with 175 less ensemble members, (d) is very similar to (b) due to the use of the covariance localization function.

following Dowell and Wicker (2009) and Yussouf et al. (2013), additional noise is added to the inner domain fields of temperature, dew point temperature, and the horizontal winds as a final step before integrating WRF forward. Errors based on standard deviations of 0.50 K and 0.50 m s^{-1} are added to each field where the observed reflectivity is greater than 25 dBZ. Additive noise helps to maintain ensemble spread during DA and quickly introduce observed storms into the analysis. Note that the exact values of localization and inflation parameters are often case- and application-dependent. These values were chosen following Johnson et al. (2015), though additional work determining optimal values for nocturnal convection is likely needed.

3.3 Experimental design

The simulations described in this study are "multi-scale" in that they involve determining the impact of assimilating two different observations types that sample unique scales and features. For this purpose, three experiments are designed (as summarized in Table 3.2). Conventional data are assimilated for all experiments on the outer domain at 3 hour intervals beginning at 0000 UTC on 24 June until 0000 UTC on 25 June when the inner domain is initialized. For the inner domain, the different observation types are assimilated at different cycling intervals. Peña and Kalnay (2004) explain that cycling frequency should be consistent with the mode of error growth consistent with that observation type. In the convDA experiment, only conventional assimilation is performed on the inner domain for 3 cycles of 30 minute intervals (to 0130 UTC on 25 June) with the goal of improving the mesoscale and synoptic environments to be more supportive of new developing convection. This can be done by improving upper-level features as well as thermodynamic support and cold pool structures. In the radarDA experiment, only radar data is assimilated on the inner domain for 18 cycles of 5 minute intervals (also

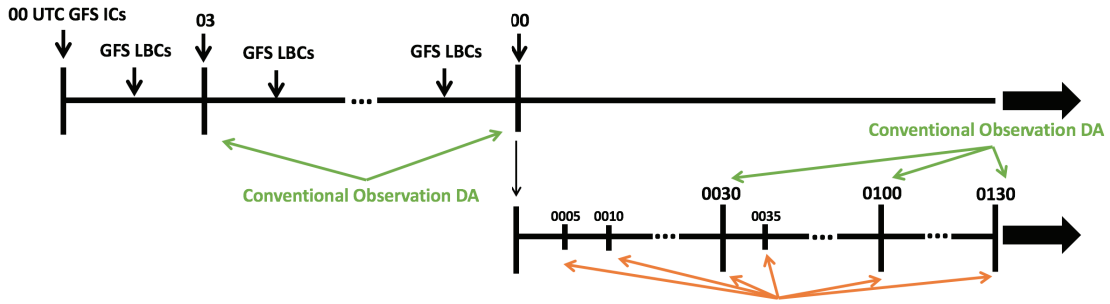


Figure 3.5: Flowchart for the allDA experiment. The green arrows indicate analysis times during which conventional observations are assimilated, while the orange lines indicate analysis times during which radar observations are assimilated. The top line is for the outer, 12 km domain while the bottom line is for the inner, 4 km domain.

to 0130 UTC on 25 June) with the goal of improving the structure of the previous convection and any outflow boundaries in southern Kansas. Lastly, the allDA experiment assimilates both conventional and radar observations on the inner domain with the same cycling patterns described above. Since all state variables are able to be updated by all observations in the EnKF through cross-variable correlations, this experiment allows conventional observations to update radar-related variables (such as hydrometeor contents) and vice-versa. A flowchart for the allDA experiment is shown in (Fig. 3.5).

Experiment	**Assimilation Cycles**
convDA	Conventional observations assimilated for 3 cycles (one every 30 min)
radarDA	Radar observations assimilated for 18 cycles (one every 5 min)
allDA	Both conventional (3 cycles; one every 30 min) and radar (18 cycles; one every 5 min) observations assimilated

Table 3.2: Summary of observation assimilation experiments on the inner domain.

Chapter 4

Observation impact analysis

4.1 Data assimilation cycling results

We first examine the results of the data assimilation cycling experiments (convDA, radarDA, and allDA) to determine what impact each observation type had on the final EnKF analyses ending at 0130 UTC on 25 June. Since the true state of the atmosphere is not known and instead approximated by the DA process, the quality of the update cycles is first evaluated based on the guesses' (background or analysis) fit to independent observations. Two quantities, including the root mean square innovation (RMSI) and total ensemble spread (TES), are calculated within the observation space. For a given innovation of:

$$\boldsymbol{d} = \boldsymbol{y}^o - \overline{\boldsymbol{H}(\boldsymbol{x}^{\boldsymbol{f}})} \tag{4.1}$$

the RMSI is calculated as:

$$RMSI = \sqrt{\langle \boldsymbol{d}^2 \rangle} \tag{4.2}$$

in which $\boldsymbol{y}^o$ is the observation vector, and $\boldsymbol{H}(\boldsymbol{x}^{\boldsymbol{f}})$ is the forecast guess vector (either the background or analysis) in observation space. Brackets indicate an average over all observations, while an overbar represents an ensemble mean. TES

(Dowell and Wicker 2009) is an estimate of the ensemble spread combined with the observation error, σ_o^2:

$$TES = \sqrt{\sigma_o^2 + \langle \frac{1}{N-1} \sum_{n=1}^{N} [\boldsymbol{H}(\boldsymbol{x}_n^f) - \overline{\boldsymbol{H}(\boldsymbol{x}^f)}]^2 \rangle} \tag{4.3}$$

A perfectly consistent ensemble, in which the total ensemble spread provides a perfect estimate of the actual error of the ensemble, would produce a plot of RMSI that overlaps with the TES. Three common verification metrics are calculated in observation space based on the first guess and analysis fields (Figs. 4.1, 4.2). The first is the "sawtooth" plot which compares an alternating time-series of background and analysis RMSI to the TES (Wheatley et al. 2014); the second is a profile of RMSI and TES; and lastly a profile of the background and analysis bias given simply as $\langle \boldsymbol{d} \rangle$.

The outer domain, in addition to providing the initial conditions for the inner-domain, storm-scale assimilation, also interacts with features on the inner domain through the use of two-way nesting. Thus we first evaluate the DA cycles during the 24 h of conventional assimilation on the outer domain in Fig. 4.1. As is expected, each assimilation update cycle produces a reduction in RMSI: the improvements are largest for temperature and wind, and smallest for the water vapor mixing ratio. The ensemble spread provides a good estimate of the model error for both temperature and wind speed, however mixing ratio is overdispersive throughout all of the lower troposphere (where more water vapor is located) and during all DA cycles (Fig. 4.1d,e). There is also a slight cold bias at the surface that is oddly pulled to be even slightly colder (to $\sim$ -1 K) by the analysis update (Fig. 4.1c). And while the mixing ratio is nearly unbiased, the same miscorrection occurs for the mesoscale analysis of wind speed (Fig. 4.1i). However these errors are minor and the final domain-averaged RMSIs of 1.4 K, 1.3 g kg^{-1}, and 3.1 m s^{-1} are reasonable, thus we conclude that the mesoscale analysis provides a good initial background for the storm-scale domain. Since the inner domain experiments are each initialized

from the same outer domain analysis, the above results do not differ between the three experiments.

4.1.1 Inner domain conventional observation verification

To demonstrate the large improvement in the analyzed storm-scale environment via the addition of conventional observations, the sawtooth plots for the inner domain variables of temperature, water vapor mixing ratio, and wind speed are presented in Fig. 4.2. Note that these objective statistics are calculated over the entire inner domain, while the 2D plots over the convective area of interest (Figs. 4.9 onward) are zoomed in to include only Kansas. Profiles of bias and RMSI/TES are not included due to the small number of observations in each vertical bin for only three cycles. Omitting these three cycles of conventional DA, the temperature final RMSI almost doubles that of the experiments with the data included (3.25 vs. 1.8 K for the final cycle). The differences between other variables are less extreme, but the addition of conventional observations still provides a positive benefit. Adding in radar data, in addition to the conventional data (allDA) actually provides a small degradation in the error statistics for temperature (for which TES is also lower in allDA than convDA) and mixing ratio. This is possibly due to allDA overly suppressing echoes that in turn weaken the size and magnitude of true cold pools across the domain (Figs. 4.4a, 4.14).

Since most observations between 00 and 12 UTC in the conventional dataset are surface observations, the majority of the positive impact from conventional observations is found closer to the ground. The near-surface temperature biases at observation locations for the final EnKF update cycle (Fig. 4.3) reveal that the cold bias present in the outer domain remains throughout most of the inner domain. This error appears to be largest in the eastern half of the domain near eastern Kansas with temperature biases approaching -5 K near Kansas City, MO. This cold

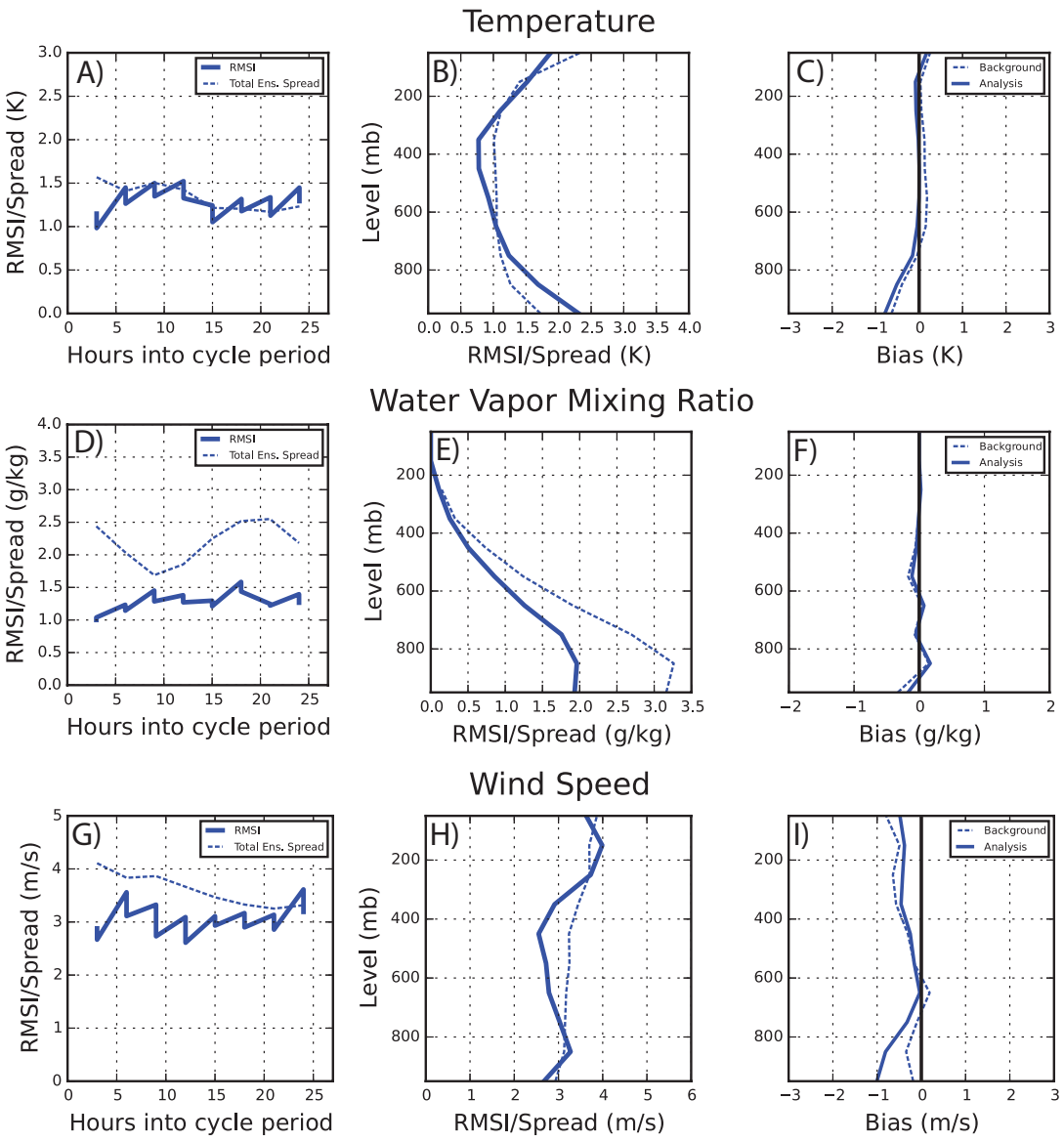


Figure 4.1: Verification statistics from the outer domain variables of temperature (K; a-c), water vapor mixing ratio (g kg^{-1}; d-f), and wind speed (m s^{-1}; g-i) including: (a,d,g) alternating time series of background and analysis RMSI (sawtooth; solid line) and TES (dotted line); (b,e,h) profiles of background RMSI (solid line) and TES (dotted line); and (c,f,i) background (dashed line) and analysis (solid line) bias.

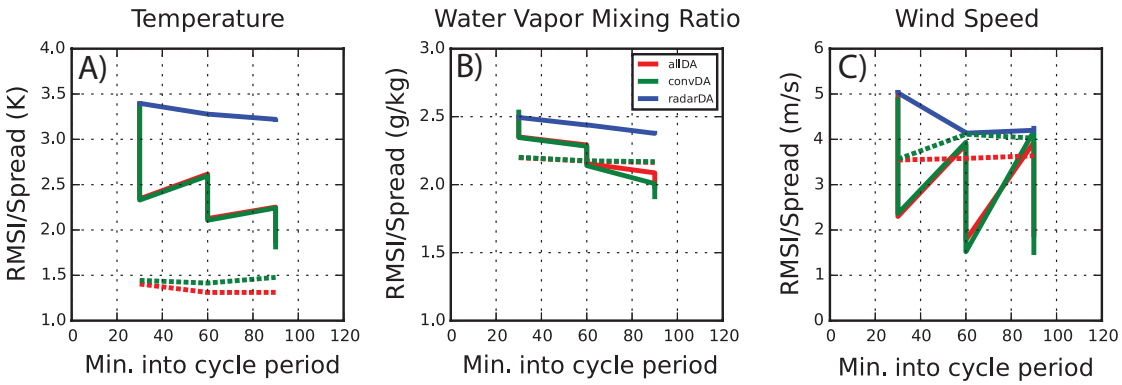


Figure 4.2: As in Fig. 4.1(a,g,d) but for the inner domain variables of temperature (K), water vapor mixing ratio (g kg^{-1}), and wind speed (m s^{-1}) for convDA (green); radarDA (blue); and allDA (red).

error is drastically improved by assimilating conventional observations, though the problem still exists (Fig. 4.3b). Cold biases across the state of Kansas are warmed to $\sim$ -1 to -2 K. However, the cold pool produced by previous convection in southern Kansas is too warm in the final analysis; a warm bias of $\sim$ 2 - 3 K exists that is not improved by conventional observations. Improving moisture biases is an another important advantage of conventional data assimilation specifically for CI purposes, as even slight thermodynamic differences in a mesoscale environment can produce precipitation at completely different times and locations (Martin and Xue 2006). Similar improvements can be seen in the water vapor field near the surface: dry biases in northeastern and southwestern Kansas, as well as southern Nebraska are moistened with the addition of conventional data (Fig. 4.3c,d).

Though we have no rawinsonde observations at the end of the cycling period to verify against, analysis soundings for the three experiments show differences in both the lower and mid-tropospheric environments across Kansas (Fig. 4.4a in southern Kansas and 4.4b in northern Kansas near the area of future CI). As will be discussed in the next sections, the convDA experiment produces overly

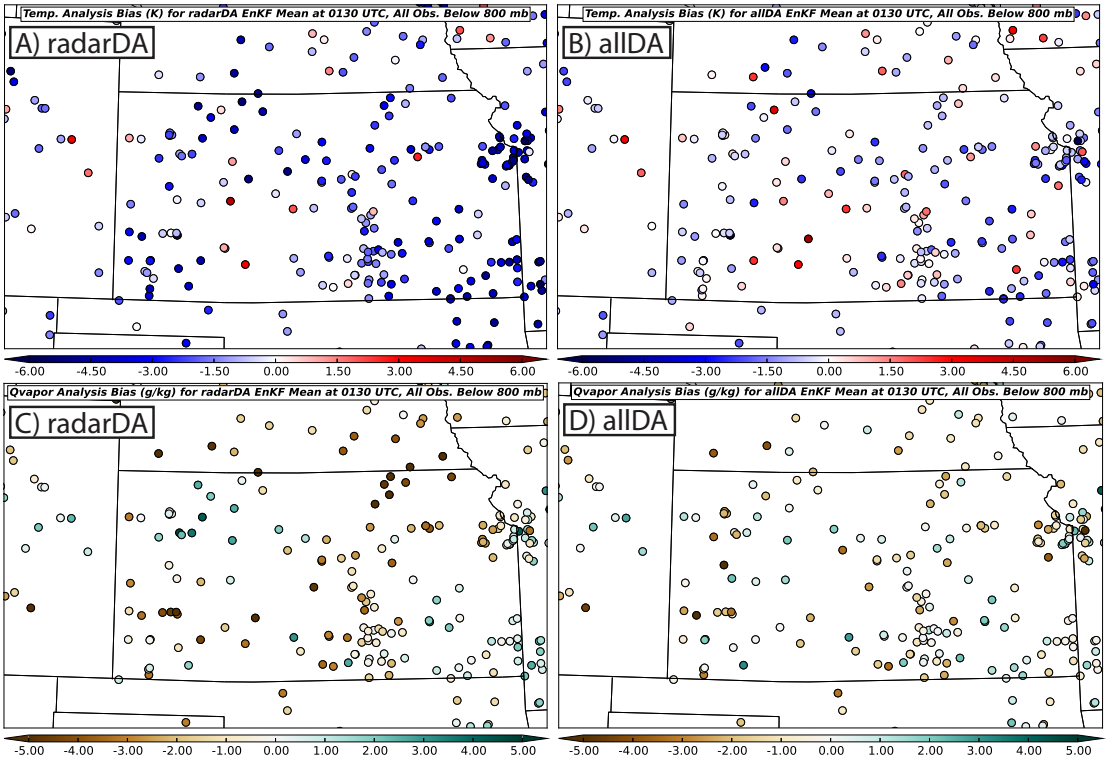


Figure 4.3: Final EnKF mean (a,b) temperature biases (K); and (c,d) water vapor mixing ratio biases (g kg^{-1}) at each observation location below 800 hPa for (a,c) radarDA; and (b,d) allDA.

strong storms in southern Kansas, leading to expansive cold pools throughout the area (as seen by the extreme low-level cooling in Fig. 4.4b). With the addition of radar data assimilation to suppress the spurious echoes and remove the diabatic heat source, the allDA and radarDA experiments produce cooler upper-level temperatures across northern and southern Kansas. Despite the low-level cooling and warmer upper-level temperatures, the experiments with conventional DA (allDA and convDA) produce steeper low-level lapse rates and enhanced low-level moisture, leading to stronger instability located at the surface in southern Kansas (Fig. 4.5).

Lastly, as the nocturnal LLJ is often an important mechanism in producing nocturnal convection, we examine the differences in the analyzed 850 hPa winds ($\sim$700 m AGL in central Kansas) produced by the three experiments (Fig. 4.6). Though the jet has yet to fully develop by 0130 UTC, all three experiments analyze similar low-level wind speeds, with maximum values reaching between 40-50 kts. The addition of surface wind observations in the conventional DA experiments (convDA, allDA) weakens surface winds in southwestern and northern Kansas and thus confines the maximum speeds to near the region of new CI. More localized convergence is produced at the termini of these wind maxima with conventional DA. With just radar DA, the jet is more widespread across the entire western half of Kansas (but east of the dryline) and strong convergence is only located near the interactions with the northern surface boundary and the dryline.

4.1.2 Inner domain radar observation verification

Radar reflectivity verification (Figs. 4.7a-c) is only performed on the inner domain in locations where precipitation (as defined by reflectivity $>$ 10 dBZ) is present in both the guess and the observation. Since the default value for no-precipitation is -35 dBZ in WRF, any location in which precipitation was observed

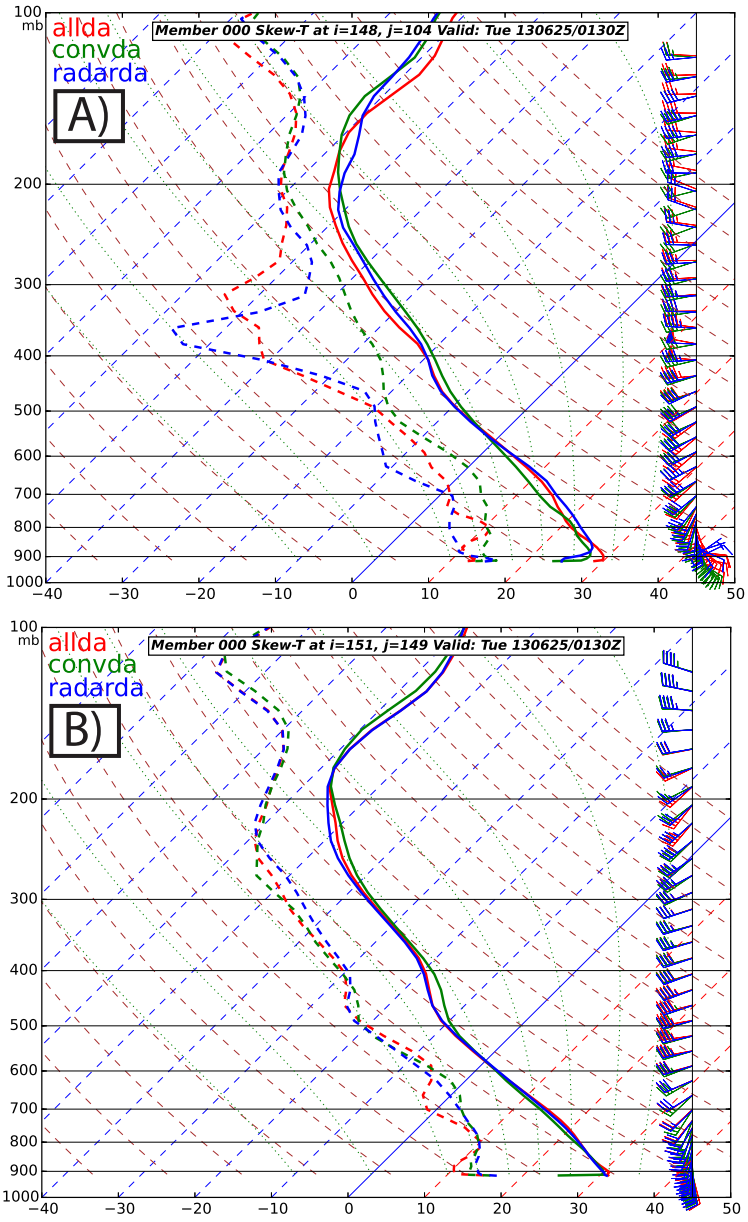


Figure 4.4: Final EnKF mean analysis (0130 UTC) soundings from (a) southern Kansas and (b) northwestern Kansas for: convDA (green); radarDA (blue); and allDA (red).

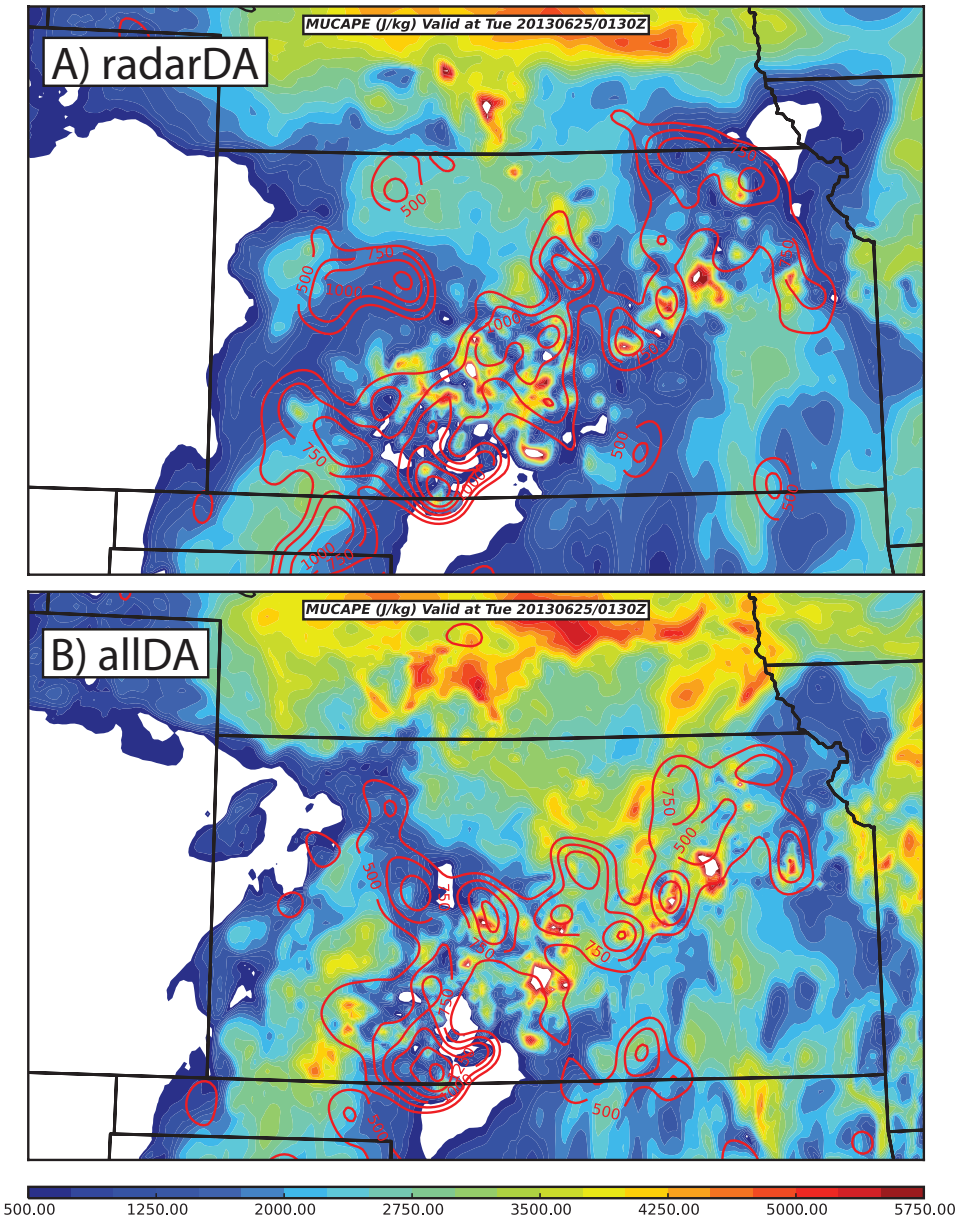


Figure 4.5: Final EnKF mean analysis (0130) of the most unstable convective available potential energy (MUCAPE; J kg^{-1}; filled) and the lifted parcel level (LPL; m; red contours) for (a) radarDA; and (b) allDA. The LPL indicates the height AGL that the most unstable parcel originates.

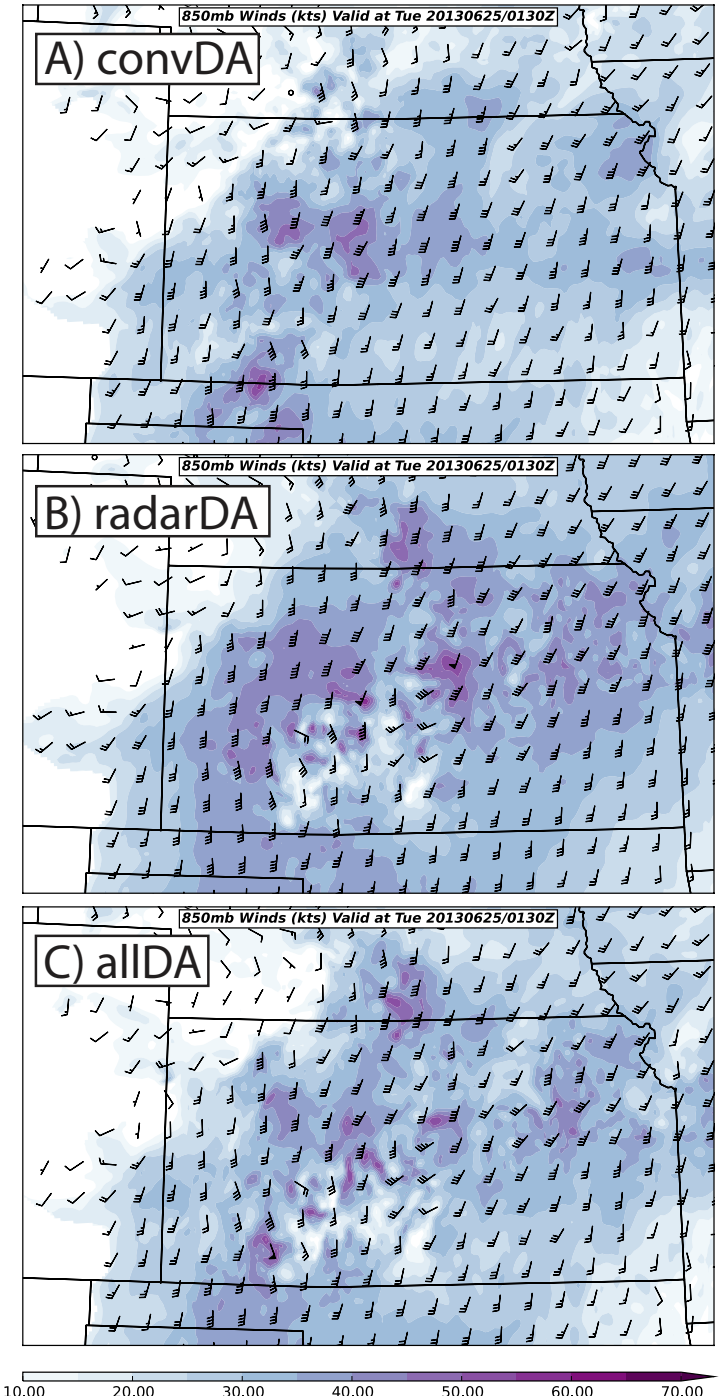


Figure 4.6: Final EnKF mean analysis (0130) of the 850 hPa wind speeds and barbs for (a) convDA; (b) radarDA; and (c) allDA.

but not located in the background/analysis would produce very large RMSIs and negative biases. Radar reflectivity RMSI and TES values are similar to previous studies (e.g. Dowell et al. 2011; Jones et al. 2015; Yussouf et al. 2015) and demonstrate that each cycle improves the overall fit of the analysis of the observed storms. Errors are highest near the surface, possibly due to a smaller number of observations at that level. Interestingly, with the addition of conventional DA (allDA) a higher RMSI is produced in the later cycles and closer to the surface. However the allDA ensemble does produce a larger TES to make up for this. Note that the increase in RMSI during the 16th cycle (at 0120 UTC) arises due to the KDDC radar being offline until that point and thus many more observations now being included in the assimilation and verification processes. There is little-to-no difference between the allDA and radarDA experiments in the errors and biases produced for radial wind (Figs. 4.7d-f); both experiments are stable and have reasonable RMSI and bias profiles.

Since the error metrics in Fig. 4.7 are only calculated at locations where precipitation is both observed and located in the guess (background or analysis), another method is needed to demonstrate that the radar data assimilation is providing a good fit to the observations. Fig. 4.8a shows the percentage of total precipitation observations in which precipitation was also located in the guess. Fig. 4.8b shows the opposite: the percentage of total clear-air observations in which clear-air was also located in the guess. Both of these metrics should increase with each update cycle as the model and observation state grow closer to each other, and a value of 100% would indicate complete agreement in terms of precipitation or clear-air locations (but not for the magnitude of those echoes). Though only 10% of observed precipitation locations have corresponding reflectivity echoes in the first background cycle, this value is increased to 70% by 40 minutes into the cycling

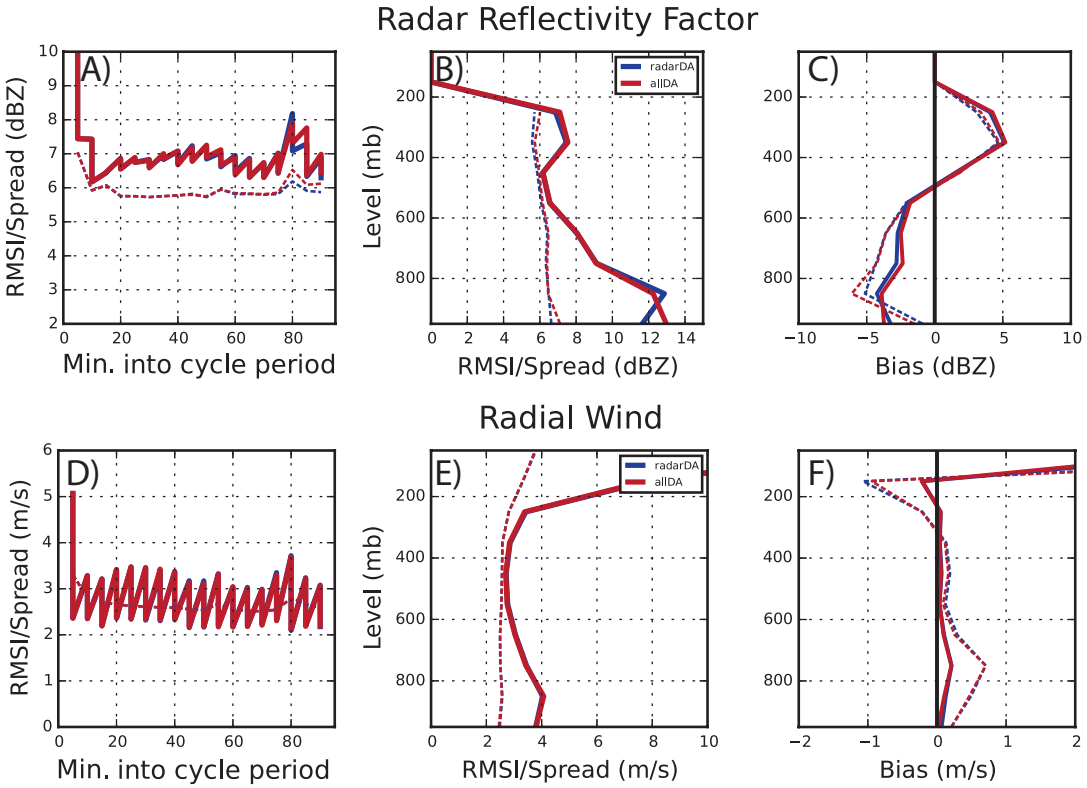


Figure 4.7: As in Fig. 4.2 but for the inner domain variables of radar reflectivity factor (dBZ; a-c) and radial wind (m s^{-1}; d-f). The blue line represents the radarDA experiment and the red line represents the allDA experiment. All statistics are only calculated at observation locations where both the guess and observation have reflectivity $>$ 10 dBZ.

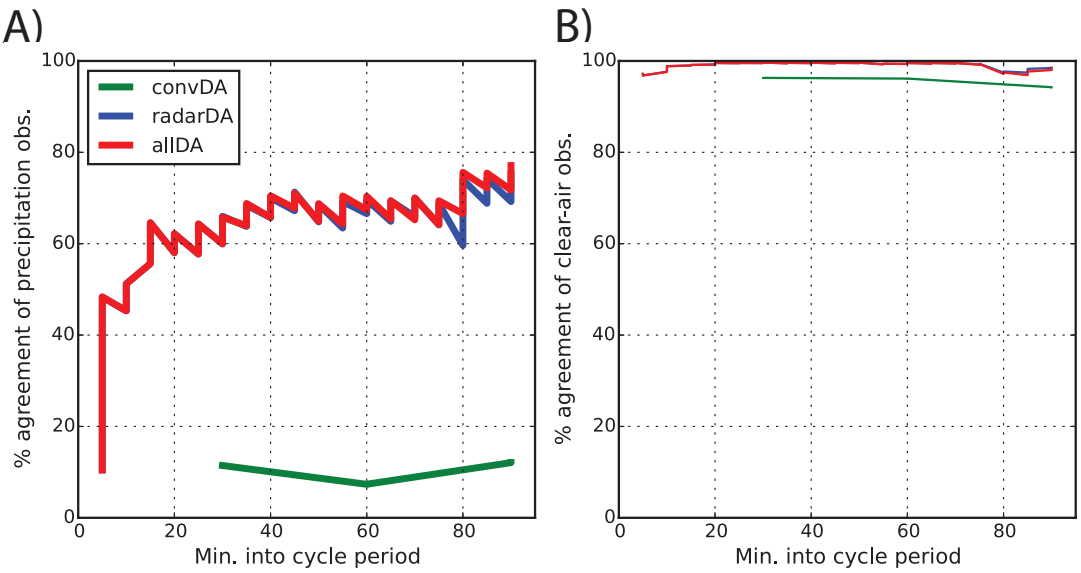


Figure 4.8: Alternating time series of background and analysis (a) percentage of precipitation observations where precipitation was also located in the guess; and (b) percentage of clear-air observations where clear-air was also located in the guess. The green lines indicate convDA; the blue lines indicate radarDA; and the red lines indicate allDA.

period (Fig. 4.8a), thus demonstrating that the reflectivity assimilation is properly adding correct precipitation locations into the model state. This is a large improvement to the experiment without any radar assimilation, in which only 15% of observation locations with precipitation are in agreement. Additionally, the radar assimilation is correctly working to remove spurious areas of precipitation by improving the agreement in clear-air locations between the model state and the observations (Fig. 4.8b). The small increase in spurious precipitation at 80 minutes into the cycling period is a result of the KDDC radar coming back online and thus a large number of new observations being added to the dataset. However, many of these spurious areas are removed within the last two cycles.

As discussed in section 3.2.2, if the observation is ever less than a noise value of 5 dBZ, it is reduced to the no-precipitation level in WRF of -35 dBZ. This has the impact of greatly suppressing the occurrence of any spurious echoes when assimilating radar observations. Without any radar data assimilation, many spurious storms form along the western border between Kansas and Nebraska that persist until the end of the cycling period (Fig. 4.9a). Although most members highlight this northern area of convection, as well as an additional area in southwestern Kansas, a lot of spread is present in the composite reflectivity field, with all members showing different shapes and locations of convective activity. By assimilating radar data (Fig. 4.9b), the spurious echoes in northern Kansas are totally removed in the final analyses. The core of the southern storm is well analyzed and there is strong ensemble agreement on its location. Overall the analysis looks very similar to the observations in Fig. 4.9d. More spread is present southwestern Kansas, potentially due to the KDDC radar only being online for 20 minutes at that point. The addition of conventional data (allDA; Fig. 4.9c and red line in Fig. 4.8) better suppresses spurious convection towards the end of the cycling period, as indicated by a smaller percentage than radarDA of non-precipitation observations in which precipitation is located in the guess. However, this addition might be slightly over-suppressing some observations compared to the radarDA experiments, as seen by the slight gap in Fig. 4.8b near the end of the cycling period.

4.2 Ensemble forecasts

4.2.1 Convection initiation forecast differences

The previous sections have demonstrated the thermodynamic and kinematic advantages gained in the storm-scale analysis from assimilating conventional observations. Additionally, radar DA provides a large improvement through the

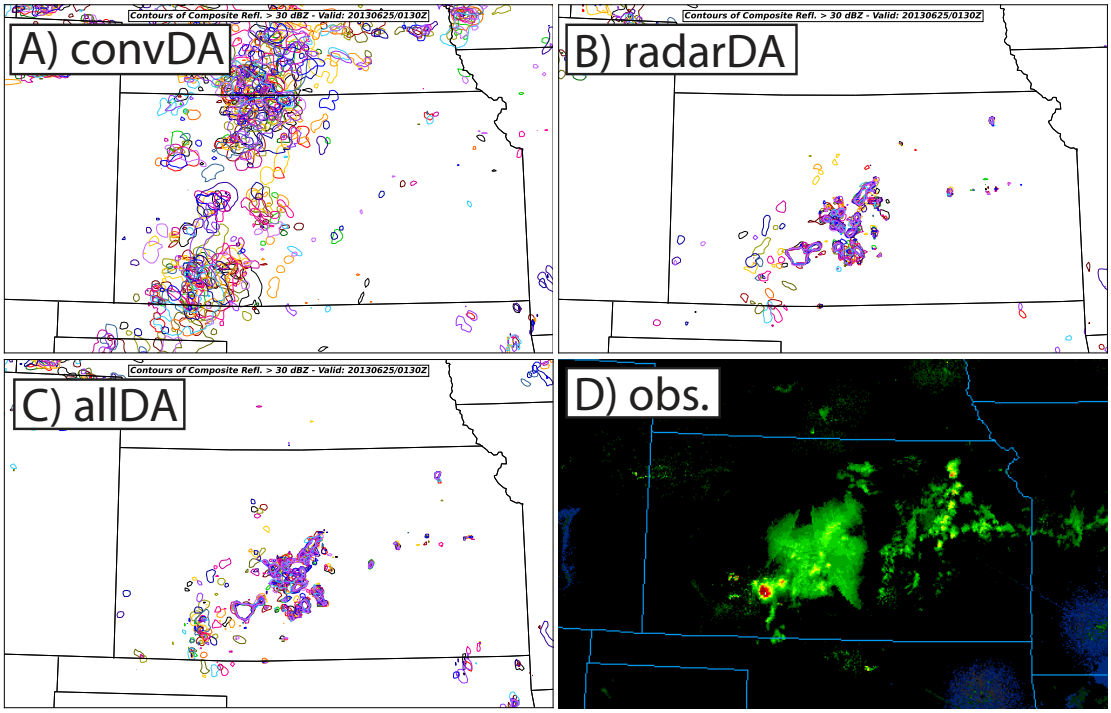


Figure 4.9: Spaghetti contours for each ensemble member of composite radar reflectivity factor greater than 30 dBZ for the (a) convDA; (b) radarDA; and (c) allDA EnKF analyses (at 0130 UTC). Each member plotted is a different color. Observed 1 km AGL reflectivity at the same time is given in (d).

suppression of spurious radar echoes and by better resolving pre-existing convection, especially in southern Kansas. We now determine the downstream impact these observations had by examining ensemble forecast differences between these two experiments. Spaghetti contours of reflectivity greater than 40 dBZ are presented in Figs. 4.11 – 4.13 and can be compared to observations at the same time in Fig. 4.10.

As mentioned in the previous section, convDA produces a largely spurious and very strong area of convection along the Kansas and Nebraska border. The southern Kansas convection produced is also overly strong, before and after the final EnKF analysis. These two regions of convection progress eastward throughout the free forecast, and almost no new storms develop in the first 1.5 h (Fig. 4.11a,b). The observed CI of interest that we are attempting to capture develops between 0230 – 0300 UTC, though these are not seen at that time in the convDA simulations. By 0400 UTC, a few members begin to show the first hints of echoes developing in northwestern Kansas (Fig. 4.11c), which form $\sim$ 1 h late and also possess a western location bias. However, they possess the same "pristine" quality and orientation as the observed storms, thus we consider this a successful forecast of the nocturnal CI. By 0500 UTC (Fig. 4.11d), 16 of the 20 ensemble members have captured the new CI and a few are actually producing the linear growth that the observed storms possess. Even though the convDA experiment produces a large, overly strong mass of convection just north of the area of interest, it is still able to successfully forecast the new CI.

Though the analysis for the experiments with radar data assimilated (radarDA and allDA) were able to better suppress the spurious echoes in southern Kansas during the DA period, spurious storms from southwestern to northeastern Kansas quickly redevelop in the free forecast periods of those simulations (0200 UTC; Figs. 4.12 and 4.13a,b). From this, we infer that, even though the radar data

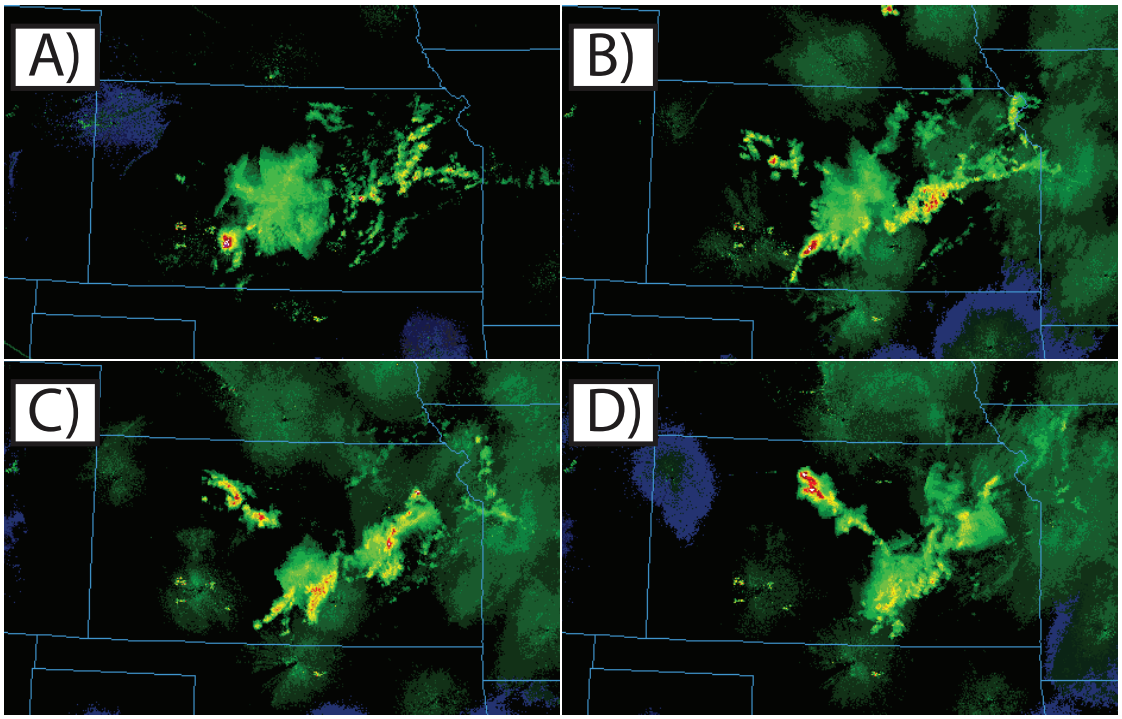


Figure 4.10: Observed 1-km AGL radar reflectivity factor from a) 0200; b) 0300; c) 0400; and d) 0500 UTC.

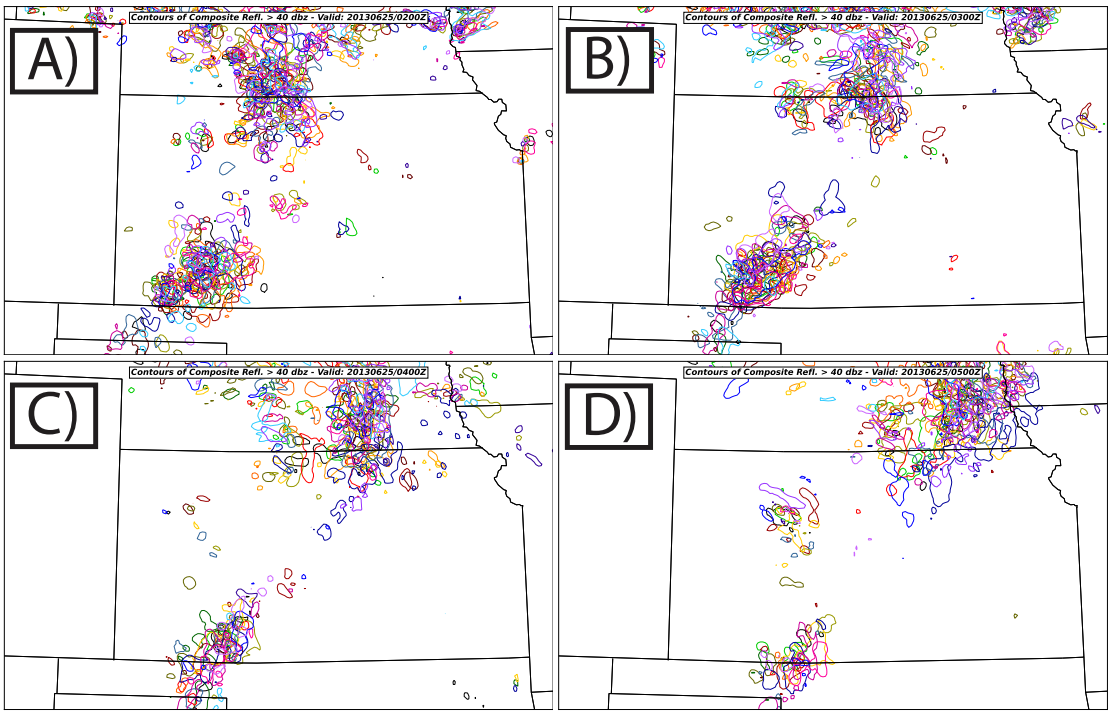


Figure 4.11: Spaghetti contours for each ensemble member of composite radar reflectivity factor greater than 40 dBZ for the convDA experiment, valid at a) 0200; b) 0300; c) 0400; and d) 0500 UTC.

are able to remove actual echoes from the area, the mesoscale thermodynamic and kinematic environments are strongly supportive of convective development. Storms also begin to initiate along the bulging dryline in northwestern Kansas within 30 min of the forecast period. Though these widespread spurious regions of convection quickly pop back up after the DA period, they fall apart by 0300 UTC ($\sim$ 1.5 h of free forecasts; Figs. 4.12 and 4.13b). Three areas of convection are emphasized by the radarDA and allDA experiments at this time: one in southern Kansas and eastern-central Kansas (both of these are observed), and another spurious region along the Kansas and Nebraska border (not observed, but much weaker than those produced by convDA). Through 0300 UTC, the radarDA and allDA experiments behave similarly, neither of which produce the new CI at the observed time. However by 0400 UTC (Figs. 4.12 and 4.13c), the allDA experiment begins to produce new echoes in a similar spot as the convDA experiment (once again an hour too late and with a westward bias). Additionally, the eastern area of convection begins to dissipate in radarDA at this time. This new development again becomes linear, similar to the observed storms, by 0500 UTC (Figs. 4.12 and 4.13d) in allDA, while radarDA continues to produce no new storms. Three ensemble members generate new convection around 0600 UTC in radarDA, but it is difficult to determine whether these are the same storms predicted as the other experiments due to the temporal lag. The improvements from convDA to allDA were small in regards to the new convective development. All but one ensemble member produced the new convection in allDA (three more than convDA). There is also more agreement (less spread) between the ensemble members as to the location of the new CI compared to convDA, producing an overall more confident forecast. However, some allDA members also develop the new convection about 15 minutes later than the corresponding members in convDA.

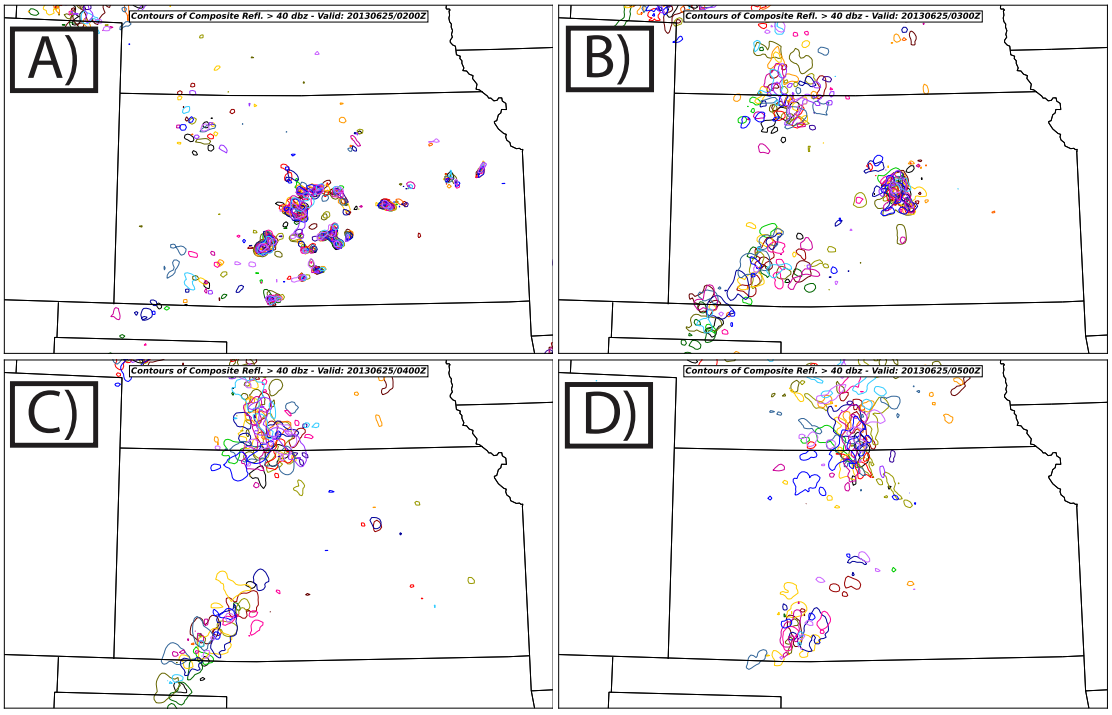


Figure 4.12: As in Fig. 4.11 but for the radarDA experiment.

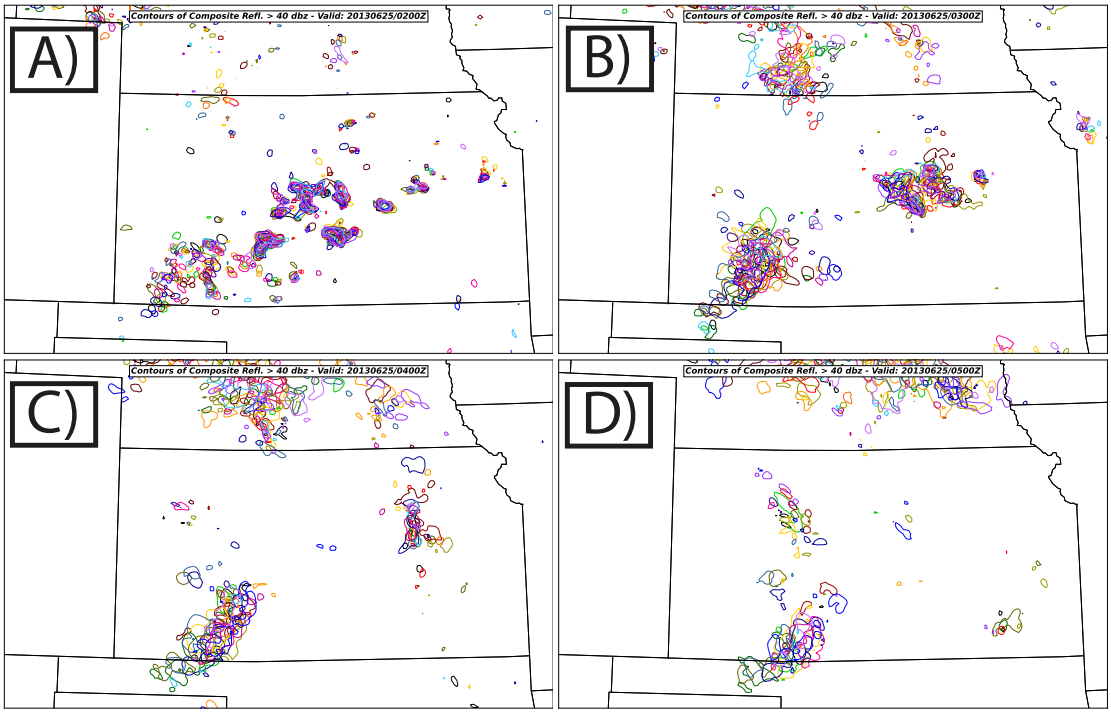


Figure 4.13: As in Fig. 4.11 but for the allDA experiment.

4.2.2 Thermodynamic and kinematic forecast differences

Both convDA and the allDA experiments produce the nocturnal CI of interest in northwestern Kansas, albeit with a temporal lag of $\sim$ 1 h and a westward bias of $\sim$ 100 km. While they both predict the new development, allDA produces an overall better forecast across the domain due to the continuing convection in eastern Kansas, as well as more confident forecast of the CI location. The addition of only three cycles of conventional assimilation appears to have been the key to capturing these new storms. The root cause of these new storms will be further studied in chapter 6; however important differences between other forecast components will be highlighted now. The plots to be shown in this section are 1.5 hour forecasts valid at 0330 UTC, 30 min before the new convection forms in the convDA and allDA experiments.

One large difference between the experiments with conventional DA and radarDA comes from the strength of the storm in southern Kansas. As mentioned in 4.1.1, the addition of conventional data during the assimilation process produces a more accurate thermodynamic environment, one that has steeper low-level lapse rates and is moister in southern Kansas (and thus more unstable). Due to this, the southern storm is enhanced in those experiments and in turn produces a much more obvious cold pool (Fig. 4.14). The cold pools produced by convDA and allDA are assumed to be more realistic, as a surface temperature of 72 °F was observed underneath the southern convection at 0300 UTC. This cold pool was found to be $\sim$ 750 m AGL deep (not shown) in the allDA simulations.

Near the surface at 800 hPa ($\sim$ 1200 m AGL), a band of positive vertical velocities associated with lifting ahead of the cold pool is seen moving outward from the convection in southwestern Kansas in convDA and allDA, but not radarDA (Fig. 4.15a,c; only radarDA and allDA shown). A sounding from northern Kansas (Fig. 4.16) reveals a nearly dry-adiabatic thermodynamic profile from $\sim$ 800 – 500

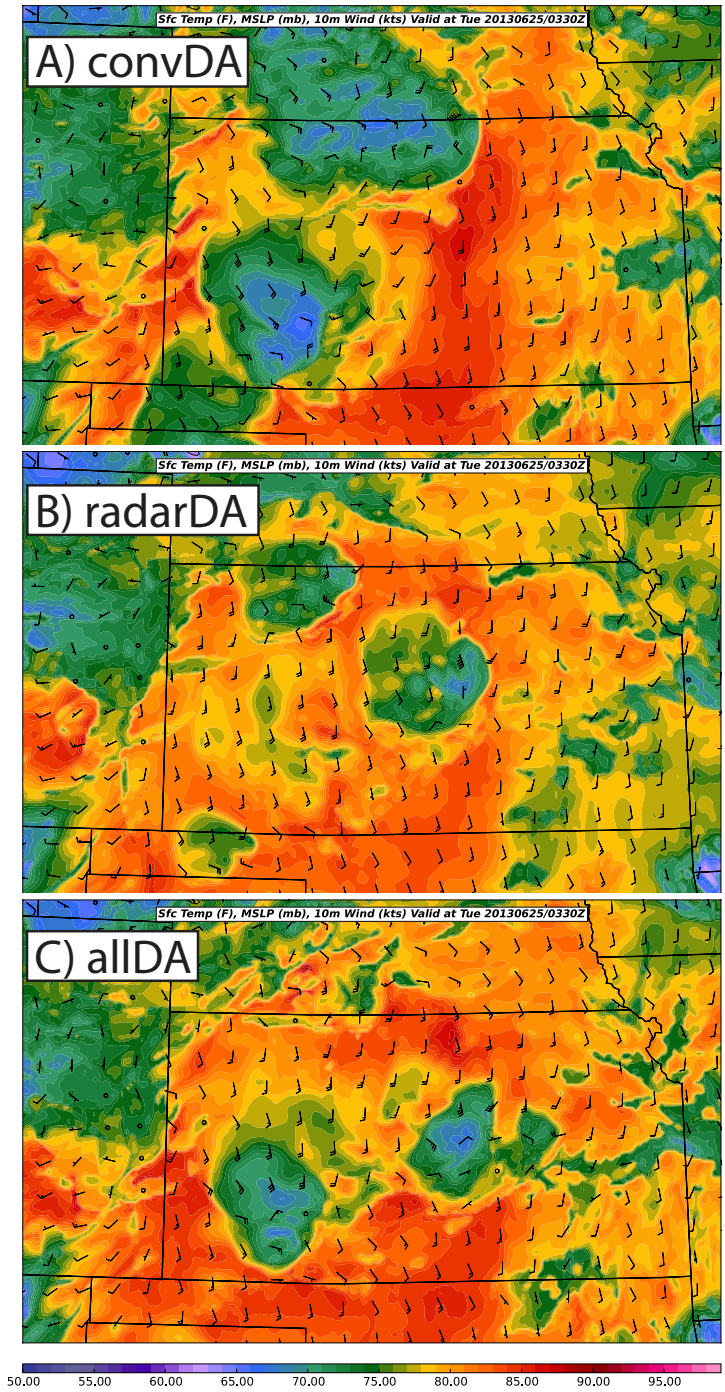


Figure 4.14: Two hour surface temperature (°F) ensemble mean forecasts valid at 0330 UTC from the: a) convDA; b) radarDA; and c) allDA experiments.

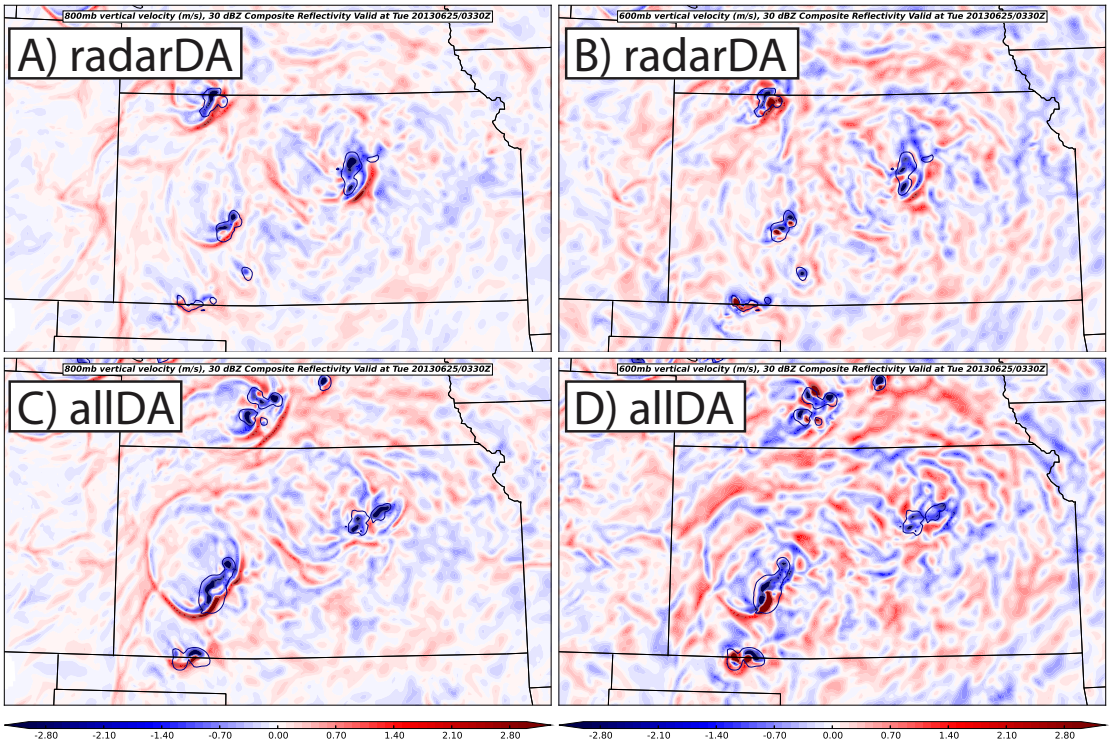


Figure 4.15: Two hour forecasts for member 3 valid at 0330 UTC of a,c) 800 hPa vertical velocity; and b,d) 600 hPa vertical velocity. (a,b) are from radarDA, while (c,d) are from allDA. Also overlaid on all plots are the contours of 30 dBZ composite reflectivity.

hPa in all three experiments. The cold pool that was produced in convDA and allDA thus promotes deep lifting all the way up to the mid-troposphere (Fig. 4.15d). For these figures, only member 3 (which was determined to be the most consistent with observations of reflectivity) from each experiment is shown, as the ensemble mean smooths out slight location differences. Deep lifting is seen with this band all the way up to 600 hPa in allDA, while no similar features are seen with just radar data assimilated. Interestingly, multiple bands of positive vertical velocity are seen in the allDA experiment at 600 hPa that do not appear at 800 hPa; these will be discussed in further detail in chapter 6.

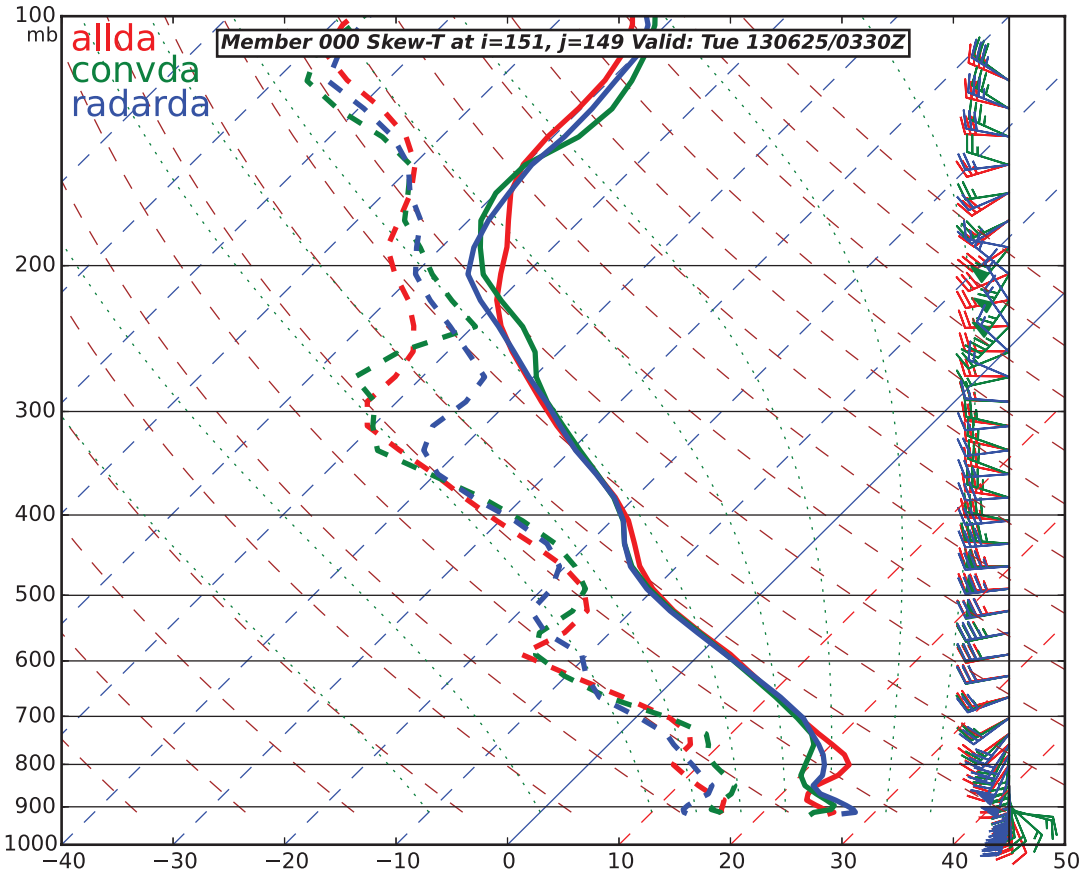


Figure 4.16: Two hour forecast ensemble mean soundings valid at 0330 UTC from near the area CI for: convDA (green); radarDA (blue); and allDA (red).

As mentioned in section 4.1.1, the radarDA experiment produces a LLJ with a more widespread wind maxima across western Kansas, compared to the localized maxima produced in allDA and convDA. This continued into the free forecast period (Fig. 4.17). At 0330 UTC, the localized convergence produced by convDA and allDA becomes much more apparent, especially in northwestern Kansas where the new CI soon develops. Compared to convDA, the allDA experiment produces a few more maxima across northern Kansas, and thus more localized areas of convergence are present. The low-level wind profiles lead to a different low-level thermodynamic profile between the three experiments (Fig. 4.16). Though convDA was found to produce warmer temperatures in the mid- and upper-levels due to diabatic heating effects from large amounts of precipitation, the upper-level profiles became more uniform between the three experiments throughout the forecast period. As we will show in chapter 6, the convection that formed in northwestern Kansas initialized above the 800 hPa warm nose and was thus this low-level profile difference was unlikely important for CI purposes.

4.3 Summary of observation impacts

The addition of each observation types provided a positive impact on both the analysis and the consecutive free forecasts. The convDA experiment without any radar data was able to capture the CI with similar timing and orientation to the allDA run. The addition of conventional data during the DA process greatly improved the storm-scale environment by reducing the errors in temperature, wind, and water vapor mixing ratio (mostly at the surface). The conventional data was also able to enhance the environment in southern Kansas (by a greater magnitude than the radar observations) for the pre-existing storms to strengthen during the earlier forecast, thus producing a stronger cold pool and deep tropospheric lift. Additionally, surface wind observations improved the LLJ analysis and forecast

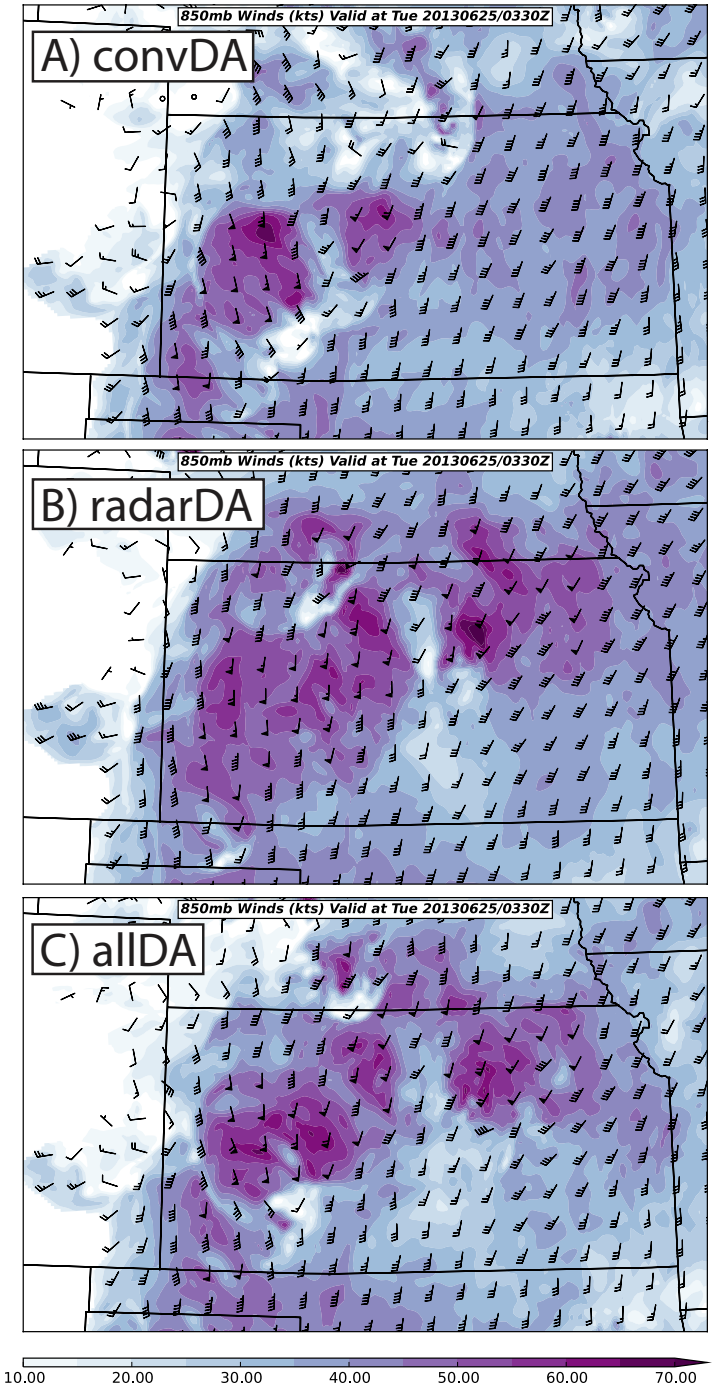


Figure 4.17: As in Fig. 4.6 but for the 2 hour ensemble mean forecasts of 850 hPa wind speeds (valid at 0330 UTC).

by producing more localized areas of convergence across western Kansas. We will soon show that these features improved by the conventional DA were extremely important for the CI process.

When comparing convDA to allDA, there were slight improvements in the location of the new development, as well as in the ensemble confidence of that location. However the timing of CI was later in this experiment as well. Perhaps the greatest impact provided by the addition of radar observations in the allDA experiment was the ability to better suppress strongly spurious echoes that were produced in convDA, and also to introduce storms into the model that would otherwise not be there. Though the radarDA experiment was not able to produce the new convection, the composite reflectivity analysis field looks very similar to the observations in Fig. 4.9d. Because of numerous spurious echoes in the early hours of a model simulation, operational meteorologists might not trust the downstream forecast of that model. Thus improving the initial fields of reflectivity in allDA provides a better end-product for the forecasters. Some spurious storms do quickly form again in the free forecast period, yet they are much weaker and less widespread than simulations without any radarDA at all. This reduction of spurious echoes also reduced the diabatic warming in the upper-levels of the troposphere which result in a more unstable environment for the new storms to develop within.

Chapter 5

Sensitivity to physical parameterizations

The previous chapter focused on the DA and ensemble forecast results from three different experiments to show the impact of different observation types on the forecast of nocturnal CI. We now shift our attention from forecast sensitivity to DA configuration, to sensitivities to different physical parameterization schemes. To study the impact of both the PBL and microphysics schemes on nocturnal CI for the 25 June event, the ensemble forecast simulations are run with five different schemes of each type. As we have previously determined that the allDA experiment produces the best analysis and forecast, we use the final EnKF analysis from that experiment to initialize these forecasts. Apart from differences in the PBL and microphysics schemes, all WRF configuration settings follow those discussed in chapter 2.

5.1 Planetary boundary layer parameterizations

Since the representation of turbulent mixing in NWP models is mostly a sub-grid process, PBL parameterization schemes are needed to control the transport and mixing of mass, moisture, and energy fluxes throughout the troposphere. The PBL scheme's responsibilities include the local mixing of sensible and latent heat fluxes (output from the land surface model) between the surface layer and the

PBL, local and nonlocal mixing (for some schemes) throughout the PBL, and also entrainment into the free atmosphere and vertical diffusion. Each PBL scheme requires a closure scheme to estimate the turbulent fluxes from mean quantities (Holt and Raman 1988): either a local closure scheme in which only adjacent vertical levels are considered, or a nonlocal scheme which consider a deeper layer. Thus the PBL scheme is often one of the main drivers of the low-level thermodynamic and kinematic structure of the environment; both of which are main factors in forecasting convection in a numerical simulation. For example, if the PBL is too warm or too dry, the LFC for surface-based convection might be unobtainable. Also, if the PBL scheme overmixes a jet maxima downwards, spurious convergence might be located near the ground. As nocturnal convection is often elevated, instability sources and updrafts tend to be disconnected from the surface. Thus unless the PBL scheme is performing poorly, such as when large errors in the solar irradiance inhibit the growth of ground-based nocturnal inversions (Zamora et al. 2003), the connection between elevated convection and the PBL scheme is less clear.

In this section, we examine nocturnal CI forecast sensitivities to five different PBL schemes following Coniglio et al. (2013). Three of the schemes examined are local schemes: MYNN following the control allDA experiment, quasi-normal scale elimination (QNSE; Sukoriansky et al. 2005), and Mellow-Yamada-Janjic (MYJ; Janjic 1994, 2002). The last two are nonlocal schemes: the asymmetric cloud model version 2 (ACM2; Pleim 2007), and Yonei University (YSU; Hong and Pan 1996; Noh et al. 2003; Hong and Kim 2008). Coniglio et al. (2013) compared rawinsonde observations upstream of deep convection to convection-allowing WRF forecasts. As the 1200 UTC morning radiosonde launch is the closest observation time to average nocturnal convection times, this is the closest previous studies have come to examining the different environments produced by PBL schemes specifically for elevated storms. They found that morning PBLs in all schemes (for both local

and nonlocal closure) are too cool and dry, despite having little bias in the PBL depth. The only outlier was the YSU scheme, which predicted significantly higher PBL heights during the early morning. This result, combined with the fact that the nonlocal mixing terms in ACM2 are shut off for nocturnal, stable conditions, implies that local mixing under more stable regimes produces more accurate nocturnal PBL depths. Past studies have supported this hypothesis (Shin and Hong 2011; Hu et al. 2010). The morning biases in temperature and moisture led to an under-prediction in mixed-layer CAPE and an over-prediction of mixed-layer CIN during the morning for all schemes, thus inhibiting early morning convection. In the evening, they found that local schemes produce PBLs that are often too shallow and too moist compared to the nonlocal schemes (though the local scheme MYNN was found to be nearly unbiased in PBL depth, moisture, and potential temperature). Hu et al. (2010) found that the vertical mixing at night is weaker in MYJ and ACM2 compared to YSU due to recent enhancements in its vertical mixing scheme, resulting in stronger LLJs, higher temperatures, and lower moisture. Few studies have specifically examined the role of PBL schemes in nocturnal CI. Recently, Johnson and Wang (2016) applied objective verification techniques to an operational forecast ensemble during the PECAN field experiment to find that, though the ensemble as a whole was nearly unbiased in forecast CI timing, certain physics schemes did demonstrate different results. MYNN was shown to perform the best, while QNSE members showed an early bias and ACM2/MYJ members showed a late bias. YSU members also showed a slight late bias but with more spread in the timing of CI.

In this study, we focus specifically on the PBL schemes' ability to forecast nocturnal CI and the important components that are possibly responsible for its occurrence. As PBL schemes are important drivers of thermodynamic and kinematic conditions within the boundary layer itself (lowest $\sim 1-2$ km of the troposphere),

we focus on low-level differences between the different forecast experiments. At the surface (Fig. 5.1), we notice that all PBL schemes produce cold pools with similar structure, and that there tends to be more similarity in their structure and magnitude within the local (MYNN, QNSE, MYJ; Fig. 5.1a-c) and nonlocal (ACM2, YSU; Fig. 5.1d,e) schemes. All PBL schemes appear to produce a cold pool that is too cold ($\sim$ 67°F), as the lowest temperature observed during this time was 72 °F. This is opposite of the results from the first cold pool present during the DA analysis, in which the area was analyzed as too warm. This region of southwestern Kansas is not observationally dense, so is possible that a lower temperature occurred but was not observed. The nonlocal schemes do not extend the cold pool as far to the north, similar to the observations (Fig. 2.7), though they produce surface temperatures slightly too warm (2 – 3 °F) in regions of western and northern Kansas.

Soundings from within (Fig. 5.2a) and ahead of (Fig. 5.2b) the cold pool from the southern Kansas convection are shown. Though there are no observed soundings around this time to verify against, we can note a few points. There once again is clustering in the vertical profile around the local and nonlocal schemes. The largest differences appear within the cold pool as the local schemes produce a weaker stable layer at 850 hPa with maximum temperatures of $\sim$ 19 – 20 °C, while the nonlocal schemes are $\sim$ 2 – 3 °C warmer. This reverses above 500 hPa, where the nonlocal schemes produce steeper lapse rates. Additionally, the nonlocal schemes are drier throughout most of the lower troposphere within the cold pool. Ahead of the cold pool where the new convection forms, there is very little difference between the schemes in the vertical profile (Fig. 5.2a,b). The inversion layer is now warmer in the local schemes by $\sim$ 1 °C. These differences have very little impact on the elevated CAPE in the region; no obvious differences appear (not shown).

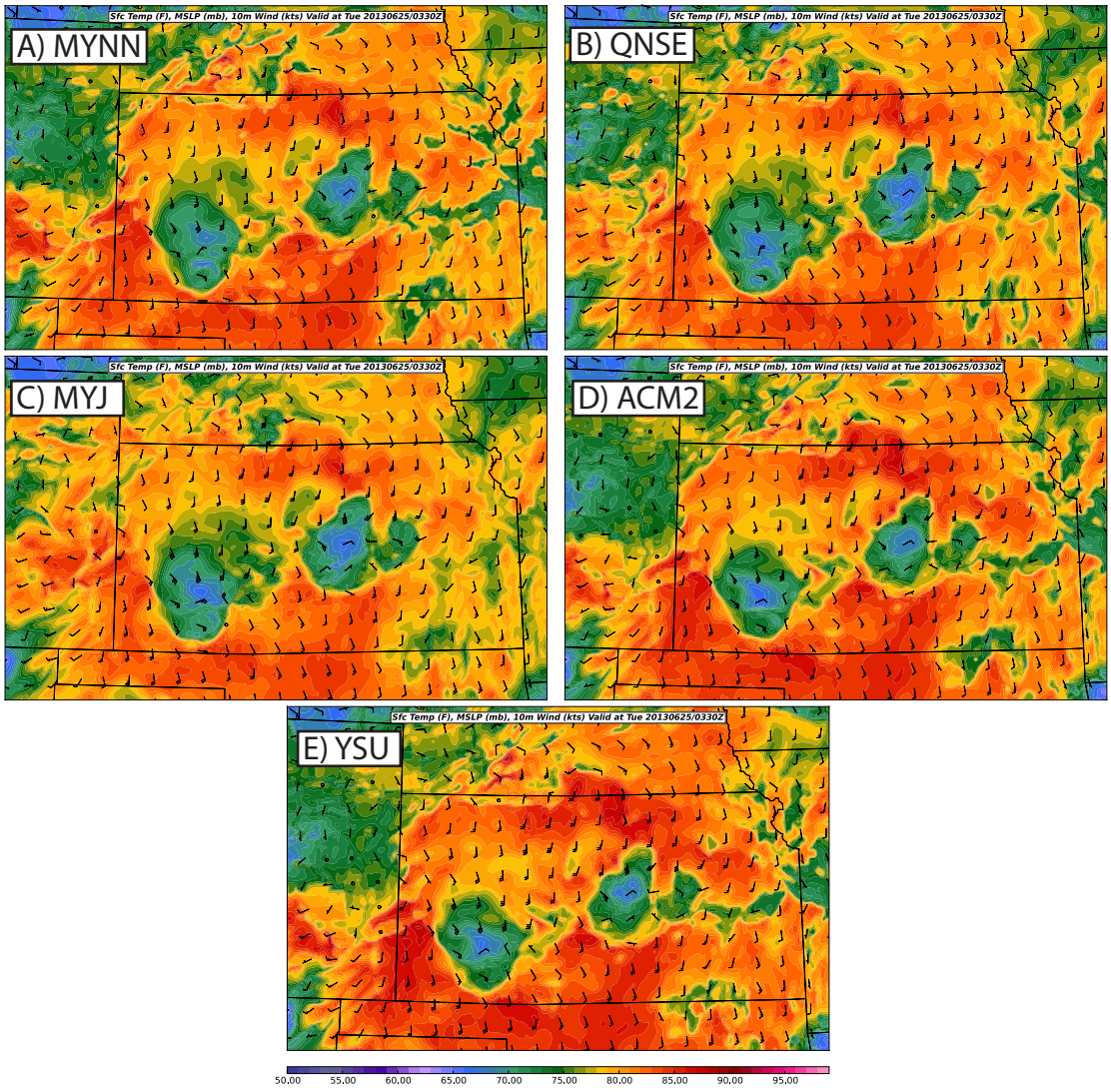


Figure 5.1: Ensemble mean surface temperature forecasts (°F) from 0330 UTC on 25 June for the (a) MYNN; (b) QNSE; (c) MYJ; (d) ACM2; and (e) YSU PBL sensitivity experiments.

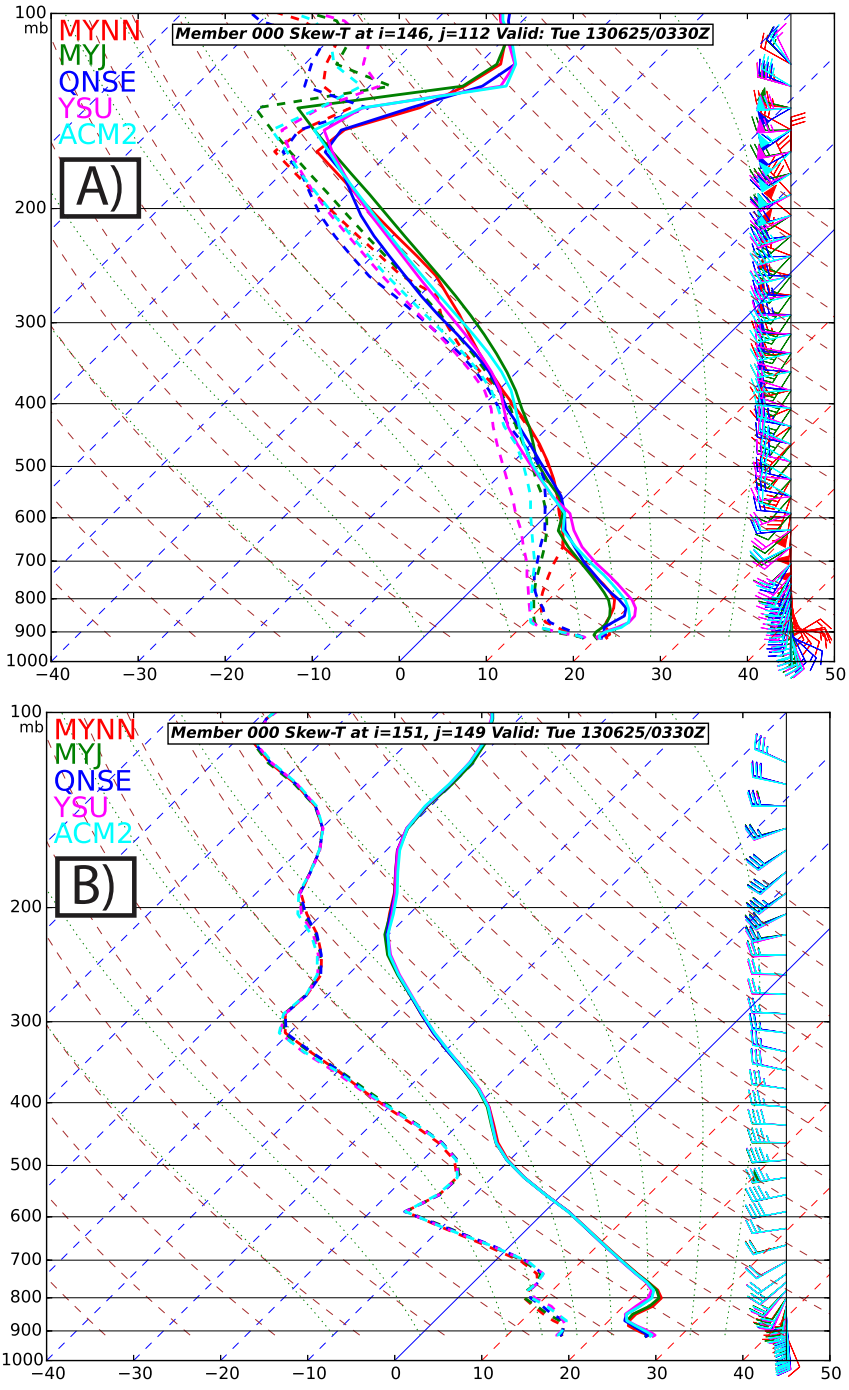


Figure 5.2: Ensemble mean soundings from (a) within the cold pool; and (b) ahead of the cold pool for each PBL scheme.

Since the PBL scheme determines the vertical mixing of horizontal momentum within the PBL, it is possible that different schemes could produce different LLJs. From the sounding within the cold pool (Fig. 5.2a), MYNN appears to produce a deeper LLJ. The local schemes overall produce stronger wind maxima at 850 hPa (and thus stronger convergence) in southwest Kansas (Fig. 5.3), consistent with findings from Hu et al. (2010), though the convergence areas are present in similar areas. As mentioned in the previous chapter, conventional observation assimilation produced strong lift ahead and behind the cold pools all the way up to 600 hPa; Fig. 5.4 demonstrates that there was little difference in these vertical velocity features between the various PBL schemes. Even though the cold pool was further south in the nonlocal schemes, the strongest lift along the outflow boundary occurred at similar locations and with similar magnitudes in all schemes.

The end results of these differences, which are comparatively small above the PBL and outside of the cold pool, are very similar forecasts of nocturnal CI for the 25 June case (Fig. 5.5). All schemes predict the convective development at the same time and location, and with similar structure and orientations. One member in MYJ doesn't produce the new convection that appears in other schemes, and ACM2 produces slightly less weak convection in southeastern Kansas. The convective members in each scheme grow linearly and look similar to other schemes at later lead times (not shown). The features responsible for triggering the CI of interest are likely disconnected from the PBL (to be discussed in the next chapter), leading to weaker sensitivities to the PBL scheme than one would expect from surface-based convection.

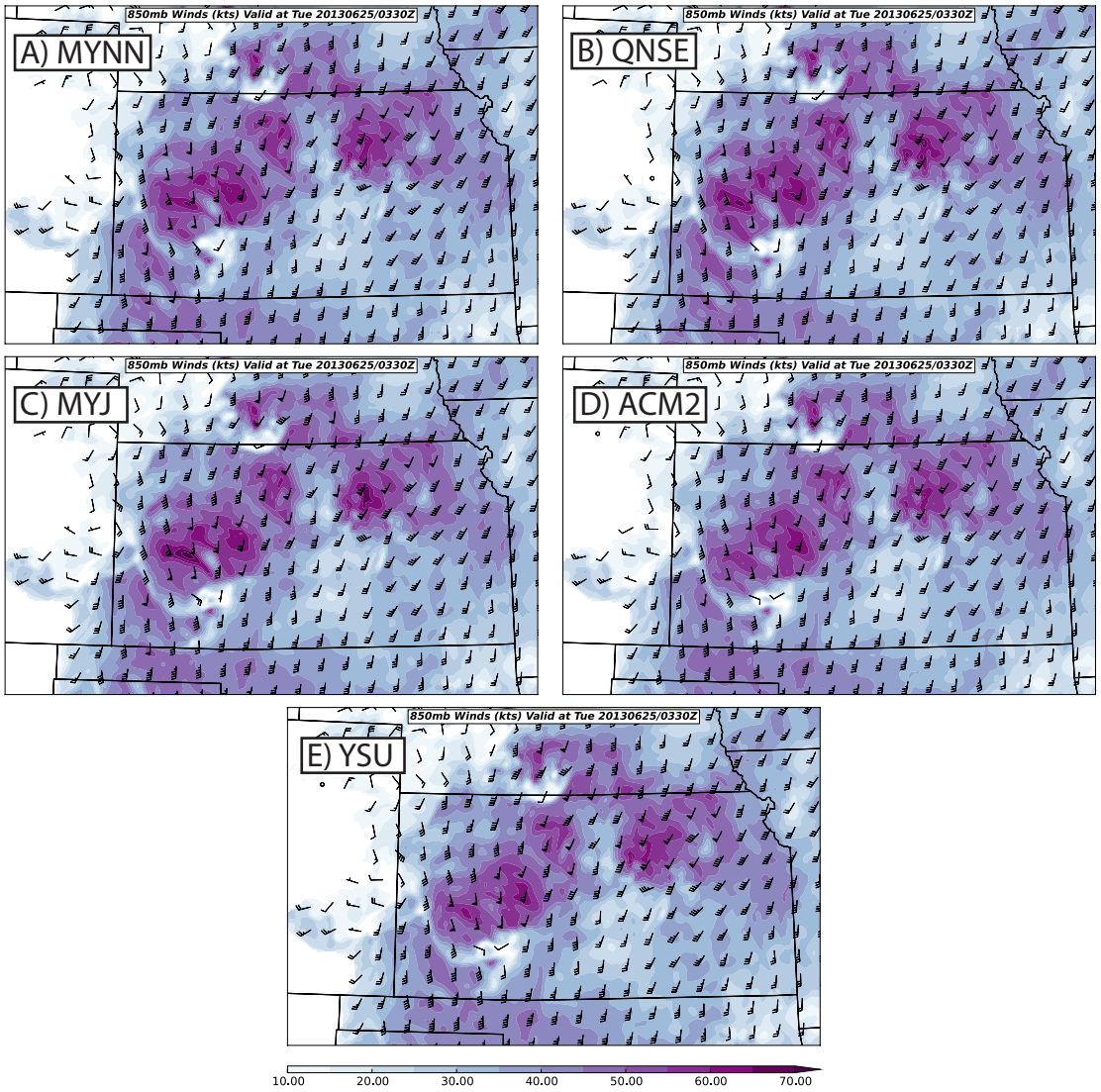


Figure 5.3: As in Fig. 5.1 but for 850 hPa wind speeds (kts).

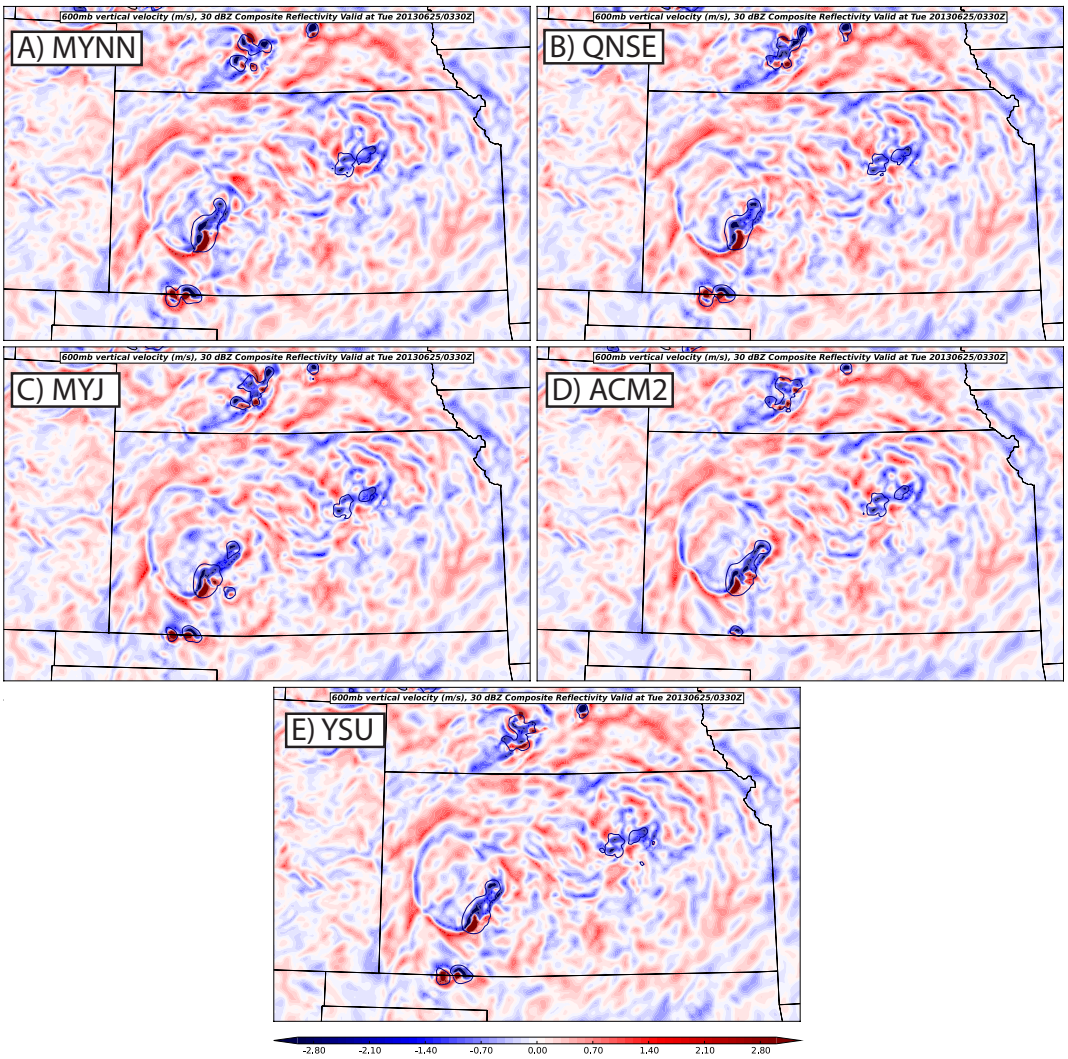


Figure 5.4: As in Fig. 5.1 but for 600 hPa vertical velocity (m s^{-1}) and only for member 3. Also plotted is the 30 dBZ composite reflectivity contour.

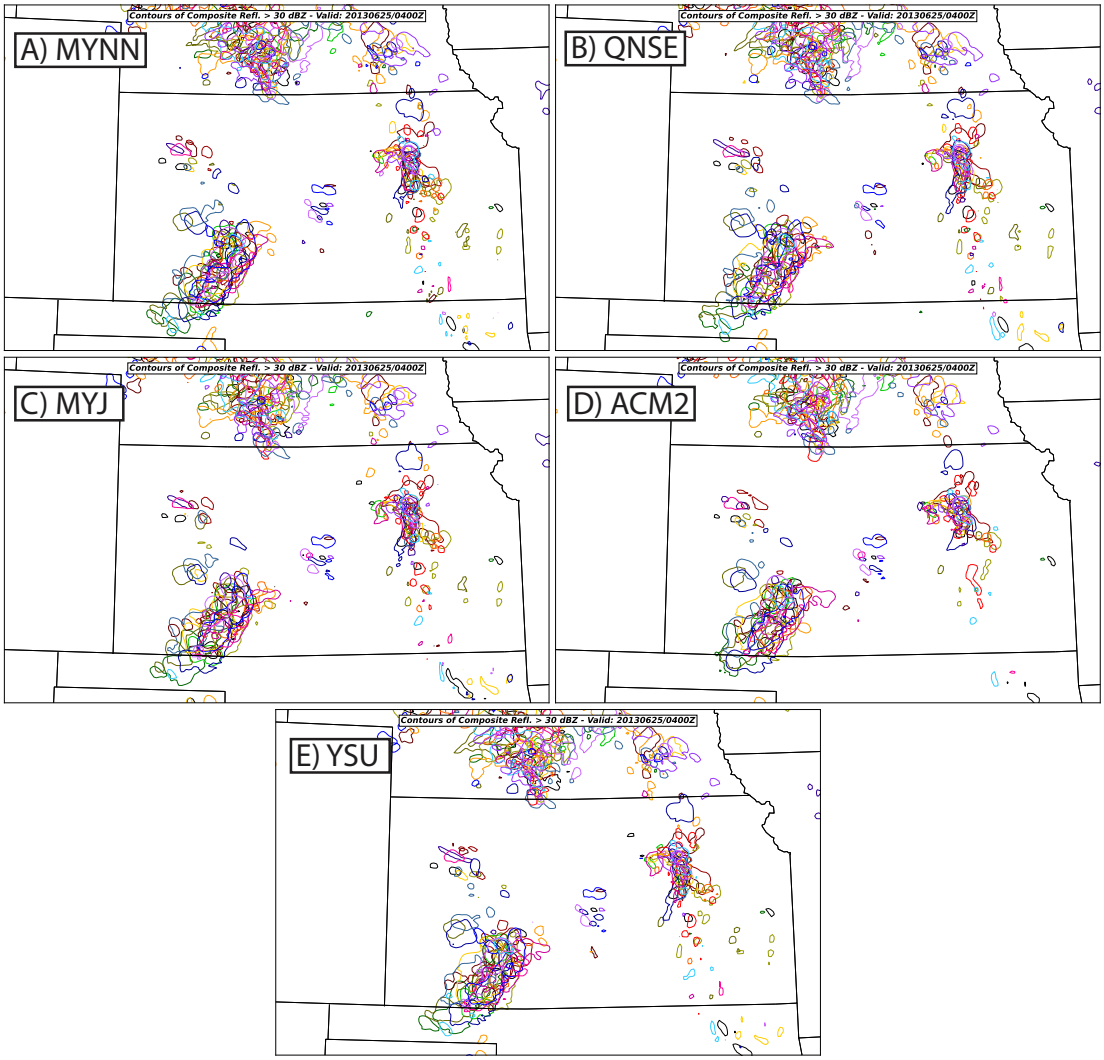


Figure 5.5: As in Fig. 5.1 but at 0400 UTC and for the spaghetti contours for each ensemble member of composite reflectivity greater than 30 dBZ.

5.2 Microphysical parameterizations

Microphysics schemes handle many processes within an NWP model but are mainly used to control the formation, growth, and fallout of cloud droplets and ice crystals. They also provide atmospheric heat and moisture tendencies, and surface rainfall quantities (Morrison and Milbrandt 2010). Microphysical processes driving these quantities include latent heating and cooling, condensation loading, sedimentation and evaporation, precipitation, coupling with surface processes, radiative transfer, and cloud-aerosol-precipitation interactions amongst others. Since these interactions occur at a scale much smaller than the common NWP grid size, microphysical parameterization schemes are needed. Nearly all schemes separate microphysical processes between liquid and ice phases (which are in turn separated into different ice species) and can be divided into two separate categories, similar to the PBL closure schemes. These include: bin schemes, in which the particle size distributions are discretized into individual bins; and bulk schemes, in which the size distribution is assumed to follow a functional form (such as a gamma distribution). The majority of all microphysics schemes used operationally and in WRF are bulk schemes due to their computational advantage. Additionally, all schemes can be divided into single- or multi-moment schemes. Though they are more computationally expensive, multi-moment schemes allow certain terms in the gamma distribution to vary and, in addition to predicting hydrometeor mixing ratios from the single-moment schemes, are also able to predict number concentration (2^{nd} moment), and reflectivity (3^{rd} moment).

The Lin scheme was subjectively chosen for the previous simulations and observation impact studies due to its ability to best produce convection similar to the observed storms. However, convective structure and precipitation distributions at the surface are known to be extremely sensitive to the choice of microphysics scheme (Otkin et al. 2006; Pieri et al. 2015). Thus we evaluate our nocturnal CI

forecasts using four other microphysics schemes, including the Thompson (semi-double-moment; Thompson et al. 2008), Morrison (double-moment; Morrison et al. 2005); WRF single-moment 6-class (WSM6; Hong and Lim 2006), and the WRF double-moment 6-class (WDM6; Lim and Hong 2010) microphysics schemes. These schemes, and which species they predict, are listed in Table 5.1. Many studies have examined the capability of various microphysics schemes in WRF to produce different cloud and convective features (e.g. Tao and Simpson 1989; Liu et al. 1997; Tao et al. 2003; Gilmore et al. 2004; Liu and Moncrieff 2007; Hong et al. 2009; Grasso et al. 2014; Johnson et al. 2015); however, few have examined these schemes specifically in terms of nocturnal convection.

Scheme	**Moment**	**Predicted Species**
Lin	Single-moment	Mixing ratios for cloud, rain, ice, snow, and graupel
Thompson	Partially double-moment	Mixing ratios for cloud, rain, ice, snow, and graupel; number concentrations of ice and rain
Morrison	Double-moment	Mixing ratios for cloud, rain, ice, snow, and graupel; number concentrations for rain, ice, snow, and graupel
WSM6	Single-moment	Mixing ratios for cloud, rain, ice, snow, and graupel
WDM6	Double-moment	Mixing ratios for cloud, rain, ice, snow, and graupel; number concentrations for rain and cloud; cloud condensation number

Table 5.1: Microphysics schemes studied in 5.2, as well as their moments and predicted species.

As the number concentrations predicted improve various microphysical processes, most results (e.g. Min et al. 2015) conclude that double-moment schemes perform better for diurnal convection cases. The double-moment schemes are also known to produce more accurate cold pools (Dawson et al. 2010). Li et al. (2015) examined the sensitivity of WRF microphysics schemes for precipitation and cold pools produced by shallow marine clouds. They found that, compared to Thompson, the Morrison scheme produces more robust cloud cover and liquid water path (LWP) due to a slower autoconversion and stronger accretion processes, and stronger cold pools due to differences in the terminal fall speeds producing higher evaporation rates. A common trend in microphysics studies indicates that different schemes can produce very different structures and magnitudes of cold pools due to differences in precipitation loading and evaporative cooling rates. Morrison et al. (2015) performed idealized WRF simulations and found that the differences in simulated cold pools, in turn, produce different amounts and structures of new convection along their outflow boundaries. Recently, Johnson and Wang (2016) examined the impact of microphysics schemes used during both the DA and forecast period for the purpose of nocturnal convection forecasts over a multitude of cases. They found that that the use of Thompson for DA produced worse results for forecasts of nocturnal precipitation (not specifically initiation) over WSM6 at shorter lead times, but that the opposite was true at longer lead times. When used during the forecast period, Thompson produced the most skillful precipitation forecast at all lead times. Additionally, an ensemble with multiple physics schemes (PBL, microphysics, and cumulus) using during the forecast period was subjectively shown to be more skillful at producing nocturnal CI.

Ensemble mean forecasts of composite reflectivity for the 25 June case are shown in Fig. 5.6. Thompson and Lin produce the most realistic convective structures for the southern Kansas storm compared to the observed storms, while precipitation regions in Morrison and the WRF schemes (WSM6 and WDM6) are much too expansive. In terms of highest reflectivity values, all schemes except WDM6 handle the storms well. WDM6 produces an overly strong convective core, which is also represented by the strongest cold pool at the surface (Fig. 5.6e). Thompson is known to better resolve stratiform precipitation regions, though it appears to be under-predicting most of the storms through central Kansas for this event.

The differences between simulated cold pools are larger for different microphysical schemes (Fig. 5.7) than they were for the PBL schemes. Lin and WDM6 simulate the coldest cold pools, which as in the previous section, are likely too cold compared to available observations in the region. Cold pools produced by the Thompson and WRF schemes are better forecast in terms of size, though Thompson appears to be slightly too warm. Morrison produces a very weak cold pool (Fig. 5.7c; lowest temperature of $\sim$ 77 °F), even though strong precipitation is present above. This is different from the Dawson et al. (2010) and Li et al. (2015) findings that show strong improvements in cold pool strength from the use of a double-moment scheme for diurnal convection. Similar differences are seen within the vertical thermodynamic profile of the cold pool (Fig. 5.8a). Morrison and Thompson are much warmer and dryer below 700 hPa than would be expected, thus it is possible that too much of the precipitation is evaporating before it can reach the surface and consequently producing nearly no cold pool. Johnson and Wang (2016) found that Thompson produced better results for a simulated nocturnal MCS by also producing a dry slot above the surface that inhibited the growth of a spurious MCS shown in other members. A similar dry layer is seen in our results,

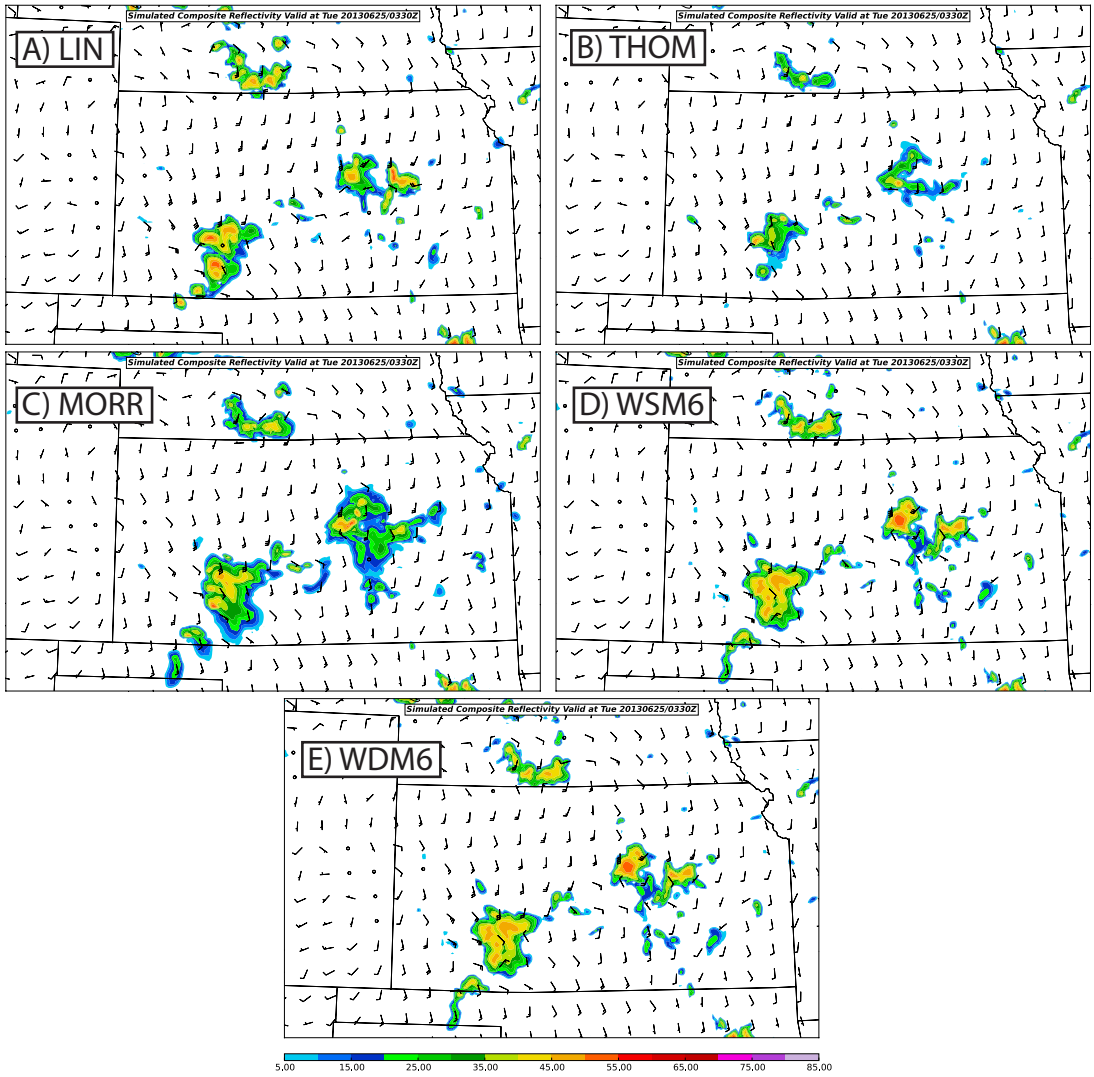


Figure 5.6: Ensemble mean forecasts of composite reflectivity (dBZ) valid at 0330 UTC for (a) Lin; (b) Thompson; (c) Morrison; (d) WSM6; and (e) WDM6 microphysics sensitivity experiments. Also plotted are surface wind barbs (kts).

though the impact of it appears to be negative. Thermodynamic differences are less significant ahead of the cold pool (Fig. 5.8b). The single-moment schemes are cooler below the inversion top, and temperatures from 500 hPa to the tropopause are slightly warmer in Lin, possibly due to strong diabatic effects. These differences once again yield almost no difference in the instability fields across Kansas.

Other than the large differences in the southern storm and its associated cold pool, almost no differences are noticeable in the other fields that have been discussed throughout this study. The LLJs produced by each scheme are similar, as are the upper-level vertical velocity fields. And as with the PBL sensitivity tests, these differences yield almost no sensitivity in the specific CI forecast in northwestern Kansas (Fig. 5.9). The new storms form at the same time and in a similar location in each scheme. Convection in the WRF schemes grow upscale slightly faster than other schemes, though the differences are minor. Though the initiation is forecast similar between each scheme, the new convection is much weaker at later lead times in the Thompson and Morrison schemes (Fig. 5.10). Since these two schemes produced the weakest cold pools but have little differences in CAPE/CIN, it is possible that lifting behind the cold pool (i.e. gravity waves) is sustaining some of the storms after initiation.

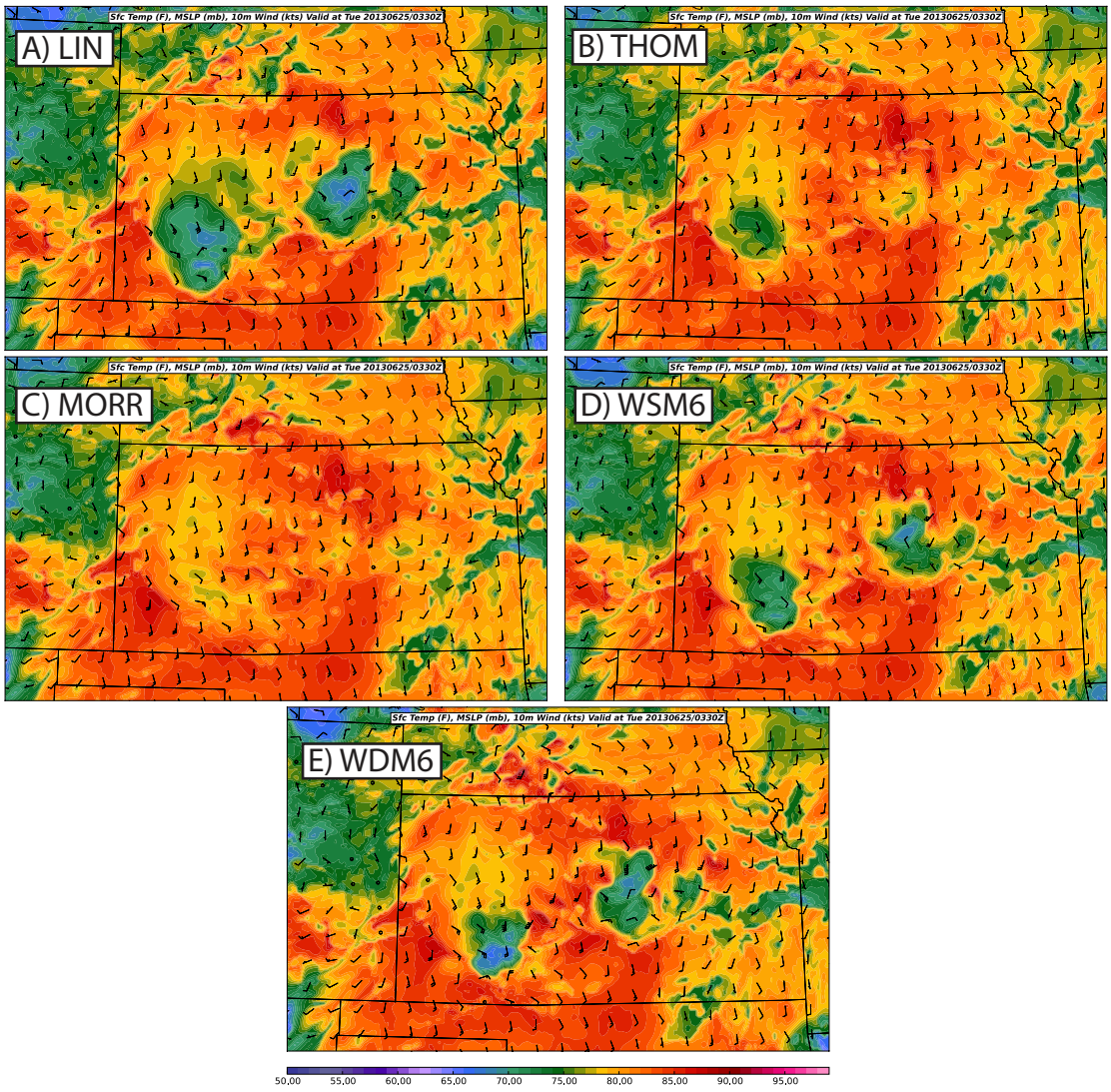


Figure 5.7: As in Fig. 5.6 but for surface temperature (°F).

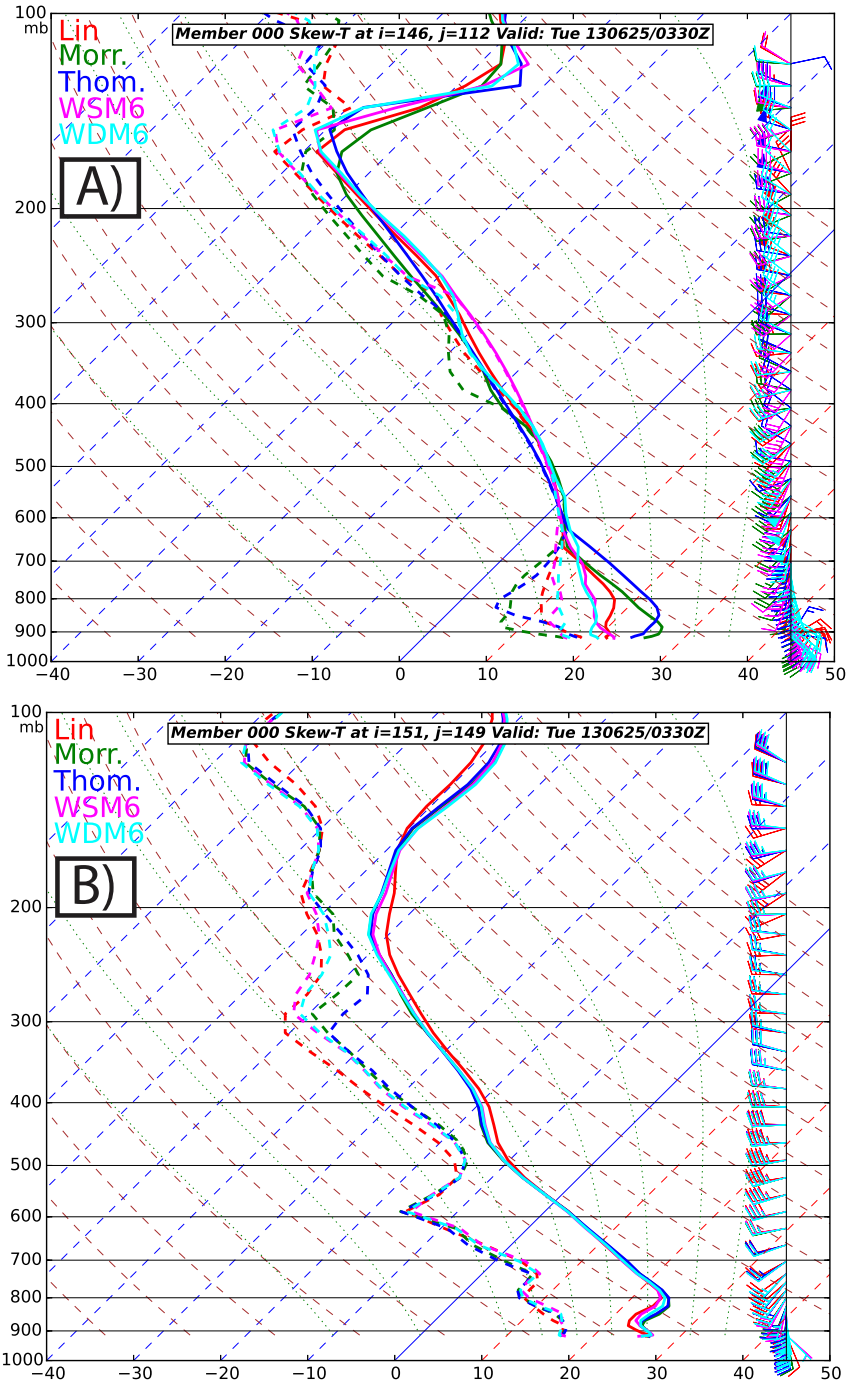


Figure 5.8: Ensemble mean soundings from (a) within the cold pool; and (b) ahead of the cold pool for each microphysics scheme.

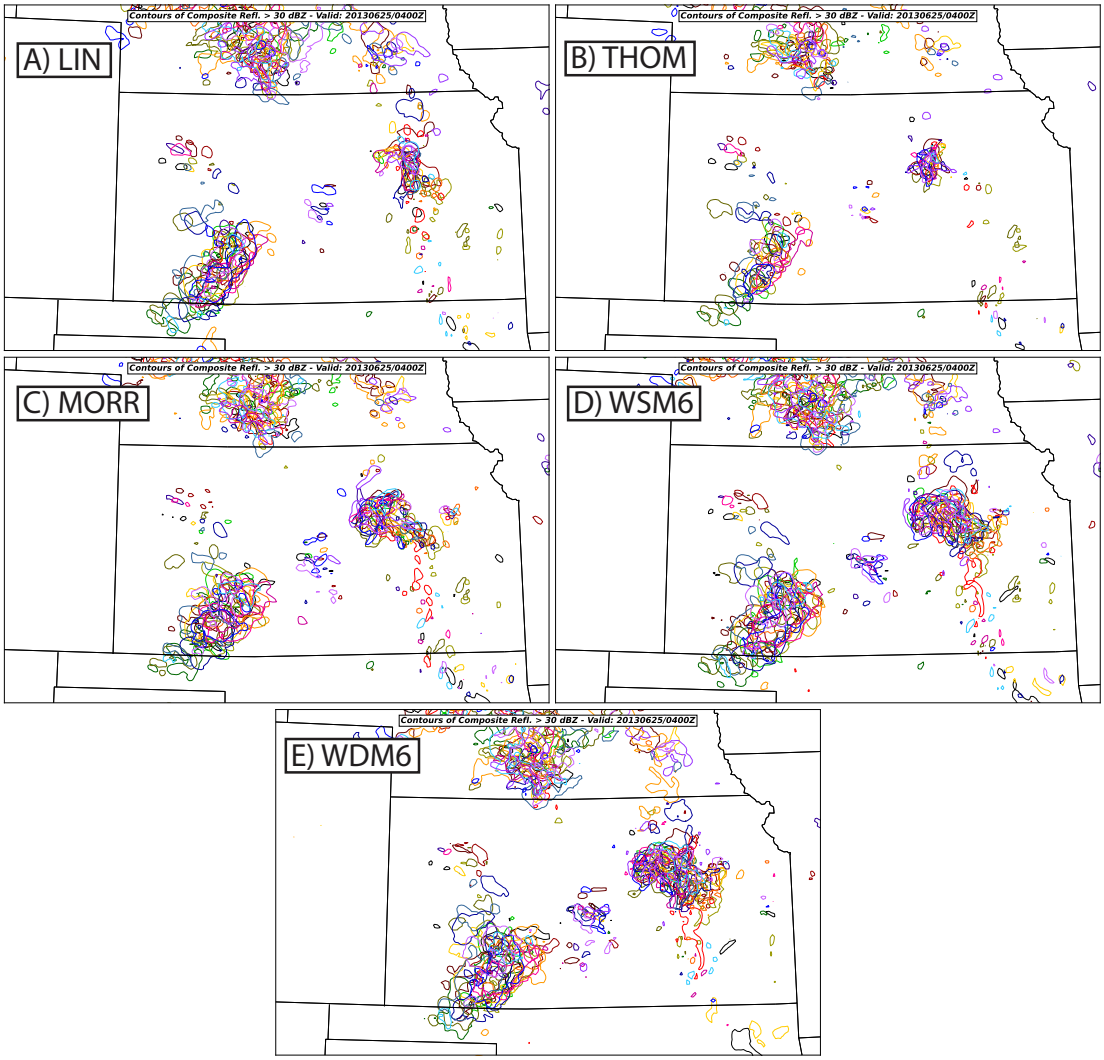


Figure 5.9: As in Fig. 5.6 but at 0400 UTC and for the spaghetti contours for each ensemble member of composite reflectivity greater than 30 dBZ.

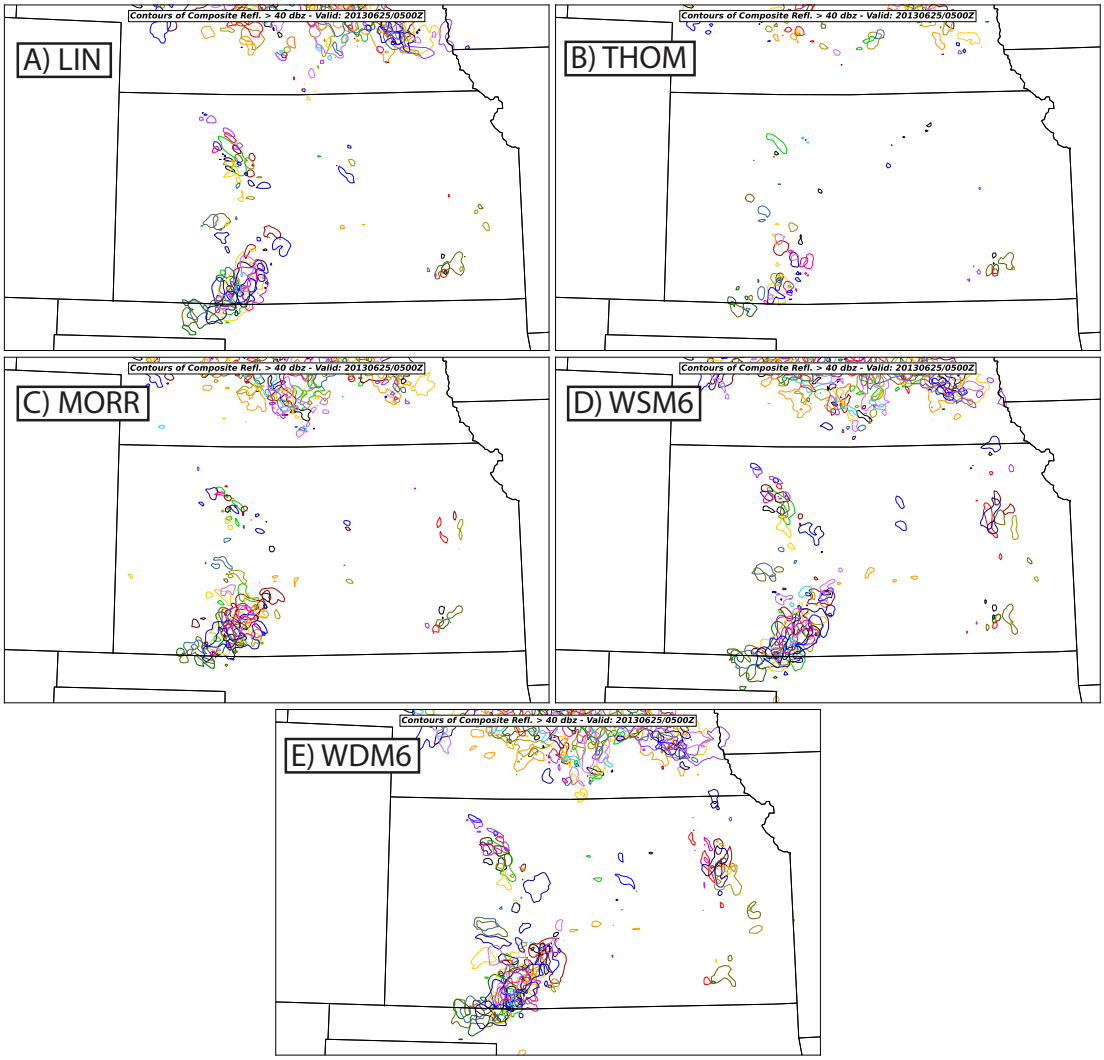


Figure 5.10: As in Fig. 5.9 but at 0500 UTC and for the spaghetti contours for each ensemble member of composite reflectivity greater than 40 dBZ.

Chapter 6

Convection initiation mechanisms

In order to highlight the mechanisms responsible for CI in this event, the final section of results will focus on a single member of the 20 ensemble forecasts for the allDA experiment. As allDA has been proven to give the best results, there is confidence in it producing the most physically realistic forecast. Member 3 is chosen as, though it produced the CI late and with a slight western bias, it gives the best subjective results consistent with the structure of the observed storms (Fig. 6.1). The first echo can be seen in the model at around 0415 UTC, over an hour later than the first observed storms in the area (at $\sim$ 0230 UTC). However, the location and structure of the storms in this member, as well as the quick evolution into a quasi-linear structure, is well forecast. Thus we will assume the results from member 3 of the allDA experiment as "quasi-truth" and analyze the mechanisms responsible for CI in this member.

6.1 Synoptic and mesoscale environment

Prior to the development of convection in northwestern Kansas, a strong upper-level wave can be seen moving through western Kansas at 0300 UTC (Fig. 6.2b). Interestingly, the CI occurred upstream of the main PV anomaly associated with this wave, an area in which large scale descent would be expected (marked by a

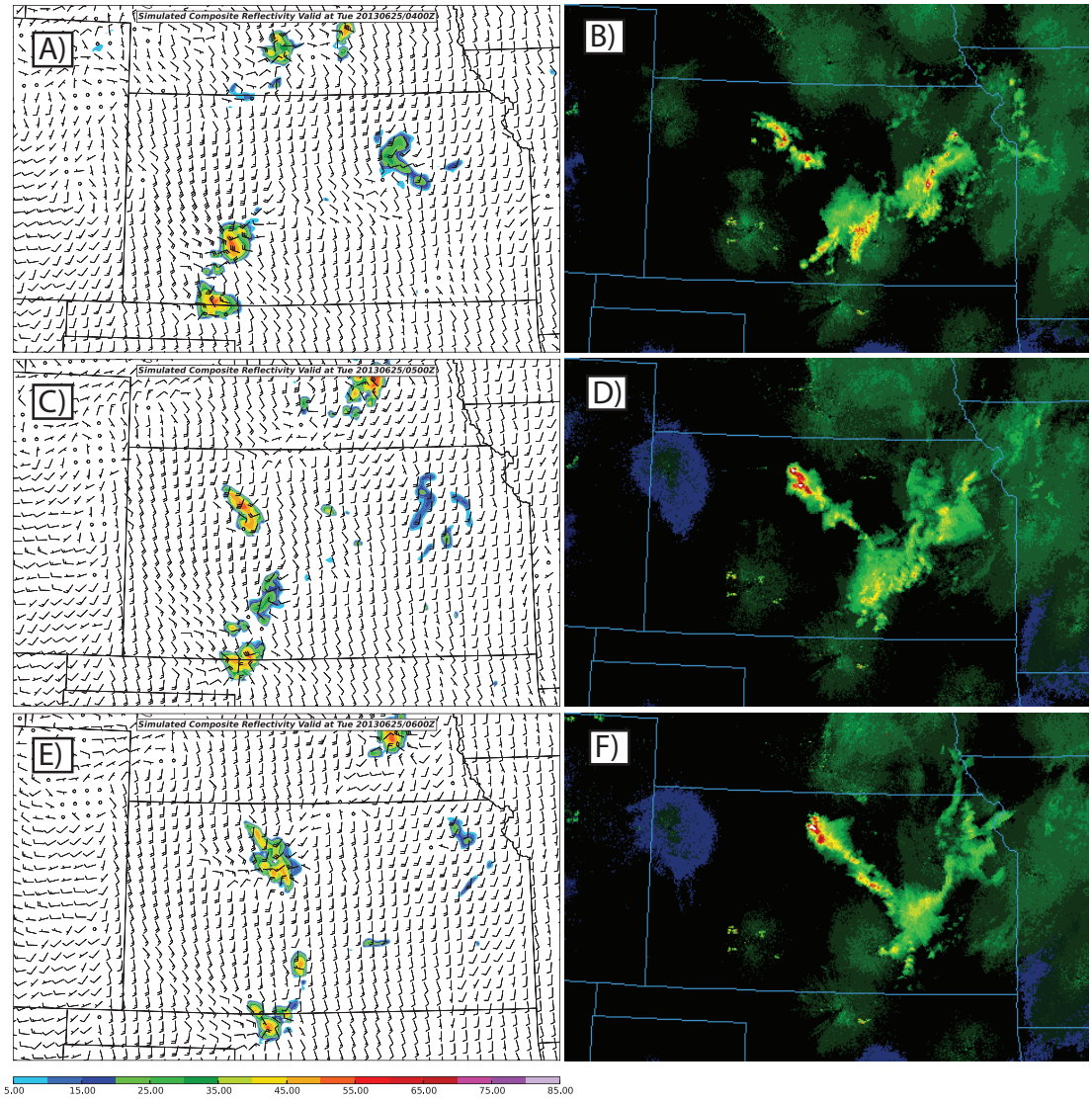


Figure 6.1: Composite reflectivity forecasts from allDA member 3 (a,c,e) and the corresponding 1 km AGL reflectivity observations (b,d,f) at (a,b) 0400 UTC; (c,d) 0500 UTC; and (e,f) 0600 UTC.

star in Fig. 6.2b). The weak dry line was located at the surface near the Colorado and Kansas border (Fig. 6.2a) with a northeast tilt and a large section bulging into northwestern Kansas. At this point the dryline was beginning to retreat back westward (and northward for the bulging section). Another boundary (warm front) was located in southern Nebraska stretching eastward. Additionally, a southerly LLJ of $\sim$ 30 - 40 kts was present at 850 hPa ($\sim$ 700 m AGL in western Kansas) that greatly strengthened with time. This has been mentioned many times in previous chapters, however we also now point out another developing jet max slightly higher above at 800 hPa ($\sim$ 1200 m AGL in western Kansas). As this jet veered with time, strong moisture convergence can be noted ahead of it (time series in Fig. 6.3).

The first surface cold pool of $\sim$ 78 °F produced by the convection in southern Kansas slowly moved northward into the region (Fig. 6.4) throughout the forecast. Ambient temperatures ahead of the cold pool were $\sim$ 85 °F. Some weak convergence could be noted along the outflow boundary in northern Kansas due to southerly winds enhanced within the cold pool. However this boundary moved beyond the region where CI occurs by 0200 UTC (2 hours prior to CI; approximate area marked by a star in Fig. 6.4). Together with the nocturnal cooling beginning to kick in (0200 UTC = 9 p.m. LST), the cold pool helped to quickly stabilize the lowest levels of the atmosphere. With the addition of the LLJ advecting warm air around 850 hPa, a strong surface-based inversion had developed. Mid-level lapse rates within this cold pool were also nearly adiabatic from 820 hPa up to 300 hPa, thus producing a region of sufficient MUCAPE ($\sim$ 2000 J kg^{-1} at 1500 m AGL) for elevated storms to develop (recall Fig. 4.16).

6.2 Sources of lift

The storms that developed in allDA member 3 were "pristine" in that they formed along no obvious surface boundary and were not directly connected to any

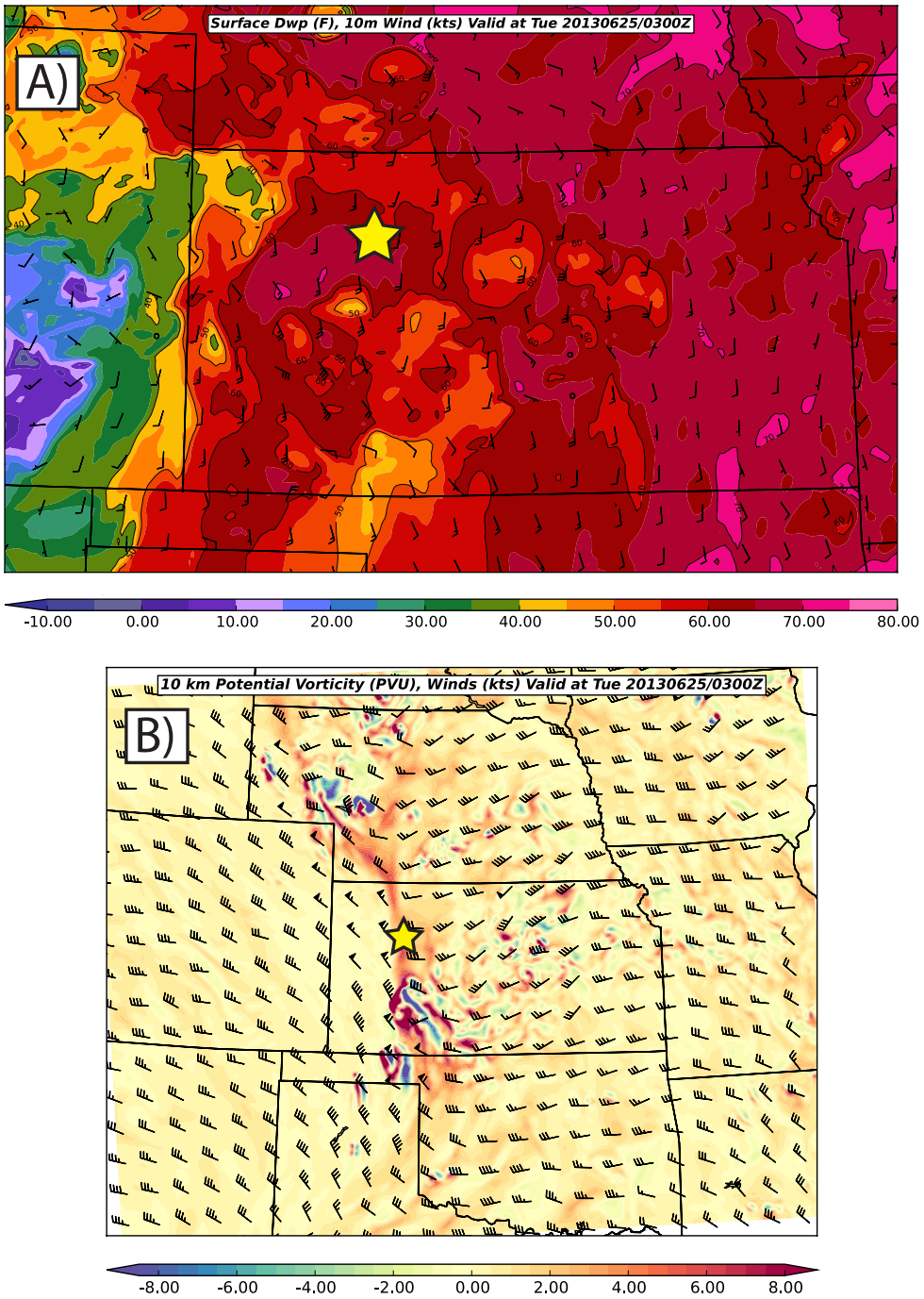


Figure 6.2: Forecasts valid at 0300 UTC from allDA member 3 of (a) surface dewpoint temperature (°F) and winds (kts); and (b) Potential vorticity (PVU) and winds (kts) at 10 km; and. The star in each plot indicates the simulated location of CI at $\sim$ 0415 UTC.

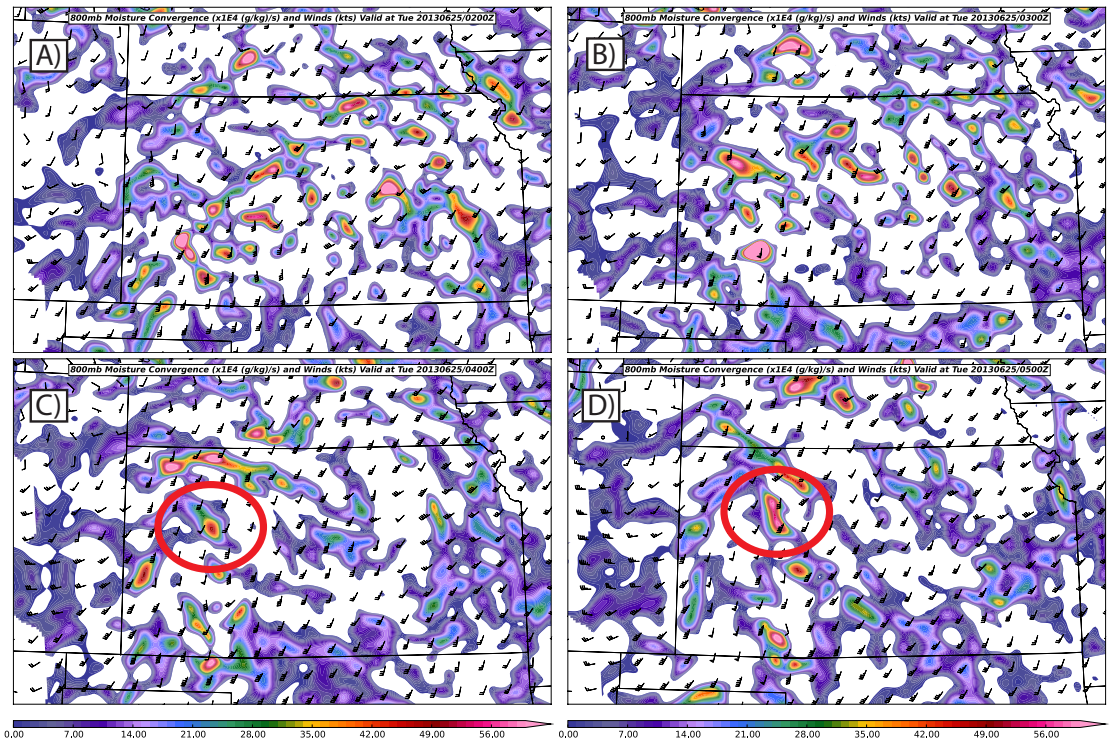


Figure 6.3: Forecasts from allDA member 3 of 800 hPa moisture convergence ($*10^4$ g kg^{-1} s^{-1}) valid at (a) 0200; and (b) 0300; (c) 0400; and (d) 0500 UTC. The circle in (c,d) indicates the location of the LLJ convergence.

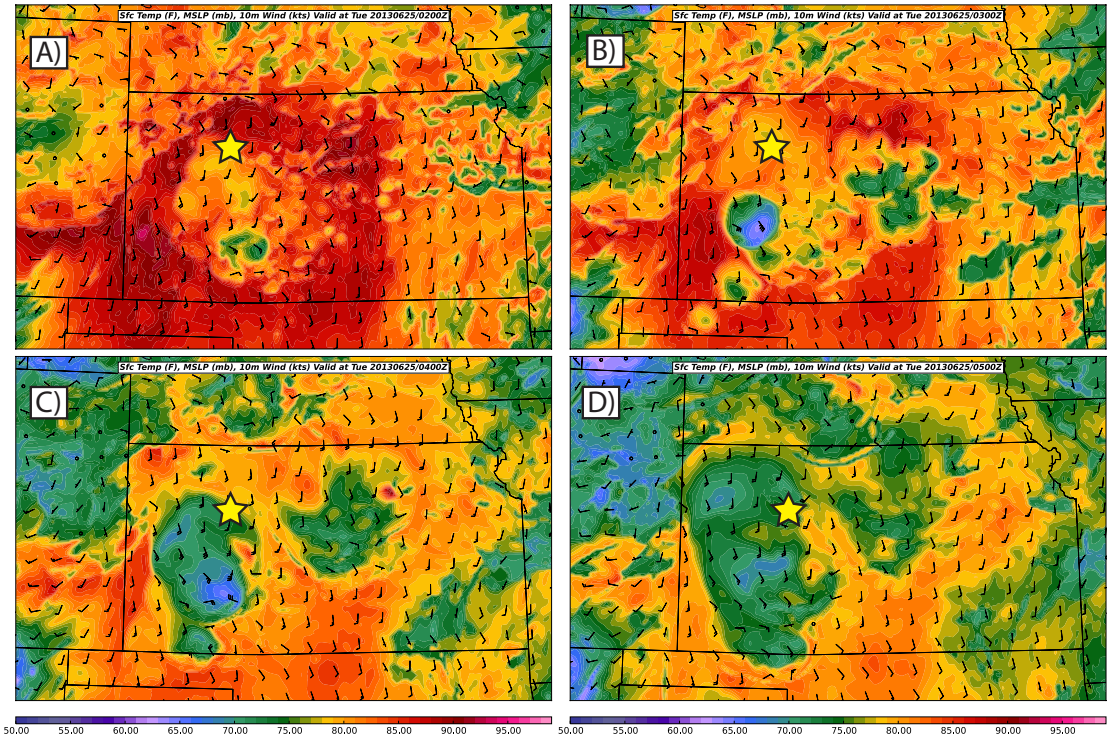


Figure 6.4: As in Fig. 6.3 but for surface temperature (°F) and winds (kts). The star in each plot indicates the simulated location of CI at $\sim$ 0415 UTC.

ongoing convection. By 0245 UTC, a second, stronger cold pool was produced by the storm in southern Kansas with temperatures within it closer to 68 °F (Fig. 6.4b-d). This boundary moved through the region of CI at $\sim$ 0400 UTC, just before CI occurred. There was again some convergence ahead of this second cold pool though it would not likely have been strong enough to lift surface-based parcels to their LFC of nearly 4 km. To determine any additional mechanisms responsible for lifting elevated parcels to their LFC, forward trajectories are presented in Fig. 6.5. The particular parcel chosen for this figure begins just east of the dryline at 3.25 km and moves northeast with the mid-level steering flow. It undergoes moderate lift for about 3 hours until it quickly ascends upwards at 0430 UTC from just under 6 km to above 7 km in 15 minutes (i.e. reached its LFC). West-to-east cross-sections are now taken through the y-location of this parcel in time (Figs. 6.6). Early on, the parcel follows the 320 K isentrope of potential temperature as it undergoes steady lift from west to east. The positive PV anomaly can be seen in Fig. 6.6a just west of the -100° longitude line and extending below 12 km. Another weaker, positive anomaly extending below the tropopause followed behind just east of the -102° longitude line; additional areas of positive PV are present between 6 and 8 km. The early parcel ascent between 0130 and 0300 UTC appears to be connected to large-scale synoptic lift associated with either the PV anomaly or the sloped isentropes near the dryline. These are also potentially connected, with the PV anomaly acting to "pull" the isentropes upwards near the surface and actually aiding in the development of the dryline.

This parcel goes through a phase of weak ascent between 0230 and 0300 UTC. At 0300 UTC, it interacts with a band of stronger ascent closer to the surface, seen circled in Fig. 6.6b, and begins to rise again. This band features vertical velocities greater than 1 m s^{-1} and moves with a westward component in time. Between 0345 and 0400 UTC, the parcel again interacts with another area of positive vertical

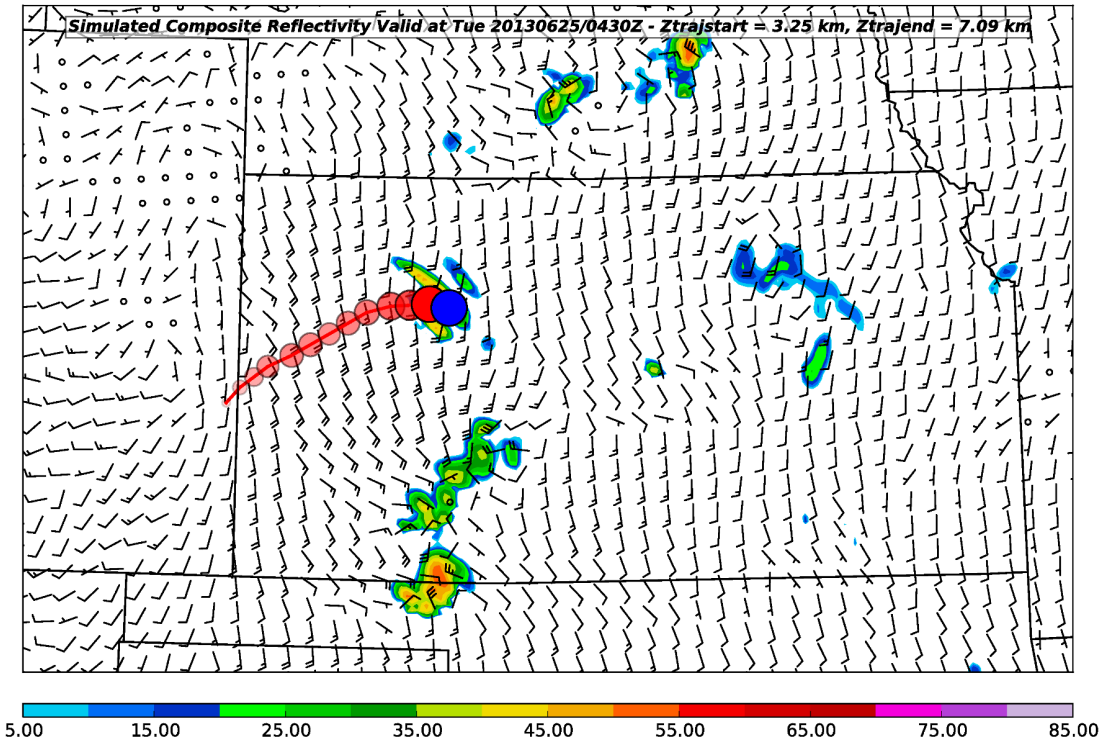


Figure 6.5: Forward trajectory of a parcel originating just east of the dryline at 0130 UTC and ending under the location of CI at 0430 UTC (in blue) for allDA member 3. The opacity and size of the red dots are proportional to the height AGL of the parcel.

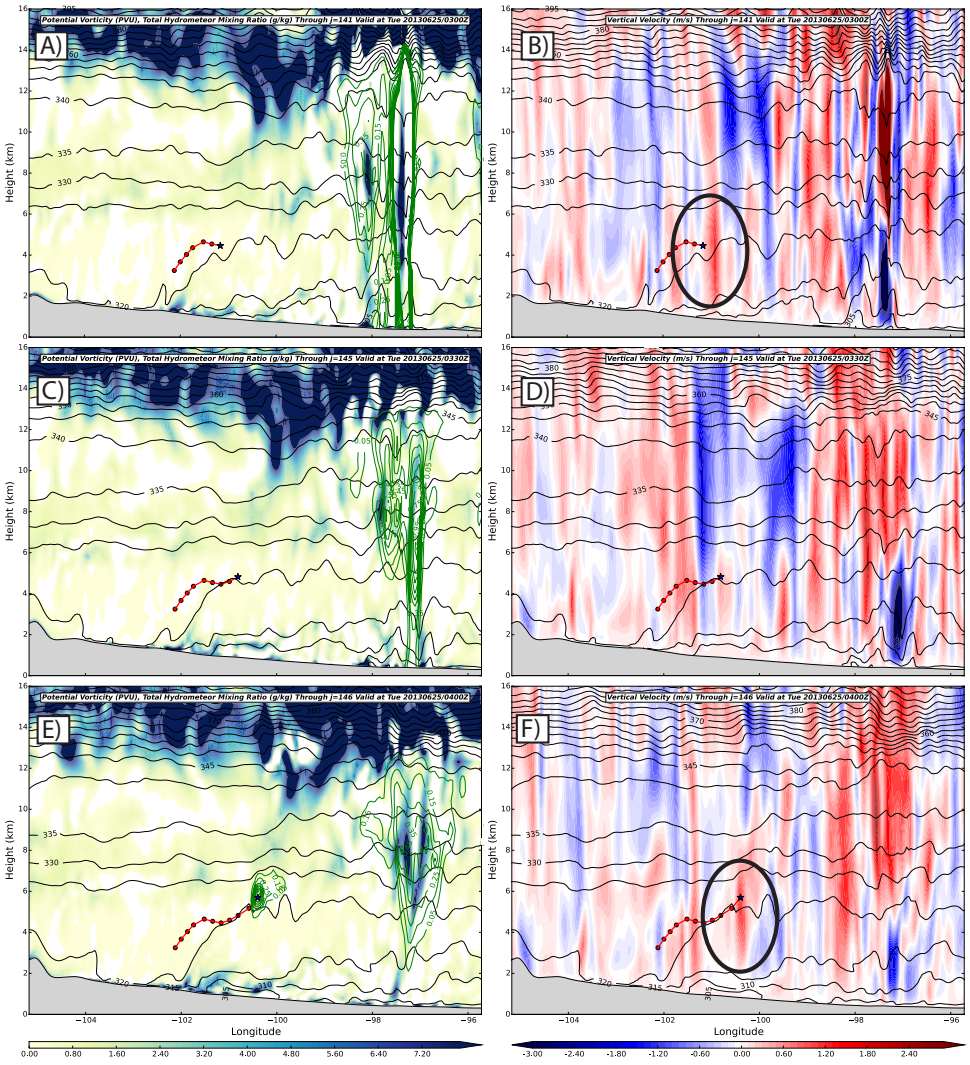


Figure 6.6: Forecast from allDA member 3 of east to west vertical cross-sections through the y-location of the parcel trajectory's location at (a,b) 0300; (c,d) 0400; and (e,f) 0500 UTC. Plotted in (a,c,e) are potential vorticity (fill, PVU), total hydrometeor mixing ratio (green contours, g kg^{-1}), and virtual potential temperature (black contours, K). Plotted in (b,d,f) are vertical velocity (fill, m s^{-1}) and virtual potential temperature (black contours, K). The parcel trajectory is the same as the 2D trajectory in Fig. 6.5. See text for description of circles.

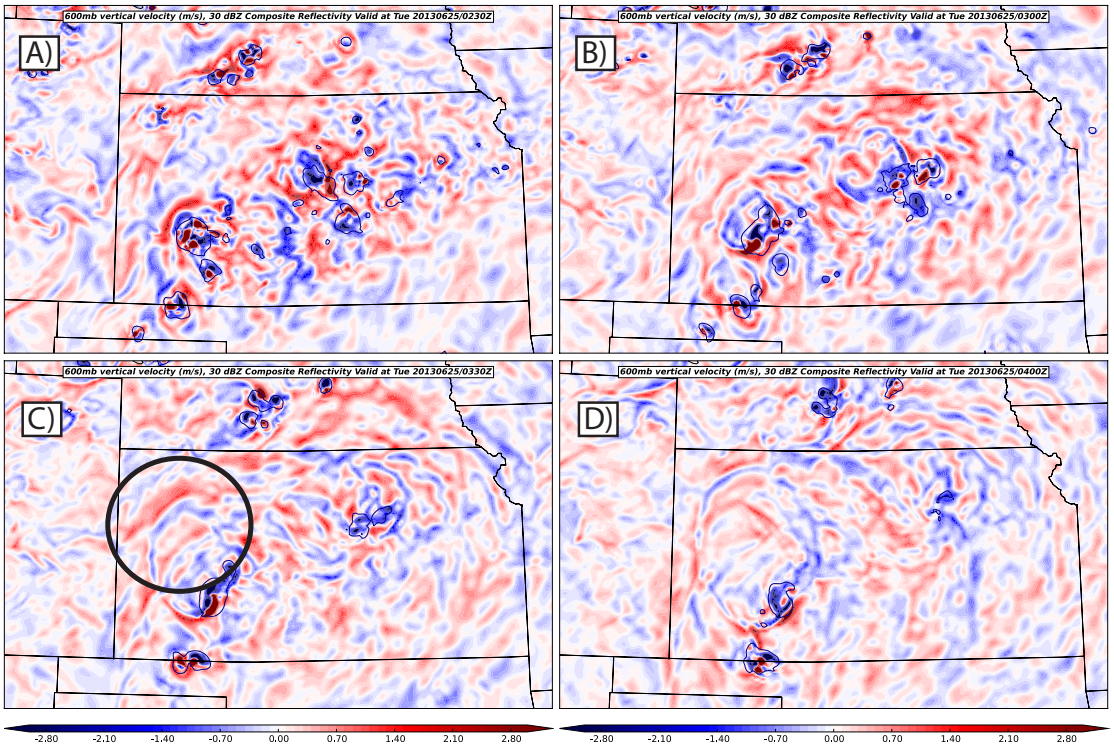


Figure 6.7: Forecasts from allDA member 3 of 600 hPa vertical velocity (m s^{-1}) valid at (a) 0230; and (b) 0300; (c) 0330; and (d) 0400 UTC. The circle in (c) indicates the location of the two positive vertical velocity bands. Also overlaid on each plot is the 30 dBZ composite reflectivity contour.

velocity (again, circled in Fig. 6.6f). This second band is enough to lift the parcel to 6 km where it can reach its LFC. These two bands can be better seen via a 2D plot of vertical velocity at 600 hPa (Fig. 6.7; circled bands at 0330 UTC). They both appear to move outwards from the previous convection in southwestern Kansas. At 0400 UTC, the banded structure of the new convection begins to appear in the vertical 2D vertical velocity field. Also at the same time, hydrometeors begin to form at 6 km as saturation occurs (Fig. 6.6e). The base of the updraft extends down to $\sim$ 3 km (2 km AGL) thus proving that the new CI is truly elevated.

6.3 Two-dimensional discrete cosine transformation

We can further determine the cause of these two bands by utilizing a two-dimensional discrete cosine transformation (2D-DCT; Denis et al. 2002), commonly used for the compression of digital images. The 2D-DCT produces an array of spectral variances in which the spatial scales are related to the 2D wavenumbers. This field can then be multiplied by a transfer function array to rebuild a specific filtered physical field (see Denis et al. 2002 for more details). Put simply, we can use the 2D-DCT to split the 2D field of 600 hPa vertical velocity (Fig. 6.7c) into its individual components at different scales (Fig. 6.8). It is now possible to identify three main features: 1) a mesoscale feature at scales greater than 100 km likely tied to the surface outflow boundary (green circle); 2) another mesoscale feature likely tied to a region of enhanced convergence at the terminus of veering low-level jet at 800 hPa (blue circle); and 3) wave features at the smaller scales less than 50 km indicated by the alternating positive and negative arcs emanating from the southern convection (time series of only scales < 50 km given in Fig. 6.9). Similar wave trains can also be seen emanating from northern convection in northeastern Kansas.

6.3.1 Mesoscale sources of lift

To demonstrate the cause of the mesoscale features in Fig. 6.8b, see Fig. 6.10. The leading band described in (1) is spatially and temporally correlated with an area of enhanced moisture convergence near the surface, consistent with the second outflow boundary moving northward (green circles in Figs. 6.8b and 6.10a). Since the thermodynamic profile was nearly dry adiabatic above the surface inversion, it is reasonable for any such lift to be vertically deep. As the low-level jet begins to strengthen and veer, a second area of enhanced surface convergence becomes apparent just above the surface (red circles in Figs. 6.8b and 6.10b) and south

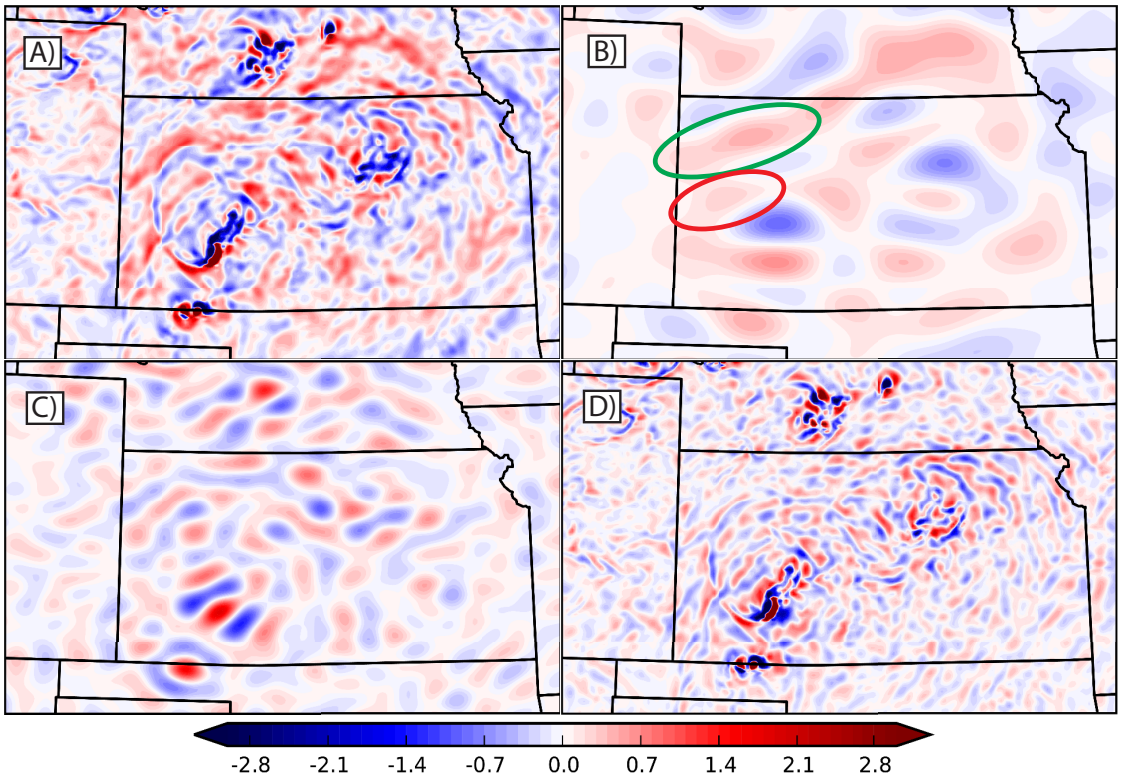


Figure 6.8: Two-dimensional discrete cosine transformation of the 600 hPa vertical velocity (m s^{-1}) field from Fig. 6.7c valid at 0330 UTC. The original plot is given in (a), while different scales of wavelengths (b) greater than 100 km; (c) between 50 and 100 km; and (d) less than 50 km are shown. See text for description of circles.

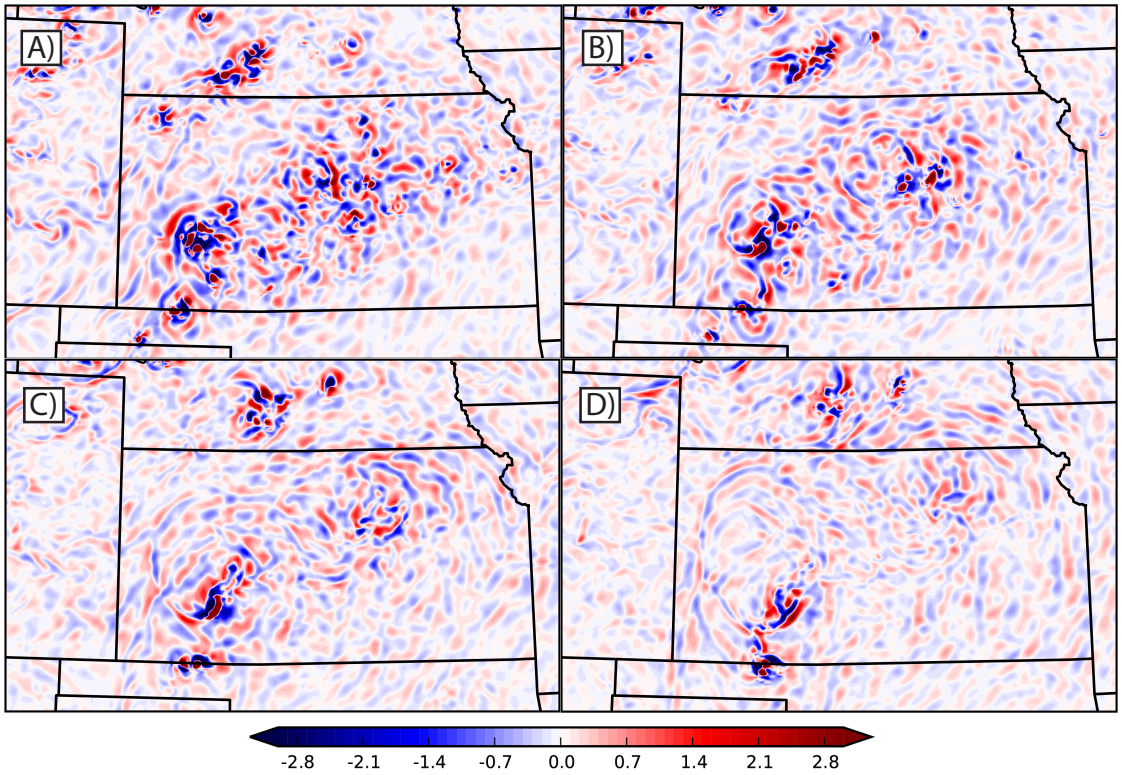


Figure 6.9: As in Fig. 6.8d but at (a) 0230; (b) 0300; (c) 0330; and (d) 0400 UTC.

of the lift produced by the outflow boundary. This band moves north and east with time as the LLJ begins to move eastward. As the jet veers (and the jet core moves eastward), the southerly flow encounters more westerly flow and hence produces stronger convergence over time; this is a common area for nocturnal CI (Josh Gebauer 2016, personal communication). The first convective echoes that form feature a similar orientation to the convergence produced at the jet terminus, leading further credence to the hypothesis that the lift associated with the LLJ is the final push up the LFC.

6.3.2 Gravity wave analysis

To determine whether the banded structures in (3) are gravity waves, we apply an analysis similar to Marsham et al. (2011). Internal gravity waves propagating in the x-z plane in a stratified system must satisfy the Taylor-Goldstein equation:

$$\frac{d^2w}{dz^2} + m^2w = 0 \tag{6.1}$$

where

$$m^2 = \frac{N^2}{(U-c)^2} - \frac{U''}{(U-c)} - k^2 \tag{6.2}$$

or $m^2 = l^2 - k^2$. l^2 is referred to as the Scorer parameter (1949); k^2 is the horizontal wavenumber; N^2 is the Brunt-Väisälä frequency; U is the wind speed in the direction of wave propagation; U'' refers to the second derivative of the wind speed with respect to height (i.e. curvature of the wind); and c represents the gravity wave phase speed. Gravity waves are often observed propagating on a stable layer near the ground with a deeper, weakly stratified layer aloft. However, a separate mechanism is needed in order to prevent the wave energy from escaping upwards (Crook 1988). Without any trapping of wave energy, most of the energy from a gravity wave will radiate away from the stable layer by the time air has traveled from one crest to the next. Scorer (1949) determined that to obtain

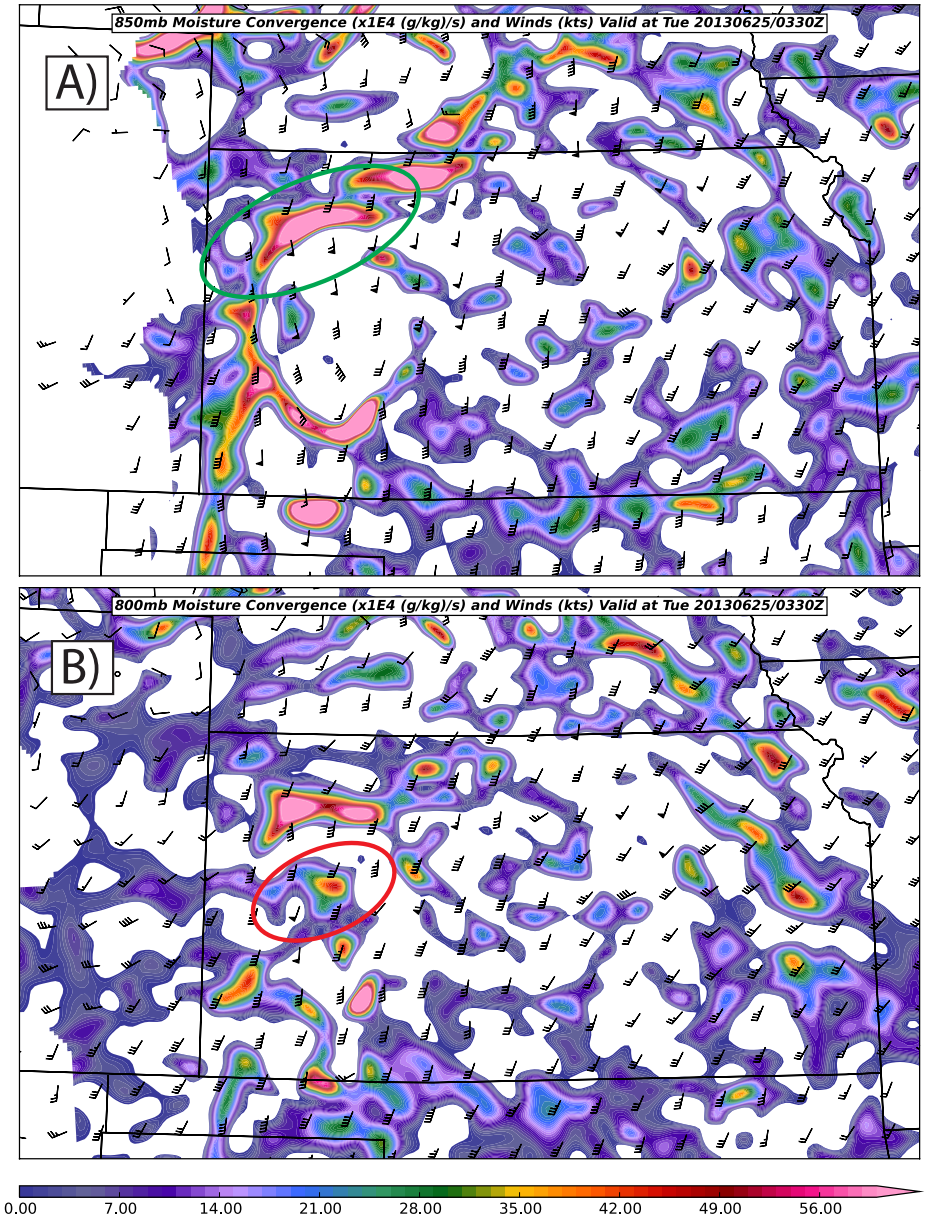


Figure 6.10: Forecasts from allDA member 3 of moisture convergence ($*10^4$ g kg^{-1} s^{-1}) at (a) 800 hPa; and (b) 850 hPa valid at 0330 UTC. The green circle indicates convergence at the cold pool, and the red circle indicates convergence at the terminus of the LLJ.

significant energy at the ground, the l^2 term must decrease with height. In any layer where $l^2 < k^2$, the propagating waves would change from propagating in the vertical to decaying and thus energy in those wavelengths would be trapped below. Though it is difficult to know the exact propagating wavenumber k^2, this requirement will always be satisfied for any negative values of the Scorer parameter (since k^2 is always positive). Using simulations from a non-hydrostatic numerical model, Crook (1988) found three common mechanisms that are able to prevent wave energy from escaping upwards and produce long period gravity waves. The first mechanism occurs when winds in the upper layer oppose the wave motion, thereby reducing the Scorer parameter in the upper layer (through increasing the magnitude of $[U - c]^2$) and causing waves to evanesce. The second occurs when a jet exists in the lower layer that opposes the wave motion. The curvature in the velocity profile above this jet increases U'' causing the second term to dominate and produce a layer of negative Scorer parameter. Lastly, the third mechanism, unrelated to the Scorer parameter, involves an elevated inversion above the lower stable layer in which wave energy can be reflected back downwards and lead to an enhancement of wave amplitude near the ground.

As a first check to further determine whether the features discussed in this section are possibly gravity waves, we estimate the phase speed of gravity waves produced from a sounding just ahead of the waves in space and time (Fig. 6.11). Eom (1975) solved a two-layer, two-dimensional simple model for the phase speed of gravity waves corresponding to adiabatic, compressible, hydrostatic and inviscid flow in a non-rotating coordinate system. In this model, each layer was assumed to have a constant stability parameter and mean depth, and also that the mean flow is non-zero in the upper layer only. By applying the perturbation method and linearizing the system of equations following a steady basic state, the phase speed of gravity waves can be solved for via a system equations detailed in Eom (1975).

To apply this model, we choose the lower stable layer to extend from 860 to 800 hPa, and the second layer from 800 to 520 hPa. After rotating the coordinate system for waves propagating along 115° (to the northwest) and correcting for the assumption of no mean flow in the lower layer, we calculated a most probable gravity wave phase speed of 28 m s^{-1}. The system of equations presented by Eom (1975) actually produces five possible speeds; this value was assumed to be the most physical for this situation. To compare this estimated speed to that of the features being discussed, the distance between wave crests at four different output times (temporally spaced by 15 minutes) was measured to produce an "observed" speed of 31 m s^{-1}. Note that the background flow as deduced by the sounding in this region was only $\sim$ 24 m s^{-1}. In the case study presented by Eom (1975), the author estimated phase speeds of 49.5 and 52.0 m s^{-1}, which he describes as "remarkably close" to the observed disturbance propagation speed of 50 m s^{-1}.

The same sounding in Fig. 6.11 is used to calculate the different components (Fig. 6.12a-c) of the Scorer parameter in Fig. 6.12d. The Scorer parameter calculation requires a given value for the phase speed of the wave, c. Though we do have an estimated value of 28 ms^{-1}, c was allowed to vary in the calculations to account for possible errors in the Eom (1975) model. The sounding does feature a nearly dry adiabatic layer aloft of a stable layer from the surface to $\sim$ 850 hPa through which gravity waves would be able to form. This can also be seen by a layer of largely decreasing N^2 (Fig. 6.12a). As mentioned earlier, a layer capable of trapping wave energy would be demonstrated by a region where the Scorer parameter becomes negative. For all gravity wave phase speeds, a trapping layer exists between 300 and 400 hPa which is consistent with the maximum heights of the positive vertical velocity bands (not shown). Since the opposing flow term, ($[U - c]$; Fig. 6.12c) is negative for all phase speeds above 600 hPa, as well as the curvature in the wind being negative (i.e., veering) between 300 – 400 hPa (Fig. 6.12b); the second term

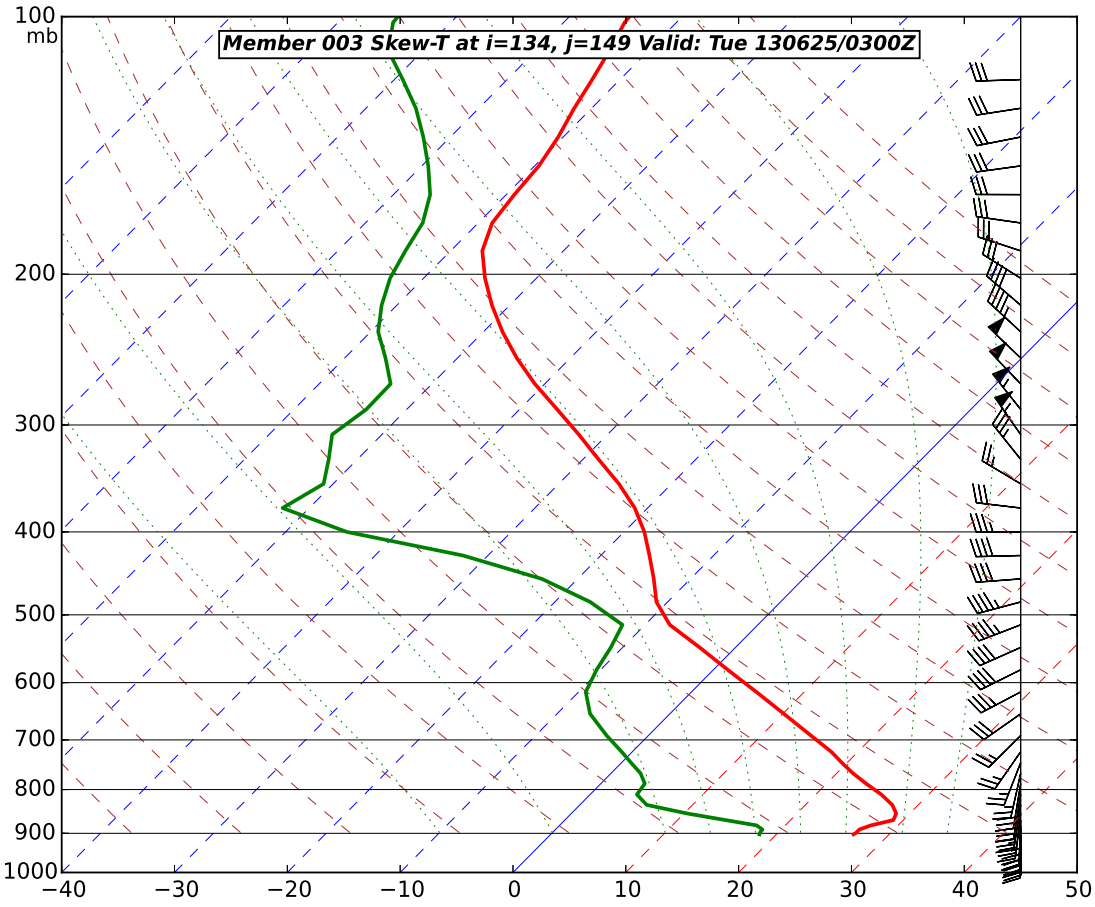


Figure 6.11: Sounding from just ahead of the potential gravity waves in Fig. 6.9b at 0300 UTC which is used to calculate the potential phase speed following Eom (1975).

in (6.2) dominates and thus the entire value becomes negative. For gravity wave phase speeds greater than 15 m s^{-1}, there exist another trapping around 600 hPa that arises due to the same reason, though it only occurs at greater phase speeds due to the weaker opposing flow in the layer. These trapping layers are similar to the first method described in Crook (1988).

Crook (1988) found in his simulations that the maximum vertical velocity obtained in these trapped waves can reach as high as 8 – 10 m s^{-1}, much faster than those produced by the banded features in our simulations of 1 – 2 m s^{-1}. However, the trapping layer in the Crook (1988) paper was much closer to the surface at $\sim$ 2 km, while there would be more wave energy damped in our simulations due the trapping layers being located higher in the atmosphere. These results indicate that the environment produced in allDA member 3 was capable of producing trapped gravity waves. And given that the estimated phase speed of gravity waves following Eom's (1975) model was extremely close to the speed of the banded features, we conclude that these features are trapped internal gravity waves. Worth noting is that the 49 vertical levels (compared to the 80 used in Crook 1988) used in our simulations is rather low for fully resolving vertically-propagating waves. Experiments in the future will examine the sensitivity of vertical grid levels to features such as these.

6.4 Summary of CI

We now summarize the mechanisms likely responsible for CI with the following: parcels originated along the dryline and underwent weak, synoptic ascent due to either a positive PV anomaly or lift ahead of the dryline (likely related). After a period of weak descent for 30 minutes, the parcels moved into an environment classified by strong low-level stability induced by previous convection's northward-moving cold pool. However mid-level lapse rates were steep, yielding

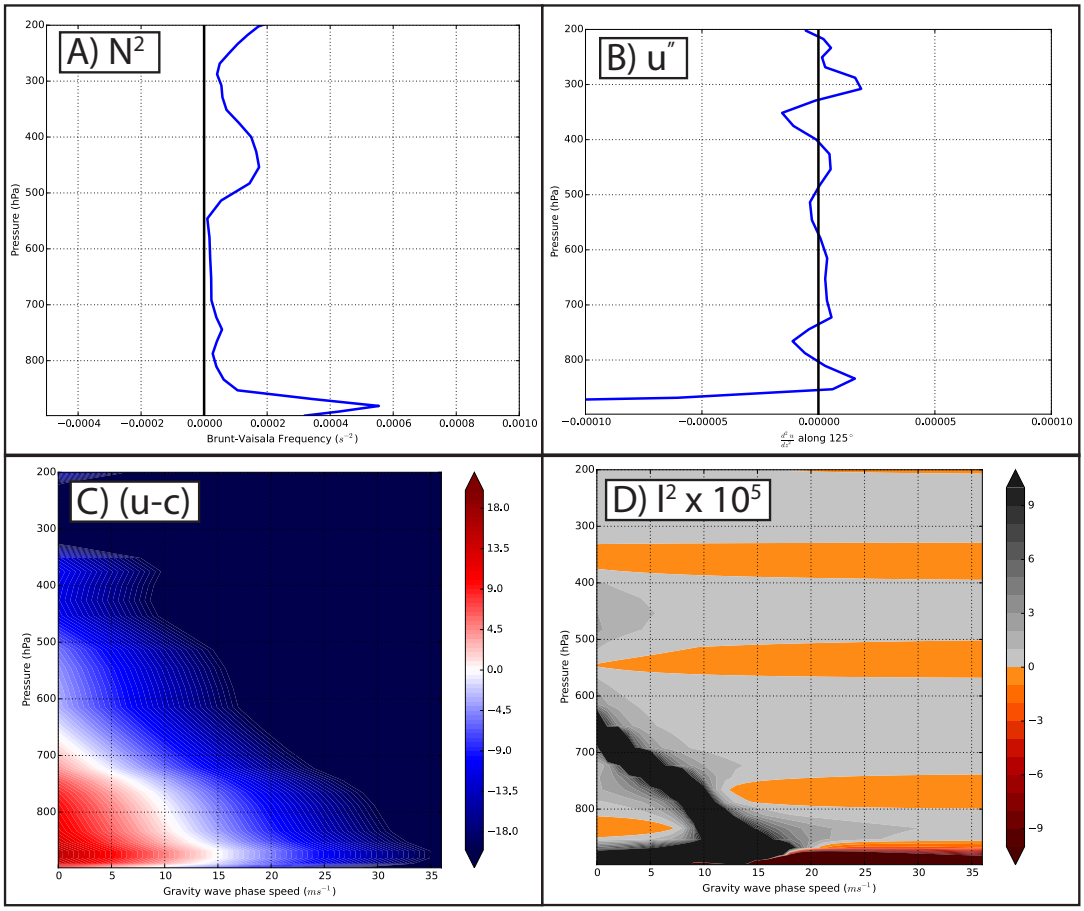


Figure 6.12: Individual terms of the Scorer parameter calculated from the sounding in Fig. 6.11 including (a) N^2; (b) u_{zz}; and (c) $(u - c)$. The final Scorer parameter profile is given in (d).

strong MUCAPE for elevated thunderstorms. There, they encountered a northward moving band of lift produced ahead of a cold pool as a result of convection in southern Kansas. A second band of lift produced by a veering LLJ provided the final push for parcels to reach their LFC and convect. These final two bands were structured and enhanced by trapped gravity waves propagating along the top of the second cold pool. A diagram and summary of these features is shown in Fig. 6.13. As discussed in the previous chapter, the Morrison and Thompson microphysics members did not produce a strong cold pool but were still able to generate the new CI in northwestern Kansas. However, these schemes did generate strong surface outflow boundaries ahead of their weaker cold pools. From this, we infer that though the cold pools were simulated differently, the gust fronts ahead of them, and their associated regions of convergence, were the important mechanisms able to sufficiently provide the early parcel lift. The boundaries are generated within 15-30 minutes after the final EnKF update cycle, thus suggesting that the DA process is potentially responsible for their production.

As the LLJ-produced convergence was the final push for parcels to reach their LFC, we assume that it was the most important mechanism. The trapped gravity waves only served to structure and enhance the lift produced by the LLJ; therefore it is possible that the convection still would have formed in their absence. However, outflow boundaries, LLJ convergence, and gravity waves were seen in each of the convDA and allDA (including the physics sensitivity tests) simulations discussed in this thesis. Since no successful forecasts were found without these mechanisms, we cannot rule out that each one played an important part in the CI process. Additionally, the convection produced by Morrison and Thompson schemes also fell apart within 2 hours of its formation, as opposed to the other schemes in which the convection quickly grew upscale. Though the gravity waves were produced by these two schemes, the maximum vertical velocities within them were weaker

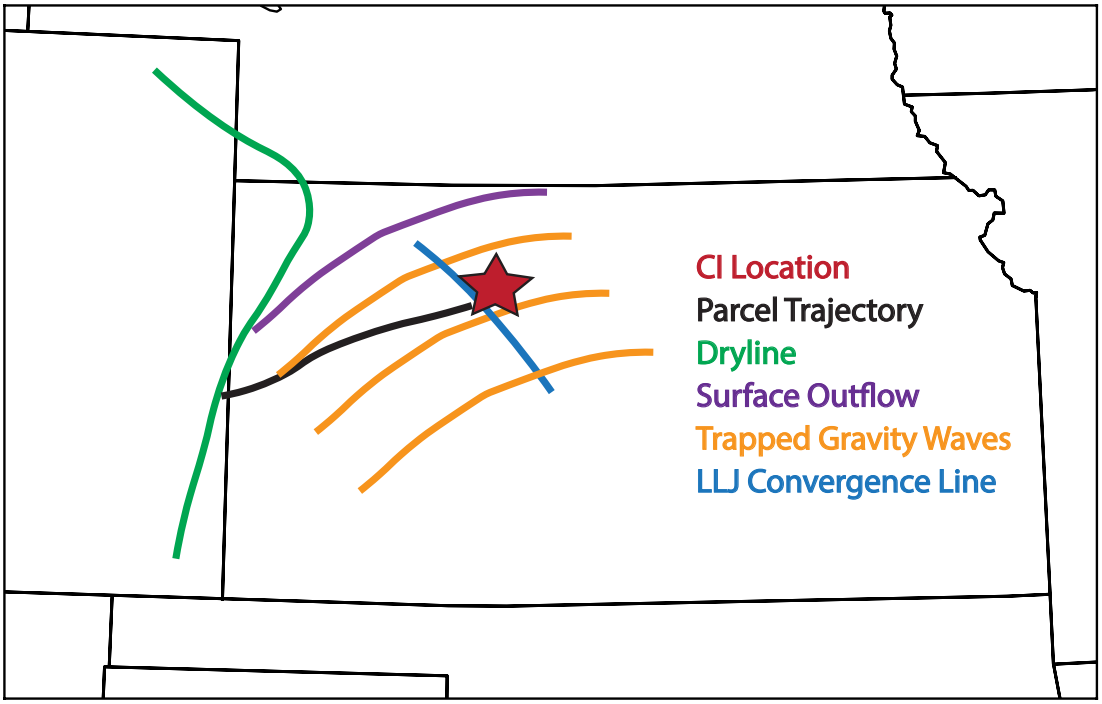


Figure 6.13: Schematic of the features likely interacting in order to generate CI for the 25 June 2013 nocturnal CI event. The parcel trajectory is also shown in black.

(0.5 m s^{-1} in Morrison, 1 m s^{-1} in Thompson, and upwards of 2 m s^{-1} in Lin), thus suggesting that the gravity waves were partly responsible for sustaining the convection after its initiation. Since the waves were moving northwestward and the storms eastward, the new convection would be provided with further support due to their interaction with additional wave crests. As the cold pools were weaker in the Morrison and Thompson schemes, the perturbation into the neutral layer aloft and resulting gravity waves were weaker.

It is difficult to verify whether the actual observed storms were produced by these same mechanisms due to the lack of a dense observation network in Kansas. However, Marsham et al. (2011) observed a similar event of CI produced by the interaction of trapped waves and a convergence line produced by an LLJ. We can thus assume that the CI produced by member 3 in the allDA experiment, also considering its similar structure and evolution to the observed convection, is reasonable.

Chapter 7

Conclusions

7.1 Summary of results

Though it can be important both economically and for severe weather threats, nocturnal convection is often difficult to forecast both in NWP models and by skilled human forecasters. As nocturnal convection is usually elevated, it isn't often as easy as simply locating surface boundaries for preferred areas of development. Multiple mechanisms are also commonly responsible for initiating nocturnal convection; they can occur and interact at many scales which are often difficult for weather models to predict. On 25 June 2013, a nocturnal CI event occurred with little warning from both operational forecasters and NWP models. After a weak MCS began to fall apart in southern Kansas, storms initiated around 0300 UTC with no obvious boundaries responsible for their formation. By using an advanced multi-scale DA system, we found positive impact in convection-allowing ensemble forecasts from both conventional and radar data assimilation for this event. Though observations were not present to verify these conclusions, the CI appears to have been generated by the interaction of synoptic scale lift, a surface outflow boundary, a veering nocturnal LLJ, and trapped gravity waves. These interactions are similar to an observed event from the IHOP experiment described

in Marsham et al. (2011) in which CI occurred at the interaction of trapped waves and a convergence line produced by the LLJ.

Conventional observations, even though they are mostly located at the surface after 0000 UTC, were able to greatly improve the thermodynamic and kinematic environments for nocturnal convection. The EnKF analysis produced mesoscale environments more supportive of strengthening convection in southern Kansas that, in turn, produced strong surface outflow ahead of its cold pool and was able to provide deep lift throughout the lower troposphere. The trapped gravity waves also formed as a result of this cold pool. Surface observations included in DA also further enhanced convergence produced at the terminus of the LLJ by weakening 850 hPa winds throughout parts of northern Kansas. While radar assimilation alone was not enough to capture the CI, it did provide improvements by better resolving earlier convection during the forecast period and by also reducing the amount of spurious precipitation in other parts of Kansas. Our simulations indicate that the cold pool and resulting gravity waves are important for the generation of new nocturnal convection. These features form as a product of ongoing convection, which is greatly improved upon in the analysis through the assimilation of radar data. Though the convDA experiment in this case was sufficient to produce the ongoing convection in southwestern Kansas, it is very possible that the use of radar DA in future experiments will show positive impacts by adding in previous convection responsible for generating cold pools and gravity waves. Additionally, from a forecaster's point of view, seeing a better analysis of current ongoing convection and less spurious storms in an NWP forecast would provide more confidence to an operational meteorologist.

In terms of the specific CI forecast, little sensitivity was found for both PBL and microphysical parameterization schemes used during the forecast period. Local and nonlocal closure PBL schemes produced different cold pool sizes and different

LLJs. However, apart from these and some minor thermodynamic differences, there was almost no difference in the CI forecast. The microphysics schemes tested produced different reflectivity structures for the convection in southern Kansas which also impacted the surface due to evaporation and cold pool differences. Though Morrison produced an extremely weak cold pool, outflow boundaries were enough to provide some lift and the converging LLJ was enough to push parcels to their LFC. These results indicate that deciding on a particular PBL and microphysics scheme, as opposed to common results for diurnal convection, isn't largely important for elevated convection. Elevated storms, which represent a majority of nocturnal convective systems, tend to be disconnected from the surface. However, the physics schemes are responsible for producing the pre-storm thermodynamic and kinematic environments that the features responsible for CI form within. With lead times of only 2 hours, which is common for CI-specific studies, the pre-storm environment has already been largely determined by the DA process. Thus it is possible that utilizing different schemes during DA, or extending the forecast lead time, would produce stronger sensitivities. Additionally, this result is likely to be extremely case-dependent; additional studies for other nocturnal CI events (similar to Johnson et al. 2016), particularly ones with more unique observations available to verify against, are necessary.

7.2 Future work

This study only examined the sensitivity of a single nocturnal convective event to assimilated observations and physics configurations. The PECAN (Parsons et al. 2013) experiment took place during 2015 in order to advance the understanding of nocturnal precipitation in conditions with a stable boundary layer, nocturnal LLJ, and the largest CAPE located above the boundary layer. Events from this field project will provide dense datasets for similar assimilation and dynamical studies in

the future. During the PECAN campaign, numerous amounts of observations were taken during nocturnal convective events. Many of these observations were located at fixed stations (fixed PISAs; PECAN integrated sounding array) throughout Oklahoma, Kansas, and Nebraska, while others were located on mobile platforms (mobile PISAs). Observations located at PISA stations include thermodynamic profilers, radiosondes, Doppler wind Lidars, and conventional surface observations. The thermodynamic profilers are designed to observe the evolution of atmospheric instability and low-level temperature and humidity with high-temporal resolution in order to quantify CI potential. The kinematic profilers provide the ability to capture the evolution of lower-tropospheric wind and turbulence profiles, in order to quantify moisture transport, mesoscale convergence, and nocturnal LLJs. Additionally, the PISAs will also serve as a test-bed for the nationwide network of profiling systems, as advocated in the 2009 National Research Council report "*Observing Weather and Climate from the Ground Up*" (NRC 2009). As shown here, nocturnal convection is often elevated and is initiated by features located above the surface such as elevated convergence zones or atmospheric waves. Environments supportive of gravity waves or atmospheric bores are also very sensitive to the structure of small-scale jets and trapping layers. Therefore the assimilation of thermodynamic and kinematic profilers can provide key information for such environments during periods when operational rawinsondes were unavailable. Future work will examine the impact of assimilating these unique observation sets. Additionally, these datasets will likely prove useful in verifying other mechanisms responsible for convection at night.

Since nocturnal convection can be initiated by many different mechanisms, further work into determining optimal model configurations for the explicit purpose of forecasting CI should be explored. The most important of these is likely the

horizontal and vertical grid spacing, both of which will be explored in future simulations. Johnson et al. (2016) found that atmospheric bore-like features are able to be produced but not fully resolved in a 4 km simulation. Though the 4 km horizontal grid spacing and 50 vertical levels were sufficient enough to produce the new convection in this case, various features which are responsible for initiating new convection at night possibly occur on much smaller scales. Schumacher (2015) found problems with simulating supercells and MCSs with grid spacing lower less than 4 km due to overmixing of a dryline, therefore detailed work will be required to find the optimal resolution to resolve these features but not cause issues elsewhere.

Bibliography

Ahijevych, D., C. Davis, R. Carbone, and J. Tuttle, 2004: Initiation of precipitation episodes relative to elevated terrain. *J. Atmos. Sci.*, **61 (22)**, 2763–2769.

Anderson, C. J., and R. W. Arritt, 1998: Mesoscale convective complexes and persistent elongated convective systems over the United States during 1992 and 1993. *Mon. Wea. Rev.*, **126 (3)**, 578–599.

Augustine, J. A., and F. Caracena, 1994: Lower-tropospheric precursors to nocturnal MCS development over the central United States. *Wea. Forecasting*, **9 (1)**, 116–135.

Billings, J. M., and M. D. Parker, 2012: Evolution and maintenance of the 22-23 June 2003 nocturnal convection during BAMEX. *Wea. Forecasting*, **27**, 279–300.

Bodine, D., P. Heinselman, B. Cheong, R. Palmer, and D. Michaud, 2010: A case study on the impact of moisture variability on convection initiation using radar refractivity retrievals. *J. Appl. Meteor. Climatol.*, **49 (8)**, 1766–1778.

Carbone, R. E., and J. D. Tuttle, 2008: Rainfall occurrence in the US Warm season: The Diurnal Cycle. *J. Climate*, **21 (16)**, 4132–4146.

Carbone, R. E., J. D. Tuttle, D. A. Ahijevych, and S. B. Trier, 2002: Inferences of predictability associated with warm season precipitation episodes. *J. Atmos. Sci.*, **59 (13)**, 2033–2056.

Childs, P. P., A. L. Qureshi, S. Raman, K. Alapaty, R. Ellis, R. Boyles, and D. Niyogi, 2006: Simulation of convective initiation during IHOP_2002 using the flux-adjusting surface data assimilation system (FASDAS). *Mon. Wea. Rev.*, **134 (1)**, 134–148.

Colman, B. R., 1990: Thunderstorms above frontal surfaces in environments without positive CAPE. Part I: A climatology. *Mon. Wea. Rev.*, **118 (5)**, 1103–1122.

Coniglio, M. C., J. Correia Jr, P. T. Marsh, and F. Kong, 2013: Verification of convection-allowing WRF model forecasts of the planetary boundary layer using sounding observations. *Wea. Forecasting*, **28 (3)**, 842–862.

Corfidi, S. F., S. J. Corfidi, and D. M. Schultz, 2008: Elevated convection and castellanus: Ambiguities, significance, and questions. *Wea. Forecasting*, **23 (6)**, 1280–1303.

Crook, N. A., 1988: Trapping of low-level internal gravity waves. *J. Atmos. Sci.*, **45 (10)**, 1533–1541.

Davis, C., and Coauthors, 2004: The Bow Echo and MCV Experiment-Observations and opportunities. *Bull. Amer. Meteor. Soc.*, **85 (8)**, 1075–1093.

Dawson, D. T., M. Xue, J. A. Milbrandt, and M. Yau, 2010: Comparison of evaporation and cold pool development between single-moment and multimoment bulk microphysics schemes in idealized simulations of tornadic thunderstorms. *Mon. Wea. Rev.*, **138 (4)**, 1152–1171.

Denis, B., J. Côté, and R. Laprise, 2002: Spectral decomposition of two-dimensional atmospheric fields on limited-area domains using the discrete cosine transform (DCT). *Mon. Wea. Rev.*, **130 (7)**, 1812–1829.

Dowell, D. C., and L. J. Wicker, 2009: Additive noise for storm-scale ensemble data assimilation. *J. Atmos. Oceanic Technol.*, **26 (5)**, 911–927.

Dowell, D. C., L. J. Wicker, and C. Snyder, 2011: Ensemble Kalman filter assimilation of radar observations of the 8 May 2003 Oklahoma City supercell: Influences of reflectivity observations on storm-scale analyses. *Mon. Wea. Rev.*, **139 (1)**, 272–294.

Duda, J. D., X. Wang, F. Kong, and M. Xue, 2014: Using varied microphysics to account for uncertainty in warm-season QPF in a convection-allowing ensemble. *Mon. Wea. Rev.*, **142 (6)**, 2198–2219.

Ek, M., K. Mitchell, Y. Lin, E. Rogers, P. Grunmann, V. Koren, G. Gayno, and J. Tarpley, 2003: Implementation of Noah land surface model advances in the National Centers for Environmental Prediction operational mesoscale Eta model. *J. Geophys. Res.*, **108 (D22)**.

Eom, J. K., 1975: Analysis of the internal gravity wave occurrence of 19 April 1970 in the Midwest. *Mon. Wea. Rev.*, **103 (3)**, 217–226.

French, A. J., and M. D. Parker, 2008: The initiation and evolution of multiple modes of convection within a meso-alpha scale region. *Wea. Forecasting*, **23**, 1221–1251.

Fritsch, J. M., and R. E. Carbone, 2004: Improving quantitative precipitation forecasts in the warm season: A USWRP research and development strategy. *Bull. Amer. Meteor. Soc.*, **85 (7)**, 955–965.

Fritsch, J. M., R. A. Houze Jr, R. Adler, H. Bluestein, and Coauthors, 1998: Quantitative precipitation forecasting: Report of the eighth prospectus development team, US Weather Research Program. *Bull. Amer. Meteor. Soc.*, **79 (2)**, 285.

Gale, J. J., W. A. Gallus Jr, and K. A. Jungbluth, 2002: Toward improved prediction of mesoscale convective system dissipation. *Wea. Forecasting*, **17 (4)**, 856–872.

Gaspari, G., and S. E. Cohn, 1999: Construction of correlation functions in two and three dimensions. *Quart. J. Roy. Meteor. Soc.*, **125 (554)**, 723–757.

Gasperoni, N. A., M. Xue, R. D. Palmer, and J. Gao, 2013: Sensitivity of convective initiation prediction to near-surface moisture when assimilating radar refractivity: Impact tests using OSSEs. *J. Atmos. Oceanic Technol.*, **30 (10)**, 2281–2302.

Gilmore, M. S., J. M. Straka, and E. N. Rasmussen, 2004: Precipitation and Evolution Sensitivity in Simulated Deep Convective Storms: Comparisons between Liquid-Only and Simple Ice and Liquid Phase Microphysics. *Mon. Wea. Rev.*, **132 (8)**, 1897–1916.

Glickman, T. S., and W. Zenk, 2000: *Glossary of Meteorology*. American Meteorological Society, 850 pp.

Grasso, L., D. T. Lindsey, K.-S. Sunny Lim, A. Clark, D. Bikos, and S. R. Dembek, 2014: Evaluation of and suggested improvements to the WSM6 microphysics in WRF-ARW using synthetic and observed GOES-13 imagery. *Mon. Wea. Rev.*, **142 (10)**, 3635–3650.

Grell, G. A., and S. R. Freitas, 2013: A scale and aerosol aware stochastic convective parameterization for weather and air quality modeling. *Atmos. Chem. Phys.*, **13 (9)**, 23 845–23 893.

Hamill, T. M., 2006: Ensemble-based atmospheric data assimilation. *Predictability of Weather and Climate*, Cambridge University Press, 124–156.

Hamill, T. M., J. S. Whitaker, M. Fiorino, and S. G. Benjamin, 2011a: Global ensemble predictions of 2009's tropical cyclones initialized with an ensemble Kalman filter. *Mon. Wea. Rev.*, **139 (2)**, 668–688.

Hamill, T. M., J. S. Whitaker, D. T. Kleist, M. Fiorino, and S. G. Benjamin, 2011b: Predictions of 2010's tropical cyclones using the GFS and ensemble-based data assimilation methods. *Mon. Wea. Rev.*, **139 (10)**, 3243–3247.

Heideman, K. F., and M. J. Fritsch, 1988: Forcing mechanisms and other characteristics of significant summertime precipitation. *Wea. Forecasting*, **3 (2)**, 115–130.

Helfand, H. M., and S. D. Schubert, 1995: Climatology of the simulated Great Plains low-level jet and its contribution to the continental moisture budget of the United States. *J. Climate*, **8 (4)**, 784–806.

Higgins, R., Y. Yao, E. Yarosh, J. E. Janowiak, and K. Mo, 1997: Influence of the Great Plains low-level jet on summertime precipitation and moisture transport over the central United States. *J. Climate*, **10 (3)**, 481–507.

Holt, T., and S. Raman, 1988: A review and comparative evaluation of multilevel boundary layer parameterizations for first-order and turbulent kinetic energy closure schemes. *Reviews of Geophys.*, **26 (4)**, 761–780.

Hong, S.-Y., and S.-W. Kim, 2008: Stable boundary layer mixing in a vertical diffusion scheme. *18th Symposium on Boundary Layers and Turbulence*, Vol. 16.

Hong, S.-Y., and J.-O. J. Lim, 2006: The WRF single-moment 6-class microphysics scheme (WSM6). *J. Korean Meteor. Soc*, **42 (2)**, 129–151.

Hong, S.-Y., and H.-L. Pan, 1996: Nonlocal boundary layer vertical diffusion in a medium-range forecast model. *Mon. Wea. Rev.*, **124 (10)**, 2322–2339.

Hong, S.-Y., K.-S. Sunny Lim, J.-H. Kim, J.-O. Jade Lim, and J. Dudhia, 2009: Sensitivity study of cloud-resolving convective simulations with WRF using two bulk microphysical parameterizations: ice-phase microphysics versus sedimentation effects. *J. Climate Appl. Meteor.*, **48 (1)**, 61–76.

Houtekamer, P., and F. Zhang, 2016: Review of the Ensemble Kalman Filter for Atmospheric Data Assimilation. *Mon. Wea. Rev.*, **Early Release**.

Hu, X.-M., J. W. Nielsen-Gammon, and F. Zhang, 2010: Evaluation of three planetary boundary layer schemes in the WRF model. *J. Climate Appl. Meteor.*, **49 (9)**, 1831–1844.

Iacono, M. J., J. S. Delamere, E. J. Mlawer, M. W. Shephard, S. A. Clough, and W. D. Collins, 2008: Radiative forcing by long-lived greenhouse gases: Calculations with the AER radiative transfer models. *J. Geophys. Res.*, **113 (D13)**.

Janjic, Z. I., 1994: The step-mountain eta coordinate model: Further developments of the convection, viscous sublayer, and turbulence closure schemes. *Mon. Wea. Rev.*, **122 (5)**, 927–945.

Janjić, Z. I., 2002: Nonsingular implementation of the Mellor–Yamada level 2.5 scheme in the NCEP Meso model. *NCEP office note*, 61 pp.

Jewett, B. F., M. K. Ramamurthy, and R. M. Rauber, 2003: Origin, evolution, and finescale structure of the St. Valentine's Day mesoscale gravity wave observed during STORM-FEST. Part III: Gravity wave genesis and the role of evaporation. *Mon. Wea. Rev.*, **131 (4)**, 617–633.

Jing, Z., and G. Wiener, 1993: Two-dimensional dealiasing of Doppler velocities. *J. Atmos. Oceanic Technol.*, **10 (6)**, 798–808.

Johnson, A., and X. Wang, 2016: Design and implementation of a GSI-based convection-allowing ensemble data assimilation and forecast system for the PECAN field experiment. Part 1: Optimal configurations for nocturnal convection prediction using retrospective cases. *Wea. Forecasting*, **In Review**.

Johnson, A., X. Wang, J. R. Carley, L. J. Wicker, and C. Karstens, 2015: A comparison of multiscale GSI-based EnKF and 3DVar data assimilation using radar and conventional observations for midlatitude convective-scale precipitation forecasts. *Mon. Wea. Rev.*, **143 (8)**, 3087–3108.

Johnson, A., X. Wang, and S. K. Degelia, 2016: Design and implementation of a GSI-based convection-allowing ensemble data assimilation and forecast system for the PECAN field experiment. Part 2: Overview and evaluation of real-time system. *Wea. Forecasting*, **In Review**.

Johnson, A., X. Wang, F. Kong, and M. Xue, 2011: Hierarchical cluster analysis of a convection-allowing ensemble during the Hazardous weather Testbed 2009 spring experiment. Part II: Ensemble Clustering over the Whole Experiment Period. *Mon. Wea. Rev.*, **139 (12)**, 3694–3710.

Jones, T. A., D. Stensrud, L. Wicker, P. Minnis, and R. Palikonda, 2015: Simultaneous radar and satellite data storm-scale assimilation using an ensemble Kalman filter approach for 24 May 2011. *Mon. Wea. Rev.*, **143 (1)**, 165–194.

Kain, J. S., and Coauthors, 2013: A feasibility study for probabilistic convection initiation forecasts based on explicit numerical guidance. *Bull. Amer. Meteor. Soc.*, **94 (8)**, 1213–1225.

Keenan, T., and R. Carbone, 2008: Propagation and diurnal evolution of warm season cloudiness in the Australian and Maritime Continent region. *Mon. Wea. Rev.*, **136 (3)**, 973–994.

Kleist, D. T., D. F. Parrish, J. C. Derber, R. Treadon, W.-S. Wu, and S. Lord, 2009: Introduction of the GSI into the NCEP global data assimilation system. *Wea. Forecasting*, **24 (6)**, 1691–1705.

Koch, S. E., C. Flamant, J. W. Wilson, B. M. Gentry, and B. D. Jamison, 2008: An atmospheric soliton observed with doppler radar, differential absorption lidar, and a molecular doppler lidar. *J. Atmos. Oceanic Technol.*, **25 (8)**, 1267–1287.

Lakshmanan, V., T. Smith, G. Stumpf, and K. Hondl, 2007: The warning decision support system-integrated information. *Wea. Forecasting*, **22 (3)**, 596–612.

Lazo, J. K., M. Lawson, P. H. Larsen, and D. M. Waldman, 2011: US economic sensitivity to weather variability. *Bull. Amer. Meteor. Soc.*, **92**, 709–720.

Li, Y., and R. B. Smith, 2010: The detection and significance of diurnal pressure and potential vorticity anomalies east of the Rockies. *J. Atmos. Sci.*, **67 (9)**, 2734–2751.

Li, Z., P. Zuidema, P. Zhu, and H. Morrison, 2015: The sensitivity of simulated shallow cumulus convection and cold pools to microphysics. *J. Atmos. Sci.*, **72 (9)**, 3340–3355.

Lim, K.-S. S., and S.-Y. Hong, 2010: Development of an effective double-moment cloud microphysics scheme with prognostic cloud condensation nuclei (CCN) for weather and climate models. *Mon. Wea. Rev.*, **138 (5)**, 1587–1612.

Lin, Y.-L., R. D. Farley, and H. D. Orville, 1983: Bulk parameterization of the snow field in a cloud model. *J. Climate Appl. Meteor.*, **22 (6)**, 1065–1092.

Liu, C., and M. W. Moncrieff, 2007: Sensitivity of cloud-resolving simulations of warm-season convection to cloud microphysics parameterizations. *Mon. Wea. Rev.*, **135 (8)**, 2854–2868.

Liu, Y., D.-l. Zhang, and M. Yau, 1997: A multiscale numerical study of Hurricane Andrew (1992). Part I: Explicit simulation and verification. *Mon. Wea. Rev.*, **125 (12)**, 3073–3093.

Maddox, R. A., C. F. Chappell, and L. R. Hoxit, 1979: Synoptic and meso-α scale aspects of flash flood events. *Bull. Amer. Meteor. Soc.*, **60 (2)**, 115–123.

Marquis, J., Y. Richardson, P. Markowski, D. Dowell, J. Wurman, K. Kosiba, P. Robinson, and G. Romine, 2014: An investigation of the Goshen County, Wyoming, tornadic supercell of 5 June 2009 using EnKF assimilation of mobile mesonet and radar observations collected during VORTEX2. Part I: Experiment design and verification of the EnKF analyses. *Mon. Wea. Rev.*, **142 (2)**, 530–554.

Marsham, J. H., S. B. Trier, T. M. Weckwerth, and J. W. Wilson, 2011: Observations of elevated convection initiation leading to a surface-based squall line during 13 June IHOP_2002. *Mon. Wea. Rev.*, **139 (1)**, 247–271.

Martin, W. J., and M. Xue, 2006: Sensitivity analysis of convection of the 24 May 2002 IHOP case using very large ensembles. *Mon. Wea. Rev.*, **134 (1)**, 192–207.

Min, K.-H., S. Choo, D. Lee, and G. Lee, 2015: Evaluation of WRF Cloud Microphysics Schemes Using Radar Observations. *Wea. Forecasting*, **30 (6)**, 1571–1589.

Moore, J. T., F. H. Glass, C. E. Graves, S. M. Rochette, and M. J. Singer, 2003: The environment of warm-season elevated thunderstorms associated with heavy rainfall over the central United States. *Wea. Forecasting*, **18 (5)**, 861–878.

Morrison, H., J. Curry, and V. Khvorostyanov, 2005: A new double-moment microphysics parameterization for application in cloud and climate models. Part I: Description. *J. Atmos. Sci.*, **62 (6)**, 1665–1677.

Morrison, H., and J. Milbrandt, 2010: Comparison of two-moment bulk microphysics schemes in idealized supercell thunderstorm simulations. *Mon. Wea. Rev.*, **193**, 1103–1130.

Morrison, H., A. Morales, and C. Villanueva-Birriel, 2015: Concurrent sensitivities of an idealized deep convective storm to parameterization of microphysics, horizontal grid resolution, and environmental static stability. *Mon. Wea. Rev.*, **143 (6)**, 2082–2104.

Nakanishi, M., and H. Niino, 2004: An improved Mellor–Yamada level-3 model with condensation physics: Its design and verification. *Boundary-layer Meteor.*, **112 (1)**, 1–31.

Nakanishi, M., and H. Niino, 2009: Development of an improved turbulence closure model for the atmospheric boundary layer. *J. Meteor. Soc. Japan*, **87 (5)**, 895–912.

Nasrollahi, N., A. AghaKouchak, J. Li, X. Gao, K. Hsu, and S. Sorooshian, 2012: Assessing the impacts of different WRF precipitation physics in hurricane simulations. *Wea. Forecasting*, **27 (4)**, 1003–1016.

Newton, C. W., 1967: Severe convective storms. *Adv. Geoph.*, **12**, 257–308.

NOAA, 2004: Summary of Natural Hazard Statistics for 2004 in the United States. Accessed 1 July 2016 [Available online at http://www.nws.noaa.gov/om/hazstats/sum04.pdf].

NOAA, 2013: NWS Text Product Archive. Accessed 1 July 2016 [Available online at https://mesonet.agron.iastate.edu/wx/afos/list.phtml].

Noh, Y., W. Cheon, S. Hong, and S. Raasch, 2003: Improvement of the K-profile model for the planetary boundary layer based on large eddy simulation data. *Boundary-layer Meteor.*, **107 (2)**, 401–427.

NRC, 2009: *Observing Weather and Climate from the Ground Up: A Nationwide Network of Networks*. National Research Council Committee on Developing Mesoscale Meteorological Observational Capabilities to Meet Multiple National Needs. National Academies Press. 250 pp.

Otkin, J., H.-L. Huang, and A. Seifert, 2006: A comparison of microphysical schemes in the WRF model during a severe weather event. *7th WRF Users' Workshop*, Boulder, CO, USA.

Parish, T. R., and L. D. Oolman, 2010: On the role of sloping terrain in the forcing of the Great Plains low-level jet. *J. Atmos. Sci.*, **67 (8)**, 2690–2699.

Parker, M. D., 2008: Response of simulated squall lines to low-level cooling. *J. Atmos. Sci.*, **65 (4)**, 1323–1341.

Parker, M. D., and D. A. Ahijevych, 2007: Convective episodes in the east-central United States. *Mon. Wea. Rev.*, **135 (11)**, 3707–3727.

Parsons, D. B., B. Geerts, and T. Weckwerth, 2013: Plains Elevated Convection at Night (PECAN) Scientific Program Overview.

Peña, M., and E. Kalnay, 2004: Separating fast and slow modes in coupled chaotic systems. *Nonlinear Processes in Geophys.*, **11 (3)**, 319–327.

Pieri, A. B., J. von Hardenberg, A. Parodi, and A. Provenzale, 2015: Sensitivity of Precipitation Statistics to Resolution, Microphysics, and Convective Parameterization: A Case Study with the High-Resolution WRF Climate Model over Europe. *J. Hydrometeor.*, **16 (4)**, 1857–1872.

Pitchford, K. L., and J. London, 1962: The low-level jet as related to nocturnal thunderstorms over midwest United States. *J. Appl. Meteor.*, **1 (1)**, 43–47.

Pleim, J. E., 2007: A combined local and nonlocal closure model for the atmospheric boundary layer. Part I: Model description and testing. *J. Climate Appl. Meteor.*, **46 (9)**, 1383–1395.

Rottman, J. W., and J. E. Simpson, 1989: The formation of internal bores in the atmosphere: A laboratory model. *Quart. J. Roy. Meteor. Soc.*, **115 (488)**, 941–963.

Sakov, P., G. Evensen, and L. Bertino, 2010: Asynchronous data assimilation with the EnKF. *Tellus A*, **62 (1)**, 24–29.

Schumacher, R. S., 2015: Resolution Dependence of Initiation and Upscale Growth of Deep Convection in Convection-Allowing Forecasts of the 31 May–1 June 2013 Supercell and MCS. *Mon. Wea. Rev.*, **143 (11)**, 4331–4354.

Schumacher, R. S., and R. H. Johnson, 2009: Quasi-stationary, extreme-rain-producing convective systems associated with midlevel cyclonic circulations. *Wea. Forecasting*, **24 (2)**, 555–574.

Scorer, R., 1949: Theory of waves in the lee of mountains. *Quart. J. Roy. Meteor. Soc.*, **75 (323)**, 41–56.

Shin, H. H., and S.-Y. Hong, 2011: Intercomparison of planetary boundary-layer parameterizations in the WRF model for a single day from CASES-99. *Boundary-layer Meteor.*, **139 (2)**, 261–281.

Skamarock, W., and Coauthors, 2008: A description of the advanced research WRF Ver. 30. NCAR Technical Note. Tech. rep., NCAR/TN-475.

Snook, N., M. Xue, and Y. Jung, 2015: Multiscale EnKF assimilation of radar and conventional observations and ensemble forecasting for a tornadic mesoscale convective system. *Mon. Wea. Rev.*, **143 (4)**, 1035–1057.

Sobash, R. A., and D. J. Stensrud, 2013: The impact of covariance localization for radar data on EnKF analyses of a developing MCS: Observing system simulation experiments. *Mon. Wea. Rev.*, **141 (11)**, 3691–3709.

Sobash, R. A., and D. J. Stensrud, 2015: Assimilating surface mesonet observations with the EnKF to improve ensemble forecasts of convection initiation on 29 May 2012. *Mon. Wea. Rev.*, **143 (9)**, 3700–3725.

Sukoriansky, S., B. Galperin, and V. Perov, 2005: Application of a new spectral theory of stably stratified turbulence to the atmospheric boundary layer over sea ice. *Boundary-layer Meteor.*, **117 (2)**, 231–257.

Surcel, M., M. Berenguer, and I. Zawadzki, 2010: The diurnal cycle of precipitation from continental radar mosaics and numerical weather prediction models. Part I: Methodology and seasonal comparison. *Mon. Wea. Rev.*, **138 (8)**, 3084–3106.

Tao, W.-K., and J. Simpson, 1989: Modeling study of a tropical squall-type convective line. *J. Atmos. Sci.*, **46 (2)**, 177–202.

Tao, W.-K., and Coauthors, 2003: Microphysics, radiation and surface processes in the Goddard Cumulus Ensemble (GCE) model. *Meteor. Atmos. Phys.*, **82 (1)**, 97–137.

Thompson, G., P. R. Field, R. M. Rasmussen, and W. D. Hall, 2008: Explicit forecasts of winter precipitation using an improved bulk microphysics scheme. Part II: Implementation of a new snow parameterization. *Mon. Wea. Rev.*, **136 (12)**, 5095–5115.

Thompson, T., 2014: Ensemble Kalman Filter Methods for Convective-Scale Radar Data Assimilation and Multi-Scale Data Assimilation of the 13 June 2010 Tornadic Supercell Environment. Ph.D. Dissertation. School of Meteorology, University of Oklahoma.

Tollerud, E. I., and Coauthors, 2008: Mesoscale moisture transport by the low-level jet during the IHOP field experiment. *Mon. Wea. Rev.*, **136 (10)**, 3781–3795.

Trier, S. B., and D. B. Parsons, 1993: Evolution of environmental conditions preceding the development of a nocturnal mesoscale convective complex. *Mon. Wea. Rev.*, **121 (4)**, 1078–1098.

Trier, S. B., G. S. Romine, D. A. Ahijevych, R. J. Trapp, R. S. Schumacher, M. C. Coniglio, and D. J. Stensrud, 2015: Mesoscale thermodynamic influences on convection initiation near a surface dryline in a convection-permitting ensemble. *Mon. Wea. Rev.*, **143 (9)**, 3726–3753.

Tripoli, G. J., and W. R. Cotton, 1989a: Numerical study of an observed orogenic mesoscale convective system. Part 1: Simulated genesis and comparison with observations. *Mon. Wea. Rev.*, **117 (2)**, 273–304.

Tripoli, G. J., and W. R. Cotton, 1989b: Numerical study of an observed orogenic mesoscale convective system. II: Analysis of governing dynamics. *Mon. Wea. Rev.*, **117 (2)**, 305–328.

Wallace, J. M., 1975: Diurnal variations in precipitation and thunderstorm frequency over the conterminous United States. *Mon. Wea. Rev.*, **103 (5)**, 406–419.

Wang, X., D. M. Barker, C. Snyder, and T. M. Hamill, 2008: A hybrid ETKF-3DVAR data assimilation scheme for the WRF model. Part I: Observing system simulation experiment. *Mon. Wea. Rev.*, **136 (12)**, 5116–5131.

Wang, X., and T. Lei, 2014: GSI-based four-dimensional ensemble–variational (4DEnsVar) data assimilation: Formulation and single-resolution experiments with real data for NCEP Global Forecast System. *Mon. Wea. Rev.*, **142 (9)**, 3303–3325.

Wang, X., D. Parrish, D. Kleist, and J. Whitaker, 2013: GSI 3DVar-based ensemble–variational hybrid data assimilation for NCEP Global Forecast System: Single-resolution experiments. *Mon. Wea. Rev.*, **141 (11)**, 4098–4117.

Weisman, M. L., C. Davis, W. Wang, K. W. Manning, and J. B. Klemp, 2008: Experiences with 0-36-h explicit convective forecasts with the WRF-ARW model. *Wea. Forecasting*, **23 (3)**, 407–437.

Wheatley, D. M., N. Yussouf, and D. J. Stensrud, 2014: Ensemble Kalman filter analyses and forecasts of a severe mesoscale convective system using different choices of microphysics schemes. *Mon. Wea. Rev.*, **142 (9)**, 3243–3263.

Whitaker, J. S., and T. M. Hamill, 2002: Ensemble data assimilation without perturbed observations. *Mon. Wea. Rev.*, **130 (7)**, 1913–1924.

Whitaker, J. S., and T. M. Hamill, 2012: Evaluating methods to account for system errors in ensemble data assimilation. *Mon. Wea. Rev.*, **140 (9)**, 3078–3089.

Whitaker, J. S., T. M. Hamill, X. Wei, Y. Song, and Z. Toth, 2008: Ensemble data assimilation with the NCEP global forecast system. *Mon. Wea. Rev.*, **136 (2)**, 463–482.

White, B. L., and K. R. Helfrich, 2012: A general description of a gravity current front propagating in a two-layer stratified fluid. *J. Fluid Mech.*, **711**, 545–575.

Wilson, J. W., and R. D. Roberts, 2006: Summary of convective storm initiation and evolution during IHOP: Observational and modeling perspective. *Mon. Wea. Rev.*, **134 (1)**, 23–47.

Xue, M., and W. J. Martin, 2006a: A high-resolution modeling study of the 24 May 2002 dryline case during IHOP. Part I: Numerical simulation and general evolution of the dryline and convection. *Mon. Wea. Rev.*, **134 (1)**, 149–171.

Xue, M., and W. J. Martin, 2006b: A high-resolution modeling study of the 24 May 2002 dryline case during IHOP. Part II: Horizontal convective rolls and convective initiation. *Mon. Wea. Rev.*, **134 (1)**, 172–191.

Yussouf, N., D. C. Dowell, L. J. Wicker, K. H. Knopfmeier, and D. M. Wheatley, 2015: Storm-scale data assimilation and ensemble forecasts for the 27 April 2011 severe weather outbreak in Alabama. *Mon. Wea. Rev.*, **143 (8)**, 3044–3066.

Yussouf, N., E. R. Mansell, L. J. Wicker, D. M. Wheatley, and D. J. Stensrud, 2013: The ensemble Kalman filter analyses and forecasts of the 8 May 2003 Oklahoma City tornadic supercell storm using single-and double-moment microphysics schemes. *Mon. Wea. Rev.*, **141 (10)**, 3388–3412.

Zamora, R., and Coauthors, 2003: Comparing MM5 radiative fluxes with observations gathered during the 1995 and 1999 Nashville southern oxidants studies. *J. Geophys. Res.*, **108 (D2)**.

Zhang, F., Y. Weng, J. A. Sippel, Z. Meng, and C. H. Bishop, 2009: Cloud-resolving hurricane initialization and prediction through assimilation of Doppler radar observations with an ensemble Kalman filter. *Mon. Wea. Rev.*, **137 (7)**, 2105–2125.

Zhu, K., Y. Pan, M. Xue, X. Wang, J. S. Whitaker, S. G. Benjamin, S. S. Weygandt, and M. Hu, 2013: A regional GSI-based ensemble Kalman filter data assimilation system for the rapid refresh configuration: Testing at reduced resolution. *Mon. Wea. Rev.*, **141 (11)**, 4118–4139.